ON THE DYNAMICS AND CONTROL STRATEGY OF TIME-DELAYED VIBRO-IMPACT OSCILLATORS

A Dissertation

by

CHI-WEI KUO

Submitted to the Office of Graduate and Professional Studies of
Texas A&M University
in partial fulfillment of the requirements for the degree of

DOCTOR OF PHILOSOPHY

Chair of Committee,	Chii-Der Suh
Committee Members,	Bruce L. Tai
	Pilwon Hur
	Yaroslav Vorobets
Head of Department,	Andreas A. Polycarpou

August 2019

Major Subject: Mechanical Engineering

ABSTRACT

Being able to control nonlinear oscillators, which are ubiquitous, has significant engineering implications in process development and product sustainability design. The fundamental characteristics of a vibro-impact oscillator, a non-autonomous time-delayed feedback oscillator, and a time-delayed vibro-impact oscillator are studied. Their being stochastic, nonstationary, non-smooth, and dynamically complex render the mitigation of their behaviors in response to linear and stationary inputs very difficult if not entirely impossible. A novel nonlinear control concept featuring simultaneous control of vibration amplitude in the time-domain and spectral response in the frequency-domain is developed and subsequently incorporated to maintain dynamic stability in these nonlinear oscillators by denying bifurcation and route-to-chaos from coming to pass. Convergence of the controller is formulated to be inherently unconditional with the optimization step size being self-adaptive to system identification and control force input. Optimal initial filter weights are also derived to warrant fast convergence rate and short response time. These novel features impart adaptivity, intelligence, and universal applicability to the wavelet based nonlinear time-frequency control methodology. The validity of the controller design is demonstrated by evaluating its performance against PID and fuzzy logic controllers in controlling the aperiodic, broad bandwidth, discontinuous responses characteristic of the time-delayed, vibro-impact oscillator.

ACKNOWLEDGEMENTS

I would like to thank my committee chairman, Dr. Suh, and my committee members, Dr. Hur, Dr. Tai, and Dr. Vorobets, for their guidance and support throughout the writing of this dissertation.

Thanks also go to my friends and colleagues and the department faculty and staff for making my time at Texas A&M University a great experience.

Finally, I want to thank my loving parents for their encouragement and to my wife for her patience and love. You are always there for me.

CONTRIBUTORS AND FUNDING SOURCES

Contributors

This work was supervised by dissertation committees consisting of Professor Steve Suh, Professor Bruce Tai, and Professor Pilwon Hur of the Department of Mechanical Engineering and Professor Yaroslav Vorobets of the Department of Mathematics.

Funding Sources

No outside funding was received for the research and compilation of this document.

TABLE OF CONTENTS

Page

LIST OF FIGURES

Page

LIST OF TABLES

Page

CHAPTER I

INTRODUCTION AND LITERATURE REVIEW

Current State of Affairs

Vibro-impact oscillators and time-delayed systems are nonlinear systems commonly found in science and engineering applications. Time-delayed vibro-impact oscillators govern many real-world systems such as bearing, gear drivers, machining, hammer-like percussion drilling, shock absorbers, and processes involving rolling contact. These dynamic systems exhibit prominent nonlinear behaviors. Time-delayed vibro-impact oscillators have various states of motion between non-impacting and impacting that induce complex dynamical responses. As a type of dynamic instability commonly observed in time-delayed vibro-impact oscillators where the impact velocity approaches zero, grazing bifurcation is a state in which the system switches suddenly from being periodic to chaotic. If not properly controlled, these nonlinear dynamic responses can lead to catastrophic failure. To comprehensively study time-delayed vibro-impact systems in search for a better control solution, a vibro-impact oscillator and a time-delayed system are studied in the dissertation. Once a feasible control method is developed, it can be further improved to enable manufacturing at increasing speed, extending equipment life, and reducing power consumption.

Literature Review

In this section, literatures on vibro-impact oscillators and time-delayed oscillators are reviewed. In addition, the strength and weakness of several common control methodologies are also discussed.

Vibro-Impact Oscillators

A vibro-impact system, or otherwise known as impact oscillator, is a discrete- or continuous-time dynamic system whose state-space is divided into different regions by a discontinuity set [1-4]. Real-world systems such as bearings, gear drives, machining, hammer-like percussion drilling, shock absorbers, and processes involving rolling contact are impact oscillators whose dynamics are characterized by complex bifurcation. Such systems can inadvertently experience the undesirable effect of abruptly changing from being non-impacting to impacting [5-8]. As a dynamic instability commonly observed in vibro-impact systems in which the impact velocity approaches zero [9], grazing bifurcation is a state in which the dynamics of a system switches suddenly from being periodic to chaotic. If not properly mitigated, grazing can lead to catastrophic failure.

Grazing is inherent to becoming chaotic [10, 11]. Low velocity impact may create several types of grazing bifurcation including period adding cascades with or without chaotic bands [12]. When certain conditions are met, the corresponding grazing trajectory would be periodic and stable [13, 14] and the grazing intersection of a quasi-periodic oscillation with a two-dimensional impact mechanism in a three-dimensional

state space can be predicted by discontinuity mapping [15]. Through the application of singularity theory [16, 17], nondegenerate grazing, minimally degenerate grazing, and extra degenerate grazing are also identified as the probable dynamic responses to low-velocity impact [18] whose further deterioration into chaotic motion can be sufficiently described [19]. It was shown using a test apparatus that a low-velocity impact oscillator can be effectively modelled as a singular system [20]. While such systems of singularity demonstrated more abundant dynamics than hard collisions [21] and that most orbits near a grazing condition are chaotic, nonetheless, there are periodic and stable orbits to be found [22]. An extensive amount of knowledge about low-velocity grazing bifurcation have since been physically confirmed [23, 24].

Controlling grazing so as to stabilize vibro-impact induced instability in non-smooth systems is essential for many engineering applications [25]. When a system experiences grazing, the corresponding dynamic response contains an infinite number of unstable periodic orbits. Furthermore, the trajectory of the system rapidly appears in the vicinity of each other. Of the handful efforts documented in addressing grazing control, one was on applying a synchronization scheme to stabilize a chaotic impact oscillator [26]. The linear scheme that was followed, however, could not fully represent the chaotic motion and the impact dynamic response did not enter the grazing bifurcation state. The same control method was subsequently utilized to constrain the displacement of an impact oscillator with double-sided walls to a predefined position [27]. Another was on applying an external force to wind-up or wind-down a cantilever beam undergoing period-1 motion and grazing bifurcation to be controlled [28]. Fast

harmonic base displacement was shown to be effective in controlling a single-sided Hertzian contact forced oscillator [29]. Feedback loop control with a time-delay was also reported as being viable for improving the stability of periodic orbits of a vibro-impact system [30].

Unlike high-velocity impact problems, grazing as the particular state of bifurcation associated with low-velocity impact is extremely challenging to deal with. This is primarily because grazing creates singularity in mapping from one motion state to another. Linearization along with the incorporation of linear control theory is oftentimes considered for grazing control. However, as the linearized dynamics does not fully represent the true response of the nonlinear system, the approach is not widely embraced for real-world applications. Another approach reported for grazing control employs the Lyapunov stability theory. However, as the Lyapunov function required of the task is very difficult to define, the Lyapunov-based approach is not as well received as the Ott-Grebogi-Yorke (OGY) method [31] which allows a targeted chaotic unstable periodic orbit to be stabilized by applying a small perturbation to the control parameter. The OGY method has been applied to (1) the control of a mechanical oscillator that describes the dynamics of an impulsive hybrid non-autonomous system [32], (2) the stabilization of a gear-rattling model where both ideal and non-ideal energy sources are considered [33], and (3) the suppression of chaotic vibro-impact response with prescribed damping laws [34, 35]. Albeit being preferred for impact oscillator control, nevertheless, the OGY method has been shown to be infeasible for reigning in nonlinear systems that are non-stationary [36]. The OGY method has its limitations rooted in the

followings - The first is that it is based on linearizing the corresponding Poincaré map and ignoring the nonlinear terms. The second is that the exact form of the unstable periodic orbit required to perform the control scheme is very difficult to obtain. In addition, the method allows no target response to be stipulated for the controlled oscillator to follow. In other words, the OGY method does not warrant that the controlled vibro-impact motion would be of the desired time and frequency qualities. OGY based schemes are unable to prevent further collisions from subsequently occurring once the controller is online.

Time-Delayed Oscillators

Time-delayed systems are ubiquitous in science and engineering. They are found governing a broad set of physical processes ranging from quantum dot laser [37] to electrical power transmission [38] to manufacturing chatter. Early interests were in characterizing time-delayed systems subject to the combined action of the time-delay and feedback parameters. Phase portrait and Poincaré section are commonly adopted for the task. For example, phase portraits were employed for the reconstruction of the chaotic data from an experiment performed on the Belousov-Zhabotinskii reaction [39] and the study of an autonomous rotary system [40]. Poincaré sections on the other hand were employed in the control of nonlinear ionization waves using time-delayed auto-synchronization [41] and for locating the periodic orbits of a time-delayed system [42]. Other characterization tools were also explored including the determination of the largest Lyapunov exponents for continuous as well as discrete systems [43, 44], the calculation

of proper delay time for chaotic time series [45], and the use of fractal dimension for searching for the proper embedding dimension that is also one of the parameters of the Method of Delays [46]. While being widely applied, nonetheless, the tools above are not without limitations. Phase portrait and Poincaré section are not feasible for erratic responses that are innately chaotic [47]. Lyapunov exponents or fractal dimensions are oftentimes insufficient for resolving chaotic responses because different attractors may generate the same Lyapunov numbers [48].

Time-delayed systems are rich in complex dynamical behaviors [49]. For example, an autonomous system requires two dimensions to demonstrate periodic responses, but it can display the same behaviors in one dimension with time-delay [50]. Besides rendering complex dynamical behaviors, time-delay parameters are also used for mitigating chaos [51]. The complex dynamical responses of aeroelasticity was mitigated using time-delayed feedback control [52]. An electrodynamic tether satellite system perturbed by its own electromagnetic interaction with the magnetic field of the earth was controlled by employing time-delayed autosynchronization [53]. A harmonic delayed system [54] and a van der Pol-Duffing oscillator [55] were stabilized by applying parametric delayed feedback control. Quantum systems affected by the filter-based control input and measurement-based feedback aberration were presented by manipulating time-delay parameters and non-smooth time-delayed control following a new Lyapunov–LaSalle-like stochastic stability criterion [56]. By employing a proper Lyapunov-Krasovskii functional and utilizing the new inequality on both the slowly- and

quickly-varying delayed systems, system dynamics were effectively bounded. More references focusing on time-delay parameter control can be found in [57, 61].

In general, it is difficult to tweak time-delay parameters without catastrophically perturbing the system to display route-to-chaos. For example, since material removal is inherently characterized by time-delayed feedback, machining speed is always set within a maximum cap to avoid the emergence of chaotic response. Thus, the manufacturing quality, efficiency, productivity could be enhanced markedly provided a viable control methodology is available. Controlling time-delayed physical processes is of great interest for several decades. For instance, state feedback controller designed based on the linear matrix inequality technique could handle both continuous and discrete time-delayed systems [62] but was insufficient in controlling nonlinear systems. Although Krasovskii-Lyapunov theory can be followed to synchronize Machey-Glass delayed differential equation [63], the linearization process mandated by the approach inadvertently skewed the true dynamics dictated by the high-order nonlinear terms. Nonlinear time-delayed systems [64] and a class of stochastic nonlinear time-delayed systems with a nonstrict-feedback structure [65] have been synthesized with fuzzy control. However, the fuzzy control approach is not generally applicable to higher order nonlinear systems since the systems cannot be known *a priori*.

Recently, control was employed to stabilize a pinning synchronizd system that was in a network of coupling delays [66]. Qiu et al. [67] focused on analyzing the delay-dependent stability and control of a class of continuous Markovian jump linear systems with time-varying delay. In addition to traditional control methodologies, fuzzy logic

control and sliding mode control are the choice methodologies for manipulating time-delayed feedback systems. Wu et al. [68] employed sliding mode control to a Markovian jump singular time-delayed system. Qi et al. [69] applied fuzzy logic control to stabilize a class of uncertain single-input-single-output (SISO) strict-feedback nonlinear time-delayed systems. They also considered an observer-based adaptive neural network control for the same system with unknown time-delays. In addition, Goyal [70] applied neural-network approximation and the Lyapunov-Krasovskii function theory based sliding mode control scheme to a class of unknown nonlinear discrete time systems. A new control scheme developed around the decentralized adaptive neural output feedback control law was also reported for a class of large-scale time-delayed systems [71] where exact *a priori* knowledge of the system parameters was not required. Predictive fuzzy control network was employed to address the random delays existed in communication channels [72]. Control of a delayed discrete-time system was demonstrated using the inverse reduction method to construct the corresponding recursive control algorithm [73]. Although these control methodologies are shown to be adaptable to these time-delayed systems, they are not viable for addressing nonlinear time-delayed systems of higher order.

Control Methodology

To stabilize a nonlinear oscillator, a small perturbation can be given to its input or system parameter. Parseval's theorem states that the total energy computed in the time-domain is equal to the total energy computed in the frequency-domain, thus

implying that time-domain control can be facilitated along with frequency-domain control simultaneously. Discrete Wavelet Transform (DWT) is a tool of choice using which dynamic aberrations indicative of bifurcation and deteriorating state of stability can be identified with simultaneous time–frequency resolution. In the dissertation, DWT is applied to address the non-stationary nature of the vibro-impact time-delayed oscillator by adopting the concept of active noise control [74] along with the filtered-x least mean square (FxLMS) optimization algorithm. In addition to noise control, FxLMS has been used to suppress the vibrations of composite structure [75], gear pairs [76], buildings [77], and machine tools [78]. It has combined with controllers such as feedback robust controller [79] and LQR controller [80] to promote the convergence speed and increase robust performance.

A novel nonlinear control scheme valid for the stabilization of non-autonomous time-delayed cubic order feedback oscillators and the mitigation of vibro-impact induced instability associated with a particular low-velocity impact oscillator is presented in the subsequent chapters. The basic ideas for the control scheme are derived from previous works [81-83] where nonlinear, non-stationary systems undergoing dynamic deteriorations including bifurcation and route-to-chaos were effectively controlled in both the time and frequency domains simultaneously. The scheme requires no linearization to allow the true dynamics of the time-delayed vibro-impact system being studied to be retained and properly interpreted. A system identification feature ensures that a desired target response is followed by the oscillator to mitigate the mapping singularity characteristic of grazing. The nonlinear oscillator traces the target which is

designed to be harmonic and of a prescribed vibration amplitude to realize 2 definitive objectives that signify control and stabilization: denying future collision and maintaining orbits that are spectrally bandwidth-limited and periodic. Albeit viable for mitigating chaotic behaviors in many nonlinear systems, however, the convergence property of the novel control scheme is yet to be investigated.

The primary configuration of this novel control follows the FxLMS algorithm. Although FxLMS has been widely used in adaptive filtering, derivation of the proper optimization step size that guarantees unconditional convergence remains to be provided [84]. It has been shown certain convergence conditions applied to FxLMS are not sufficient for the adaptive process [85]. By assuming that the input signal is abroad-band white signal and the secondary path is a pure delay system, a theoretical convergence condition for FxLMS has been derived by Long [86]. With the same secondary path and the input signal being a stochastic narrow-band signal, an FxLMS convergence analysis was conducted by Bjarnason [87]. In addition, another FxLMS convergence condition was derived considering the same secondary path with the narrow-band input signal being modeled as a combination of multiple sinusoids [88]. Another type of secondary path, which is a moving average process, is also available. Xiao [89] extended Vicente's analysis on this secondary path with the input signal being modeled as a combination of multiple sinusoids. Introduced by Gardener to simplify the complexity of deriving the FxLMS model while analyzing the convergence condition [90], the stochastic adaptation algorithm assumes the consecutive vectors of the input signal to be statistically independent. Based on the independence assumption, Ardekani

[91] derived the sufficient condition for the convergence of the FxLMS applicable to a more general secondary path. Furthermore, addressing the need for carefully choosing the regression step size, Bismor [92] derived a necessary condition for the convergence of the LMS algorithm. Other than providing convergence conditions, their study did not consider domain transform which is essential to the time-frequency control algorithm to be presented in the dissertation.

Research Objectives

The primary objective of this research is to develop a nonlinear time-frequency control concept for the control of time-delayed vibro-impact oscillators that are inherently nonlinear and non-stationary. A new time-delayed vibro-impact oscillator is formulated for the study. The wavelet-based nonlinear time-frequency control theory [36] is explored to develop a controller concept. Although it has been shown to be feasible for controlling a wide range of nonlinear systems, the convergence and controllability of the nonlinear time-frequency control theory is yet to be established. Setting the regression step size for the FxLMS algorithm is crucial for ensuring solution stability. If the step size is too small, convergence to the steady state solution could be too slow for the system identification to catch up to the unstable nonlinear system response, thus aggravating the error between the controlled output response and the desired target. As the secondary objective, this study examines mathematically the time-frequency control theory and derives the ranges of the regression step sizes, μ_1 and μ_2, that ensure fast convergence and solution stability of the controller design.

Due to the nature of this research, considerable challenges lie in the computational aspect of numerically integrating the governing equations. To fully resolve the underlying nonlinearity and to ensure convergence with accuracy, small integration time steps are required. Since the vibro-impact oscillator is inherent of grazing bifurcation and time-delayed characteristics, designing a viable controller to properly mitigate the system response is as involved as it is demanding. Due to the fact the time-frequency control theory is defined using continuous time functions, implementing the control algorithm using discrete series presents another challenge. The other challenge is to maintain a balance between the use of computing resources and the time required to facilitate proper control of the nonlinear time-delayed vibro-impact oscillator. These challenges necessitate an in-depth study of the solver algorithm to determine optimal optimization step sizes.

CHAPTER II

WAVELET BASED NONLINEAR TIME-FREQUENCY CONTROL THEORY WITH LOCAL ADAPTABILITY*

Three specific implications need be considered to properly control time-delayed vibro-impact oscillators. First, control needs be performed in the time- and frequency-domains simultaneously. Because the location and the stability of the equilibrium point vary in time when the system is undergoing route-to-chaos, it is hard to predict the system in high-dimension. For this very reason online system identification and control need to be conducted at the same time. As nonlinear systems undergoing route-to-chaos are very sensitive to initial conditions, a small perturbation can either render a system unstable or, as had demonstrated in many early studies of chaos control, restore stability. The three implications along with the Parseval's theorem, which states that the total energy computed in the time-domain equals the total energy computed in the frequency-domain, explicitly suggest incorporating time-domain control with frequency-domain measure.

---

*Part of this chapter is reprinted with permission from "A case of mitigating non-autonomous time-delayed system with cubic order feedback" by Chi-Wei Kuo, C. Steve Suh, 2017. Journal of the Franklin Institute, Volume 354, Pages 6651-6671, Copyright [2017] by Elsevier Ltd.

Adaptive Filter and Filtered-x LMS Algorithm

A control concept with physical features effective in addressing the identified properties is described in the section.

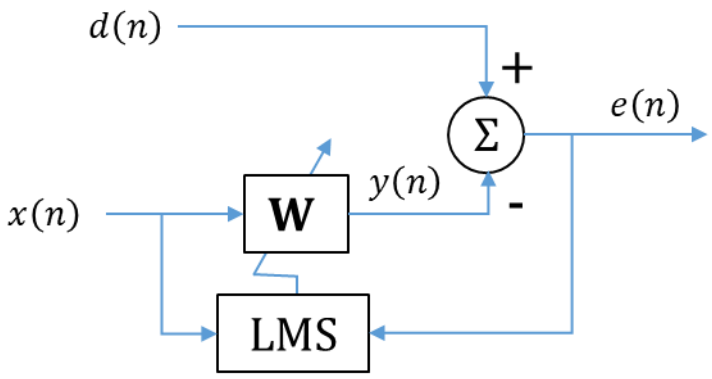

Figure 1 Schematic of an adaptive filter.

Before presenting the time-frequency control scheme, discrete-time FIR Wiener Filter and Least Mean Square (LMS) method should be mentioned. In Figure 1, the excitation sequence $\mathbf{x}(n)$ is modified by a filter, $\mathbf{W}$. The error signal, $e(n)$, is the difference between the system output, $y(n)$, and the desired response, $d(n)$. LMS algorithm is employed to optimize the mean-square value of $e(n)$ to update $\mathbf{W}$. Consider the instantaneous rough estimate of the performance function defined as follows

$$J(\mathbf{W}) = E\left[e^2(n)\right] \tag{2.1}$$

where the adaptive filter coefficient vector $\mathbf{W}$ is of the order of i

$$\mathbf{W}^{\mathbf{T}} = \begin{bmatrix} w_1 & w_2 & \cdots & w_i \end{bmatrix} \tag{2.2}$$

and the estimation error is therefore

$$e(n) = d(n) - \mathbf{W}^T \mathbf{x}(n) \tag{2.3}$$

To obtain the optimal filter coefficient $\mathbf{W}_0$, the gradient of the performance function must be zero

$$\nabla J(\mathbf{W}_0) = 0 \tag{2.4}$$

so that

$$\nabla J(\mathbf{W})\big|_{\mathbf{W}(n)} = -2d(n)\mathbf{x}(n) + 2\mathbf{x}(n)\mathbf{x}^T(n)\mathbf{W}(n) \tag{2.5}$$

The task which is updating the filter with the optimal set by solving Eq. (2.4) at each time step could have heavy computational cost when the filter length is large, and the input data rate is high. By implementing Gradient Descent optimization (non-linear regression), which is the tool of choice for finding the global minimum of the error performance surface, the computational complexity at each time step can be reduced. Gradient descent is a first-order iterative optimization algorithm and its solution strategy is to find the local minimum of a function by following the paths whose direction gradients are the steepest in the negative sense. This is progressively performed following an iterative scheme till the gradient of the solution vector is zero. By substituting Eq. (2.5) into the steepest gradient recursion,

$$\mathbf{W}(n+1) = \mathbf{W}(n) - (\mu/2)\nabla J(\mathbf{W}) \tag{2.6}$$

a new recursive scheme is obtained as a result

$$\mathbf{W}(n+1) = \mathbf{W}(n) + \mu \mathbf{x}(n) e(n) \tag{2.7}$$

Thus, LMS algorithm is a stochastic implementation of the steepest gradient method.

The adaptive filters running through the LMS algorithm are usually integrated into real-world applications such as the feedforward scheme depicted in Figure 2. By updating the weights, the filters can estimate input, track system response, and exert proper compensation to facilitate control of the plant. Modern day smart structures and bridges exploit this kind of active controllers to offset detrimental seismic trembles.

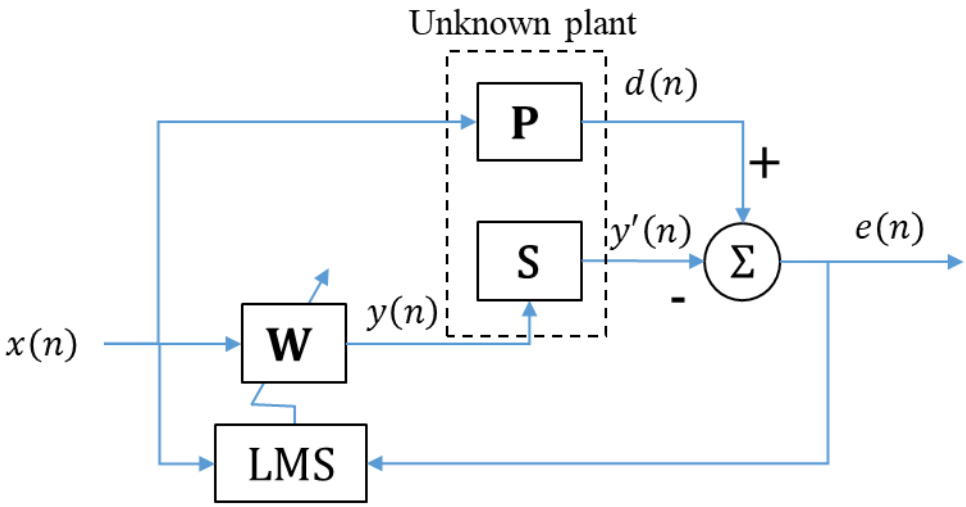

Figure 2 LMS-based adaptive system identification configuration.

In Figure 2, the LMS-based adaptive filter **W** is employed to identify the system. It estimates the response of the unknown plant **P** which is excited by the input, $x(n)$. Since the configuration in the schematic is an integral part of the real-world plant

such as a sensory or a nonautonomous subsystem, it requires a compensation, $\mathbf{S}$, which is the transfer function associated with the control mechanism. Control is applied in the adaptive algorithm by tracking the plant dynamics in time through updating the filter coefficients and minimizing the residual error $e(n)$ in the least mean-square sense. The primary path is defined by $\mathbf{P}(z)\mathbf{x}(z)$, and the secondary path by $\mathbf{S}(z)\mathbf{W}(z)\mathbf{x}(z)$. Thus, the error $e(n)$ is

$$e(n)=\left[\mathbf{P}(z)-\mathbf{S}(z)\mathbf{W}(z)\right]\mathbf{x}(z) \tag{2.8}$$

When the coefficient vector $\mathbf{W}(z)$ is of sufficient order and optimized, that is, $\mathbf{W}(z)=\mathbf{W}_0$, $e(n)$ converges to zero and the optimal transfer function $\mathbf{W}(z)$ is

$$\left[\mathbf{W}(z)\right]_{\mathbf{W}=\mathbf{W}_0}=P(z)/S(z) \tag{2.9}$$

There are two concerns related to the underlying attributes of the secondary path $\mathbf{S}(z)$ in Eq. (2.9). First, it is difficult to solve the inherent time-delay caused by $\mathbf{S}(z)$ if the primary path $\mathbf{P}(z)$ does not contain delays of the same time scale. Second, if $\mathbf{S}(\omega_c)=0$ at an unobservable control frequency, ω_c, it would render the equation mathematically singular and the systems physically unstable. To approximate $1/\mathbf{S}(z)$ with the secondary transfer function $\mathbf{S}(z)$ following the adaptive filter $\mathbf{W}(z)$, the LMS algorithm needs be modified and the filter must have sufficient length. As shown in Figure 3, running the input sequence $\mathbf{x}(n)$ through an auxiliary estimate filter $\hat{\mathbf{S}}(z)$

which is placed along the secondary path can effectively negate the noted negative effect. At the sum junction, the output error $e(n)$ is

$$e(n) = d(n) - \mathbf{S}(z) * \left[\mathbf{W}^T(z)\mathbf{x}(z) \right] \tag{2.10}$$

By substituting Eq. (2.10) into the steepest gradient recursion, $\mathbf{W}$ is updated by

$$\mathbf{W}(n+1) = \mathbf{W}(n) + \mu \mathbf{S}(n) * \mathbf{x}(n) e(n) \tag{2.11}$$

Eq. (2.11) shows that the adaptive updating scheme involves the $\mathbf{S}(n) * \mathbf{x}(n)$ term, indicating that $\mathbf{S}$ must also be placed in the filter length update path. In practice, $\mathbf{S}$ is unknown and must be estimated by an additional filter $\hat{\mathbf{S}}$ as in Figure 3.

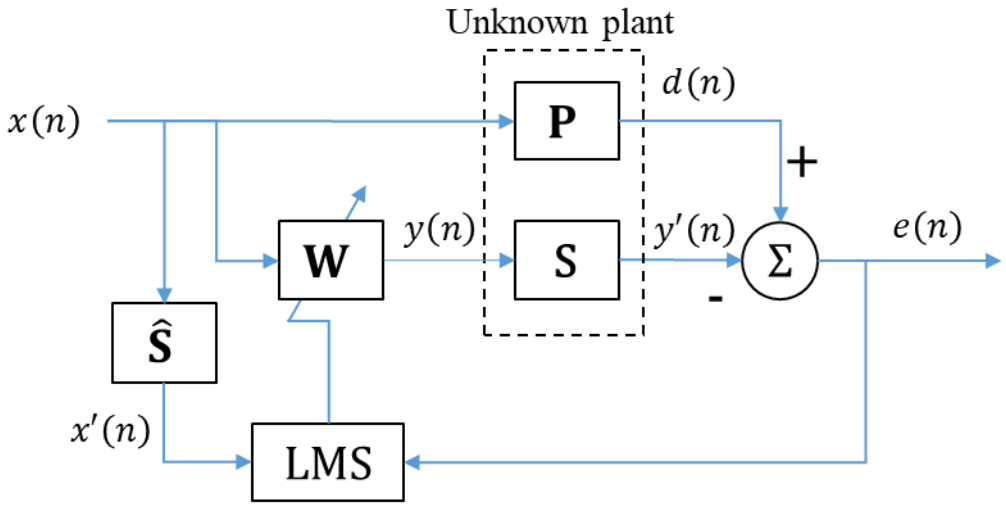

Figure 3 Scheme of Filtered-x LMS algorithm.

Wavelet Filter Banks

The concept of discrete wavelet transform (DWT) is central to the nonlinear time-frequency control to be developed in the next section. In the overall architecture of the time-frequency control, DWT decomposition serves to represent a dynamic response with different level of spectral resolution without losing the corresponding temporal information. Any anomaly indicative of perturbation or instability is identified and properly addressed in the wavelet domain. The conditioning of the response is realized by the adaptive FxLMS algorithm that updates the wavelet representations of the response. These representations are then synthesized to create a conditioned response as the control output that meets a specific control target. Having a fundamental knowledge of the working principle and implementation of DWT is therefore essential for developing a full comprehension for the nonlinear time-frequency control theory. As one of the physical components of nonlinear time-frequency control, the DWT decomposition algorithm and the corresponding synthesis algorithm incorporate a popular dyadic scheme. Various basic properties of DWT and inverse DWT render it possible for them to be implemented as digital filter banks for fast computing. These properties are best understood, and the underlying essences best presented, using the fundamental notions of multiresolution analysis (MRA). A concise while also relatively comprehensive discussion on wavelets is given in the followings.

Simultaneous time-frequency control is realized through manipulating discrete wavelet coefficients in the wavelet simultaneous time-frequency domain. Implementation of the unique and novel control idea includes incorporating DWT with

LMS adaptive filters to perform feedforward control and on-line identification by employing FxLMS to construct parallel adaptive filter banks. DWT in the time domain is realized by passing the input signal through a two-channel filterbank iteratively. Assume that the infinite input signal sequence $x[n]$ is of real numbers. The decomposition process convolutes the input $x[n]$ with a high-pass filter h_0 and a low pass filter h_1, followed by down-sampling by two. The approximation coefficient $a[n]$ and detail coefficient $d[n]$ it receives are calculated in the time-domain as follows

$$\begin{aligned} a[n] &= \sum_k h_0[2n-k]x[k] \\ &= \sum_k h_0[k]x[2n-k] \end{aligned} \tag{2.12}$$

$$\begin{aligned} d[n] &= \sum_k h_1[2n-k]x[k] \\ &= \sum_k h_1[k]x[2n-k] \end{aligned} \tag{2.13}$$

where integer $n = 0, \ldots, \infty$. Assume that the orthogonal sets are of equal and even length, and the lengths (or weights) of the high-pass filter h_0 and low-pass filter h_1 are both 4. Eqs. (2.12) and (2.13) are carried out by multiplying the signal with a linear transformation matrix, $\mathbf{T}_a$, as

$$\mathbf{Y} = \mathbf{T}_a\mathbf{X} \tag{2.14}$$

where the infinite analysis matrix, $\mathbf{T}_a$, has the high-pass filter $H[\cdot]$ and the low-pass filter $L[\cdot]$ as follow

$$\mathbf{T}_a = \begin{bmatrix} \ddots & \ddots & \ddots & \ddots & \ddots & \ddots & & & & & & \\ \cdots & 0 & H[3] & H[2] & H[1] & H[0] & 0 & 0 & 0 & 0 & 0 & \cdots \\ \cdots & 0 & 0 & 0 & H[3] & H[2] & H[1] & H[0] & 0 & 0 & 0 & \cdots \\ \cdots & 0 & 0 & 0 & 0 & 0 & H[3] & H[2] & H[1] & H[0] & 0 & \cdots \\ & \vdots & \vdots & \vdots & \vdots & \vdots & \vdots & \vdots & \vdots & \vdots & \vdots & \\ \cdots & 0 & L[3] & L[2] & L[1] & L[0] & 0 & 0 & 0 & 0 & 0 & \cdots \\ \cdots & 0 & 0 & 0 & L[3] & L[2] & L[1] & L[0] & 0 & 0 & 0 & \cdots \\ \cdots & 0 & 0 & 0 & 0 & 0 & L[3] & L[2] & L[1] & L[0] & 0 & \cdots \\ & & & & & & \ddots & \ddots & \ddots & \ddots & \ddots & \ddots \\ & & & & & & & & & & & \end{bmatrix} \tag{2.15}$$

and $\mathbf{X}$ is an infinite array of the input signal. $\mathbf{Y}$, which consists of wavelet approximation and detail coefficients, can be represented as

$$\mathbf{Y} = \begin{bmatrix} \cdots & a[0] & a[1] & a[2] & \cdots & d[0] & d[1] & d[2] & \cdots \end{bmatrix} \tag{2.16}$$

To prevent adding nonzero entries, the finite signal is assumed to be periodic and uses the values within the finite signal to replace the missing samples – a process called periodization. Thus for an input signal $\mathbf{X}$ of period N,

$$\mathbf{X} = \begin{bmatrix} \cdots & x[0] & x[1] & \cdots & x[N-1] & x[0] & x[1] & \cdots & x[N-1] & \cdots \end{bmatrix}^T \tag{2.17}$$

Eq. (2.17) can be truncated as follow

$$\mathbf{X}^N = \begin{bmatrix} x[0] & x[1] & \cdots & x[N-1] \end{bmatrix}^T \tag{2.18}$$

Because the transformed signal is also periodic of period N, N consecutive entries in $\mathbf{Y}$ are selected to represent it. Thus, a finite signal $\mathbf{X}^N$ is transformed into a finite signal $\mathbf{Y}^N$ of equal length. The analysis matrix T_a is also truncated to an $N \times N$ matrix, $\mathbf{T}_a^N$, to avoid extending the signal. The deleted filter coefficient in $\mathbf{T}_a^N$ is put back into

the proper position in the matrix to be consistent with the periodic signature of the signal. The transformation of Eq. (2.14) then becomes

$$\mathbf{Y}_{k+1}^{N} = \mathbf{T}_{a}^{N}\mathbf{X}_{k}^{N} \tag{2.19}$$

where k is the level of transformation (decomposition). Substituting truncated Eq. (2.15), Eq. (2.19) can be arranged to take up a concise form below

$$\begin{bmatrix}\mathbf{A}_{k+1}\\ \mathbf{D}_{k+1}\end{bmatrix} = \mathbf{T}_{a}^{N}\mathbf{X}_{k}^{N} \tag{2.20}$$

with

$$\mathbf{A}_{k+1} = \begin{bmatrix} a[0] & a[1] & \cdots & a[N/2-1]\end{bmatrix}^{T} \tag{2.21}$$

$$\mathbf{D}_{k+1} = \begin{bmatrix} d[0] & d[1] & \cdots & d[N/2-1]\end{bmatrix}^{T} \tag{2.22}$$

Simultaneous Time-Frequency Control

Figure 4 illustrates the adaptive concept featuring FxLMS in the control architecture where the least-mean-square (LMS) algorithm is modified by adding an adaptive filter to identify the system in real-time. The wavelet-based time-frequency controller thus constructed is capable of parallel on-line modeling. The filter adaptively adjusts the coefficients of a Finite-Impulse-Response (FIR) filter and the wavelet transformation matrix, **T**, is placed before the two FIR adaptive filters to decompose the time-domain discrete signal into its corresponding wavelet coefficient arrays. To characterize the input signal while also easing computational load, Daubechies-4 (db4) wavelet is employed.

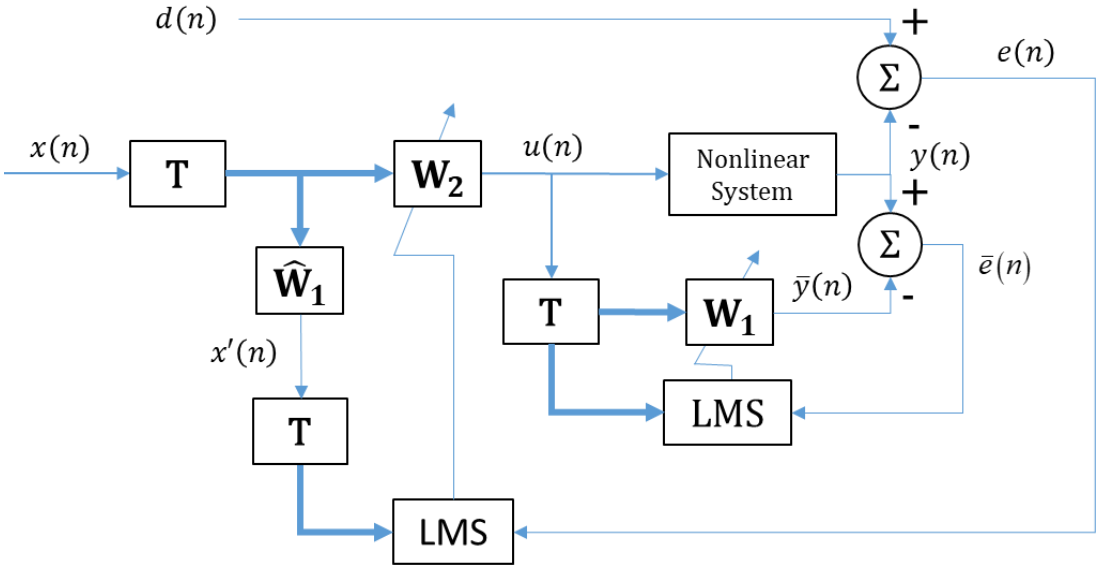

Figure 4 Wavelet based time-frequency control incorporating FxLMS.

$\mathbf{T}$ convolutes with the input sequence of length N

$$\mathbf{X}(n)=\begin{bmatrix} x(n) & x(n-1) & \cdots & x(n-N+1) \end{bmatrix}^T \tag{2.23}$$

to generate the approximation and detail coefficients at time step, n. Following the matrix $\mathbf{T}$ is the first adaptive filter which is used to model the dynamic system on-line. Its weight vector at time step n is

$$\mathbf{W}_1(n)=\begin{bmatrix} w_{1,1}(n) & w_{1,2}(n) & \cdots & w_{1,N}(n) \end{bmatrix}^T \tag{2.24}$$

The second adaptive filter serves as a feed-forward controller and its weight vector is

$$\mathbf{W}_2(n)=\begin{bmatrix} w_{2,1}(n) & w_{2,2}(n) & \cdots & w_{2,N}(n) \end{bmatrix}^T \tag{2.25}$$

The input control signal vector to the nonlinear system is

$$\mathbf{U}(n)=\begin{bmatrix} u(n) & u(n-1) & \cdots & u(n-N+1) \end{bmatrix}^T \tag{2.26}$$

with

$$u(n) = \mathbf{W}_1^T(n)\mathbf{T}\mathbf{X}(n) \tag{2.27}$$

The error sequence $e[n]$ is obtained by subtracting the desired signal $d[n]$ from $y[n]$ which is the output from the time-delayed vibro-impact oscillator

$$e(n) = d(n) - y(n) \tag{2.28}$$

The weights of the adaptive filter $\mathbf{W}_2(n)$ are updated by using the LMS algorithm as follow

$$\mathbf{W}_2(n+1) = \mathbf{W}_2(n) + \mu_2 \mathbf{T}\mathbf{X}'(n)e(n) \tag{2.29}$$

with μ_2 being the optimization step size and $\mathbf{X}'(n)$ the compensated output signal vector output from the FIR filter $\hat{\mathbf{W}}_1$,

$$\mathbf{X}'(n) = \begin{bmatrix} x'(n) & x'(n-1) & \cdots & x'(n-N+1) \end{bmatrix}^T \tag{2.30}$$

which is calculated through the operation below

$$x'(n) = \mathbf{W}_1^T \mathbf{T}\mathbf{X}(n) \tag{2.31}$$

The identification error $\bar{e}(n)$ between $y(n)$ and the reconstructed signal $\bar{y}(n)$ is

$$\bar{e}(n) = y(n) - \bar{y}(n) \tag{2.32}$$

where the reconstructed signal $\bar{y}(n)$ is

$$\bar{y}(n) = \mathbf{W}_1^T(n)\mathbf{T}\mathbf{U}(n) \tag{2.33}$$

Afterward $\bar{e}(n)$ is used to update the weights of the adaptive filter $\mathbf{W}_1(n)$ following the least-mean-square algorithm

$$\mathbf{W}_1(n+1) = \mathbf{W}_1(n) + \mu_1 \mathbf{TU}(n)\bar{e}(n) \tag{2.34}$$

where μ_1 is the optimization step size.

Local Adaptability to Nonlinear and Nonstationary Response

Adaptable Optimization Step Size for System Identification

Assume that signals u(n) and y(n) are both discrete and finite-valued in the real domain. Substitute Eq. (2.32) into Eq. (2.34) to result in

$$\mathbf{W}_1(n+1) = \mathbf{W}_1(n) + \mu_1 \mathbf{TU}(n)\left[y(n) - \bar{y}(n)\right] \tag{2.35}$$

$$\mathbf{W}_1(n+1) = \left[1 - \mu_1 \mathbf{TU}(n)\left[\mathbf{TU}(n)\right]^T\right]\mathbf{W}_1(n) + \mu_1 \mathbf{TU}(n)\, y(n) \tag{2.36}$$

Eq. (2.36) is of the form

$$\mathbf{x}(n+1) = \mathbf{A}(n)\mathbf{x}(n) + \mathbf{B}(n)\, y(n) \tag{2.37}$$

in which

$$\mathbf{A}(n) = 1 - \mu_1 \mathbf{TU}(n)\left[\mathbf{TU}(n)\right]^T \tag{2.38}$$

For a discrete, stationary system the condition below warrants instability [92]

$$\mathrm{tr}\left(|\mathbf{A}|\right) = \sum_{i=1}^{N} |a_{ii}| > N \tag{2.39}$$

where a_{ii} is the $i-th$ element on the diagonal of the state matrix $\mathbf{A}$, and N is the size of matrix $\mathbf{A}$. The stability of a discrete system requires that all the eigenvalues of the

system state matrix $\mathbf{A}$ are within the unit disk. In addition, the trace of the matrix equals to the sum of its eigenvalues. Thus, a trace greater than the size of the matrix means that at least one eigenvalue of the matrix is greater than one.

Combining Eqs. (2.38) and (2.39), the divergence sufficient condition for the adaptive LMS filter can be formulated as:

$$\mathrm{tr}\left(\left|1-\mu_1\mathbf{TU}(n)\left[\mathbf{TU}(n)\right]^T\right|\right)=\sum_{i=1}^{N}\left|1-\mu_1\left[TU(n-i)\right]^2\right|>N \tag{2.40}$$

provided that N is sufficiently large. If the condition in Eq. (2.40) is true for a limited number of samples and becomes false afterwards, the filter may still remain convergent. Therefore, the convergence necessary condition is

$$\sum_{i=1}^{N}\left|1-\mu_1\left[\mathbf{TU}(n-i)\right]^2\right|\le N \tag{2.41}$$

Numerical simulations showed that step sizes chosen close to violating the condition in Eq. (2.41) resulted in large excessive mean square errors (MSE) and abrupt growth of filter coefficients. Therefore, it would be prudent to strengthen this condition by mandating that

$$\underset{0\le i\le N-1}{\forall}\left|1-\mu_1\left[\mathbf{TU}(n-i)\right]^2\right|\le 1 \tag{2.42}$$

Note that when the left-hand side of the inequality is fulfilled, the right-hand side of the inequality holds, but the opposite relation is not necessarily true. The left-hand side of Eq. (2.42) can be expressed as

$$\underset{0\le i\le N-1}{\forall}-1\le 1-\mu_1\left[\mathbf{TU}(n-i)\right]^2\le 1 \tag{2.43}$$

Thus, for real-number input data, considering that the above inequality should hold throughout the whole adaptation, the condition can be restated as

$$\underset{n}{\forall}\, 0 \le \mu_1 \le \frac{2}{\left[\mathbf{TU}(n-i)\right]^2} \tag{2.44}$$

The above condition specifies the upper limit on the step size when a fast adaptation is needed. It also serves as a basis for a preliminary choice of the step size.

Adaptable Optimization Step Size for Input Control

To derive the optimized step size for input force control, rotated variable must be used. The correlation matrix of the input signal [91]

$$\mathbf{R} = E\left\{\mathbf{X}_T(n)\mathbf{X}_T{}^T(n)\right\} \tag{2.45}$$

can be decomposed as

$$\mathbf{R} = \mathbf{F}\boldsymbol{\Lambda}\mathbf{F}^T \tag{2.46}$$

where $\mathbf{X}_T(n)$ is the input sequence after wavelet transform, $\mathbf{F}$ is the eigenvector matrix and $\boldsymbol{\Lambda}$ is a diagonal matrix with eigenvalues λ

$$\boldsymbol{\Lambda} = diag\left(\lambda_0\lambda_1...\lambda_{L-1}\right) \tag{2.47}$$

Hence, the input vector can be rotated as

$$\mathbf{z}(n) \triangleq \mathbf{F}^T\mathbf{X}_T(n) \tag{2.48}$$

and the rotated filtered input vector can be defined as

$$\mathbf{z}_f(n) = \mathbf{F}^T\mathbf{X}_f(n) \tag{2.49}$$

where $\mathbf{X}_f(n)$ is obtained by filtering $\mathbf{X}_T(n)$ through the wavelet transform filter $\mathbf{W}_{1T}$ that is of the order of $Q-1$

$$\mathbf{X}_f(n) = \sum_{q=0}^{Q-1} w_{1T,q} \mathbf{X}_T(n-q) \tag{2.50}$$

Note that $\mathbf{W}_{1T}(n) = \left[w_{1T,1}(n) \quad w_{1T,2}(n) \quad \cdots \quad w_{1T,Q-1}(n) \right]^T$. Multiplying both sides of Eq. (2.50) by $\mathbf{F}^T$

$$\mathbf{z}_f(n) = \sum_{q=0}^{Q-1} w_{1T,q} \mathbf{z}(n-q) \tag{2.51}$$

The rotated error weight vector $\mathbf{c}(n)$ is defined as

$$\mathbf{c}(n) \triangleq \mathbf{F}^T \left[\mathbf{W}_2(n) - \mathbf{W}_{2,opt} \right] \tag{2.52}$$

where $\mathbf{W}_{2,opt}$ denotes the optimized filter weight vector. Using Eq. (2.52), Eq. (2.29) can be transformed into the rotated domain as

$$\mathbf{c}(n+1) = \mathbf{c}(n) + \mu_2 e(n) \mathbf{z}_f(n) \tag{2.53}$$

Similarly, $e(n)$ given by Eq. (2.28) can be expressed as

$$e(n) = d(n) - \sum_{q=0}^{Q-1} w_{1T,q} \mathbf{W}_2^T(n-q) \mathbf{X}_T(n-q) \tag{2.54}$$

Eq. (2.54) can be further simplified through the following manipulations

$$
\begin{aligned}
e(n) &= d(n) - \sum_{q=0}^{Q-1} w_{1T,q} \mathbf{W}_2^T (n-q) \mathbf{X}_T (n-q) \\
&= d(n) - \sum_{q=0}^{Q-1} w_{1T,q} \left[\mathbf{W}_2^T (n-q) - \mathbf{W}_{2,opt}^T + \mathbf{W}_{2,opt}^T \right] \mathbf{X}_T (n-q) \\
&= d(n) - \sum_{q=0}^{Q-1} w_{1T,q} \mathbf{W}_{2,opt}^T \mathbf{X}_T (n-q) - \sum_{q=0}^{Q-1} W_{1T,q} \left[\mathbf{W}_2^T (n-q) - \mathbf{W}_{2,opt}^T \right] \mathbf{X}_T (n-q) \\
&= e_{opt}(n) - \sum_{q=0}^{Q-1} w_{1T,q} \left[\mathbf{W}_2^T (n-q) - \mathbf{W}_{2,opt}^T \right] \mathbf{F}^T \mathbf{F} \mathbf{X}_T (n-q) \\
&= e_{opt}(n) - \sum_{q=0}^{Q-1} w_{1T,q} \mathbf{c}^T (n-q) \mathbf{z}(n-q)
\end{aligned}
\tag{2.55}
$$

where $e_{opt}(n)$ is the difference between $d(n)$ and $\mathbf{W}_{2,OPT} \mathbf{X}_f(n)$. Combing Eq. (2.4) with Eq. (2.55), the MSE can be expressed in terms of the rotated variables as

$$
J(n) = J_{\min} + J_{ex}(n) \tag{2.56}
$$

where the minimum MSE $J_{\min}$ is

$$
J_{\min} \triangleq E\left[e_{opt}^2(n) \right] \tag{2.57}
$$

and the excess MSE (EMSE) $J_{ex}(n)$ is

$$
J_{ex}(n) = \sum_{q=0}^{Q-1} w_{1T,q}^2 E\left\{ \mathbf{c}^T (n-q) \Lambda \mathbf{c}(n-q) \right\} \tag{2.58}
$$

A detail derivation of Eq. (2.58) can be found in Appendix A. Consequently the EMSE at the next time step is

$$
J_{ex}(n+1) = \sum_{q=0}^{Q-1} w_{1T,q}^2 E\left\{ \mathbf{c}^T (n+1-q) \Lambda \mathbf{c}(n+1-q) \right\} \tag{2.59}
$$

where $c(n+1-q)$ can be expressed using Eq. (2.53) as

$$\mathbf{c}(n+1-q)=\mathbf{c}(n-q)+\mu_2\mathbf{z}_f(n-q)e(n-q) \tag{2.60}$$

Substituting Eq. (2.60) into Eq. (2.59) to get $J_{ex}(n+1)$ as follows

$$\begin{aligned} J_{ex}(n+1)=&\sum_{q=0}^{Q-1}w_{1T,q}^2E\left\{\mathbf{c}^T(n-q)\mathbf{\Lambda}\mathbf{c}(n-q)\right\}\\ &+2\mu_2\sum_{q=0}^{Q-1}w_{1T,q}^2E\left\{\mathbf{c}^T(n-q)\mathbf{\Lambda}\mathbf{z}_f(n-q)e(n-q)\right\}\\ &+\mu_2^2\sum_{q=0}^{Q-1}w_{1T,q}^2E\left\{\mathbf{z}_f^T(n-q)e(n-q)\mathbf{\Lambda}e(n-q)\mathbf{z}_f(n-q)\right\}\end{aligned} \tag{2.61}$$

With the first term being Eq. (2.58), Eq. (2.61) can be expressed as

$$J_{ex}(n+1)=J_{ex}(n)+2\mu_2\beta(n)+\mu_2^2\eta(n) \tag{2.62}$$

where

$$\beta(n)\triangleq\sum_{q=0}^{Q-1}w_{1T,q}^2E\left\{\mathbf{c}^T(n-q)\mathbf{\Lambda}\mathbf{z}_f(n-q)e(n-q)\right\} \tag{2.63}$$

$$\eta(n)\triangleq\sum_{q=0}^{Q-1}w_{1T,q}^2E\left\{e^2(n-q)\mathbf{z}_f^T(n-q)\Lambda\mathbf{z}_f(n-q)\right\} \tag{2.64}$$

To evaluate $J_{ex}(n+1)$, $\beta(n)$ and $\eta(n)$ need be solved. To solve $\beta(n)$, the following scale function $b(n)$ is defined

$$b(n)\triangleq E\left\{\mathbf{c}^T(n)\mathbf{\Lambda}\mathbf{z}_f(n)e(n)\right\} \tag{2.65}$$

Substituting Eq. (2.55) into Eq. (2.65), $b(n)$ is derived to look

$$\begin{aligned} b(n)&=E\left\{\mathbf{c}^T(n)\mathbf{\Lambda}\mathbf{z}_f(n)\left[e_{opt}(n)-\sum_{p=0}^{Q-1}w_{1T,p}\mathbf{c}^T(n-p)\mathbf{z}(n-p)\right]\right\}\\ &=E\left\{\mathbf{c}^T(n)\mathbf{\Lambda}\mathbf{z}_f(n)e_{opt}(n)\right\}-\sum_{p=0}^{Q-1}w_{1T,p}E\left\{\mathbf{c}^T(n)\mathbf{\Lambda}\mathbf{z}_f(n)\mathbf{c}^T(n-p)\mathbf{z}(n-p)\right\}\end{aligned} \tag{2.66}$$

Since $e_{opt}(n)$ is a zero mean vector and statically independent of $\mathbf{z}$ and $\mathbf{c}$, the first term in Eq. (2.66) is approximately zero. The second term, $\mathbf{c}^T(n-p)\mathbf{z}(n-p)$, can be transposed and substituted. Thus,

$$b(n) = -\sum_{p=0}^{Q-1} w_{1T,p} E\left\{\mathbf{c}^T(n)\Lambda\mathbf{z}_f(n)\mathbf{z}^T(n-p)\mathbf{c}(n-p)\right\} \tag{2.67}$$

According to the independence assumption, the correlation matrix between different vectors of a stationary input signal can be approximated as

$$E\left\{\mathbf{X}_T(n-p)\mathbf{X}_T^T(n-q)\right\} = \delta_{p,q}\mathbf{R} \tag{2.68}$$

where $\delta_{p,q}$ is the Kronecker Delta function. Substitute Eq. (2.55) into Eq. (2.68) to have

$$E\left\{\mathbf{X}_T(n-p)\mathbf{X}_T^T(n-q)\right\} = \delta_{p,q}\mathbf{F}\mathbf{\Lambda}\mathbf{F}^T \tag{2.69}$$

Eq. (2.69) can be manipulated to look

$$\mathbf{F}^T E\left\{\mathbf{X}_T(n-p)\mathbf{X}_T^T(n-q)\right\}\mathbf{F} = \delta_{p,q}\mathbf{F}^T\mathbf{F}\mathbf{\Lambda}\mathbf{F}^T\mathbf{F} \tag{2.70}$$

With $\mathbf{F}$ being a rotation matrix and its inverse equal to its transpose, Eq. (2.70) can be expressed as

$$E\left\{\mathbf{F}^T\mathbf{X}_T(n-p)\mathbf{X}_T^T(n-q)\mathbf{F}\right\} = \delta_{p,q}\mathbf{\Lambda} \tag{2.71}$$

Substituting Eq. (2.57) into Eq. (2.71) to obtain

$$E\left\{\mathbf{z}(n-p)\mathbf{z}^T(n-q)\right\} = \delta_{p,q}\mathbf{\Lambda} \tag{2.72}$$

Combining Eq. (2.50) and Eq. (2.72),

$$E\left\{\mathbf{z}_f\left(n\right)\mathbf{z}^T\left(n-p\right)\right\} = E\left\{\left[\sum_{q=0}^{Q-1} w_{1T,q}\mathbf{z}\left(n-q\right)\right]\mathbf{z}^T\left(n-p\right)\right\}$$
$$= \sum_{q=0}^{Q-1} w_{1T,q} E\left\{\mathbf{z}\left(n-q\right)\mathbf{z}^T\left(n-p\right)\right\} \tag{2.73}$$
$$= \sum_{q=0}^{Q-1} w_{1T,q}\Lambda\delta_{p,q} = w_{1T,p}\Lambda$$

With the assumption that $\mathbf{z}$ and $\mathbf{c}$ are statically independent, Eq. (2.67) can be reduced to the following by substituting Eq. (2.73)

$$b\left(n\right) = -\sum_{p=0}^{Q-1} w_{1T,p}^2 E\left\{\mathbf{c}^T\left(n\right)\Lambda^2\mathbf{c}\left(n-p\right)\right\} \tag{2.74}$$

When the eigenvalues of the input signal's correlation matrix are nearly equal, Λ^2 can be approximated as

$$\Lambda^2 \approx \lambda_{av}\Lambda \tag{2.75}$$

where λ_{av} is the average of the eigenvalues. Therefore, Eq. (2.74) can be reduced to

$$b\left(n\right) = -\lambda_{av}\sum_{p=0}^{Q-1} w_{1T,p}^2 E\left\{\mathbf{c}^T\left(n\right)\Lambda\mathbf{c}\left(n-p\right)\right\} \tag{2.76}$$

Define $r_p\left(n\right)$ as

$$r_p\left(n\right) \triangleq E\left\{\mathbf{c}^T\left(n\right)\Lambda\mathbf{c}\left(n-p\right)\right\} \tag{2.77}$$

The rotated error weight vector $\mathbf{c}\left(n\right)$ defined in Eq. (2.53) can be approximated using

$$\mathbf{c}\left(n\right) \approx \mathbf{c}^T\left(n-p\right) + \mu_2 p\mathbf{z}_f^T\left(n-p\right)e\left(n-p\right) \tag{2.78}$$

Substituting Eq. (2.78) into Eq. (2.77), one has

$$
\begin{aligned}
r_p(n) &= E\left\{\left[\mathbf{c}^T(n-p) + 2\mu_2 p\mathbf{z}_f^T(n-p)e(n-p)\right]\Lambda\mathbf{c}(n-p)\right\} \\
&= E\left\{\mathbf{c}^T(n-p)\Lambda\mathbf{c}(n-p)\right\} + 2\mu_2 pE\left\{\mathbf{z}_f^T(n-p)\Lambda\mathbf{c}(n-p)e(n-p)\right\} \\
&= E\left\{\mathbf{c}^T(n-p)\Lambda\mathbf{c}(n-p)\right\} + 2\mu_2 pE\left\{\mathbf{c}^T(n-p)\Lambda\mathbf{z}_f(n-p)e(n-p)\right\}
\end{aligned}
\tag{2.79}
$$

After applying Eq. (2.65) to Eq. (2.79), $r_p(n)$ is reduced to

$$
r_p(n) = E\left\{\mathbf{c}^T(n)\Lambda\mathbf{c}(n)\right\} + \mu_2\rho b(n-p) \tag{2.80}
$$

Eq. (2.81) is resulted after incorporating Eq. (2.80) into Eq. (2.76)

$$
b(n) = -\lambda_{av}\sum_{p=0}^{Q-1} w_{1T,p}^2 E\left\{\mathbf{c}^T(n-p)\Lambda\mathbf{c}(n-p)\right\} - \lambda_{av}\mu_2\sum_{p=0}^{Q-1} pw_{1T,p}^2 b(n-p) \tag{2.81}
$$

Per Eq. (2.58), the first term in Eq. (2.81) is replaced with $-\lambda_{av}J_{ex}(n)$ to get

$$
b(n) = -\lambda_{av}J_{ex}(n) - \lambda_{av}\mu_2\sum_{p=0}^{Q-1} pw_{1T,p}^2 b(n-p) \tag{2.82}
$$

Using the recursive property of Eq. (2.82), $b(n)$ can be expanded further

$$
\begin{aligned}
b(n) &= -\lambda_{av}J_{ex}(n) - \lambda_{av}\mu_2\sum_{p=0}^{Q-1} pw_{1T,p}^2 \times \left[-\lambda_{av}J_{ex}(n-p) - \lambda_{av}\mu_2\sum_{q=0}^{Q-1} qw_{1T,q}^2 b(n-p-q)\right] \\
&= -\lambda_{av}J_{ex}(n) + \lambda_{av}^2\mu_2\sum_{p=0}^{Q-1} pw_{1T,p}^2 J_{ex}(n-p) + \lambda_{av}^2\mu_2^2\sum_{p=0}^{Q-1}\sum_{q=0}^{Q-1} pqw_{1T,p}^2 w_{1T,q}^2 b(n-p-q)
\end{aligned}
\tag{2.83}
$$

The third term in Eq. (2.83) can be neglected if $0 < \mu_2 \ll 1$ which gives $\mu_2^2 \approx 0$. Thus,

$$
b(n) \approx -\lambda_{av}J_{ex}(n) + \lambda_{av}^2\mu_2\sum_{p=0}^{Q-1} pw_{1T,p}^2 J_{ex}(n-p) \tag{2.84}
$$

By substituting Eq. (2.84) into Eq. (2.65), Eq. (2.63) becomes

$$\begin{aligned}\beta(n) &= \sum_{q=0}^{Q-1} w_{1T,q}^2 b(n-q) \\ &= -\lambda_{av} \sum_{q=0}^{Q-1} w_{1T,q}^2 J_{ex}(n-q) + \lambda_{av}^2 \mu_2 \sum_{q=0}^{Q-1} w_{1T,q}^2 \sum_{p=0}^{Q-1} p w_{1T,p}^2 J_{ex}(n-p-q)\end{aligned} \tag{2.85}$$

In case of adaptation, it can be assumed that

$$J_{ex}(n-q-p) \approx J_{ex}(n-q) \tag{2.86}$$

Then, $\beta(n)$ can be further approximated as

$$\beta(n) \approx -\lambda_{av} \sum_{q=0}^{Q-1} w_{1T,q}^2 J_{ex}(n-q) + \lambda_{av}^2 \mu_2 \sum_{q=0}^{Q-1} w_{1T,q}^2 \sum_{p=0}^{Q-1} p w_{1T,p}^2 J_{ex}(n-q) \tag{2.87}$$

Finally, $\beta(n)$ can be expressed as

$$\beta(n) \approx \lambda_{av}\left(\lambda_{av} \tau_s^2 \mu - 1\right) \sum_{q=0}^{Q-1} w_{1T,q}^2 J_{ex}(n-q) \tag{2.88}$$

where

$$\tau_s^2 \triangleq \sum_{p=0}^{Q-1} p w_{1T,q}^2 \tag{2.89}$$

From Eq. (2.64), $\eta(n)$ can be derived to have the following forms

$$\begin{aligned}\eta(n) &= \sum_{q=0}^{Q-1} w_{1T,q}^2 E\left\{e^2(n-q)\mathbf{z}_f^T(n-q)\Lambda \mathbf{z}_f(n-q)\right\} \\ &= \sum_{q=0}^{Q-1} w_{1T,q}^2 E\left\{e^2(n-q)\sum_{l=0}^{L-1} \lambda_l z_f^2(n-q-l)\right\} \\ &= \sum_{q=0}^{Q-1}\sum_{l=0}^{L-1} \lambda_l w_{1T,q}^2 E\left\{e^2(n-q) z_f^2(n-q-l)\right\}\end{aligned} \tag{2.90}$$

where $z_f^2(n-q-l)$ is the $l-th$ element of $\mathbf{z}_f(n-q)$ and λ_l is the $l-th$ eigenvalue of $\mathbf{\Lambda}$. According to the separation principle [91], $x_T^2(n)$ and $e^2(n)$ are statically

independent. Consequently, $z_f^2(n)$ and $e^2(n)$ are independent. Following this assumption, Eq. (2.90) is simplified to read

$$\eta(n) = \sum_{q=0}^{Q-1}\sum_{l=0}^{L-1} \lambda_l w_{1T,q}^2 \underbrace{E\left\{e^2(n-q)\right\}}_{J(n-q)} \underbrace{E\left\{z_f^2(n-q-l)\right\}}_{P_{x_f}} \tag{2.91}$$

By definition, $E\left\{e^2(n-q)\right\}$ is equal to the MSE at time $n-q$ and the term $E\left\{z_f^2(n-q-l)\right\}$ is the power of the filtered input signal, p_{xf}. Therefore,

$$\begin{aligned}\eta(n) &= \sum_{q=0}^{Q-1}\sum_{l=0}^{L-1} \lambda_l w_{1T,q}^2 P_{x_f} J(n-q) \\ &= P_{x_f}\left[\sum_{l=0}^{L-1}\lambda_l\right]\sum_{q=0}^{Q-1} w_{1T,q}^2 J(n-q) \\ &= P_{x_f} L\lambda_{av}\sum_{q=0}^{Q-1} w_{1T,q}^2 J(n-q)\end{aligned} \tag{2.92}$$

By using Eq. (2.56), $\eta(n)$ can eventually be expressed as

$$\eta(n) = LP_{x_f}\lambda_{av}\sum_{q=0}^{Q-1} w_{1T,q}^2\left[J_{\min} + J_{ex}(n-q)\right] \tag{2.93}$$

To predict EMSE, by substituting Eq. (2.88) and Eq. (2.93) into Eq. (2.62), it can be expressed as

$$\begin{aligned}J_{ex}(n+1) = J_{ex}(n) &+ 2\mu_2\lambda_{av}\left(\lambda_{av}\tau_s^2\mu_2 - 1\right)\sum_{q=0}^{Q-1} w_{1T,q}^2 J_{ex}(n-q) \\ &+ \mu_2^2 LP_{x_f}\lambda_{av}\sum_{q=0}^{Q-1} w_{1T,q}^2\left[J_{\min} + J_{ex}(n-q)\right]\end{aligned} \tag{2.94}$$

In Eq. (2.94), λ_{av} can be calculated using

$$\lambda_{av} = \frac{1}{L}\sum_{l=0}^{L-1}\lambda_l = \frac{1}{L}tr(\mathbf{\Lambda}) = \frac{1}{L}tr\left(E\left\{\mathbf{z}\mathbf{z}^T\right\}\right) = \frac{1}{L}\sum_{l=0}^{L-1} E\left\{z^2(n-1)\right\} = P_z \tag{2.95}$$

where P_z is the power of the rotated input signal. Because $P_z = P_x$, the power of the input signal, thus

$$\lambda_{av} = P_x \tag{2.96}$$

In addition, the power of the filtered input signal is

$$\begin{aligned} P_{x_f} &= E\left\{x_f^2(n)\right\} = E\left\{\sum_{p=0}^{Q-1} w_{1T,p} x_T(n-p) \sum_{q=0}^{Q-1} w_{1T,q} x_T(n-q)\right\} \\ &= \sum_{p=0}^{Q-1}\sum_{q=0}^{Q-1} w_{1T,p} w_{1T,q} E\left\{x_T(n-p) x_T(n-q)\right\} \end{aligned} \tag{2.97}$$

If $p \neq q$, $E\left\{x_T(n-p) x_T(n-q)\right\} = 0$. As such, Eq. (2.97) can be reduced to

$$P_{x_f} = \sum_{p=0}^{Q-1} w_{1T,p}^2 E\left\{x_T^2(n-p)\right\} = \sum_{p=0}^{Q-1} w_{1T,p}^2 P_x \tag{2.98}$$

Combining Eq. (2.96) and Eq. (2.98), one has

$$P_{x_f} = \sigma_s^2 \lambda_{av} \tag{2.99}$$

where

$$\sigma_s^2 \triangleq \sum_{p=0}^{Q-1} w_{1T,p}^2 \tag{2.100}$$

Using $\lambda_{av} = \sigma_s^{-2} P_{x_f}$ to simplify $J_{ex}(n+1)$

$$\begin{aligned} J_{ex}(n+1) = J_{ex}(n) &+ 2\mu_2 \sigma_s^{-2} P_{x_f}\left(\sigma_s^{-2} P_{x_f} \tau_s^2 \mu - 1\right) \sum_{q=0}^{Q-1} w_{1T,q}^2 J_{ex}(n-q) \\ &+ \mu_2^2 L \sigma_s^{-2} P_{x_f}^2 \sum_{q=0}^{Q-1} w_{1T,q}^2 \left[J_{\min} + J_{ex}(n-q)\right] \end{aligned} \tag{2.101}$$

Let

$$\Delta_{eq} \triangleq \frac{\tau_s^2}{\sigma_s^2} \tag{2.102}$$

$J_{ex}(n+1)$ can be further simplified to be

$$\begin{aligned} J_{ex}(n+1) = J_{ex}(n) + 2\mu_2\sigma_s^{-2}P_{x_f}\left(P_{x_f}\Delta_{eq}\mu - 1\right)\sum_{q=0}^{Q-1} w_{1T,q}^2 J_{ex}(n-q) \\ + \mu_2^2 L\sigma_s^{-2}P_{x_f}^2\sum_{q=0}^{Q-1} w_{1T,q}^2\left[J_{\min} + J_{ex}(n-q)\right] \end{aligned} \tag{2.103}$$

Using the following defined scalar parameters m and h

$$m \triangleq \mu_2 P_{x_f}\sigma_s^{-2}\left[2 - \mu_2 P_{x_f}\left(L + 2\Delta_{eq}\right)\right] \tag{2.104}$$

and

$$h \triangleq \mu_2^2 P_{x_f}^2 L J_{\min} \tag{2.105}$$

$J_{ex}(n+1)$ in Eq. (2.103) is expressed as

$$J_{ex}(n+1) = J_{ex}(n) - m\sum_{q=0}^{Q-1} w_{1T,q}^2 J_{ex}(n-q) + h \tag{2.106}$$

which is a novel model for the prediction of FxLMS convergence. A general FxLMS convergence condition is derived in the followings using Eq. (2.106). When FxLMS converges, the optimal EMSE, which is a minimum value, can be obtained for the steady state when $n \to \infty$. In this condition, it can be assumed that

$$J_{ex}(n+1) = J_{ex}(n) = \ldots = J_{ex}(n-q) = J_{ex,\min} \tag{2.107}$$

Based on this assumption, Eq. (2.106) can be reduced to

$$J_{ex,\min} = J_{ex,\min} - m\sum_{q=0}^{Q-1} w_{1T,q}^2 J_{ex,\min} + h \tag{2.108}$$

Then, the optimum EMSE can be obtained as

$$J_{ex,\min} = \frac{h}{m\sigma_s^2} \tag{2.109}$$

By substituting Eq. (2.104) and Eq. (2.105) into Eq. (2.109), $J_{ex,\min}$ can be expressed as

$$J_{ex,\min} = \frac{\mu_2 P_{x_f} L J_{\min}}{2 - \mu_2 P_{x_f} \left(L + 2\Delta_{eq}\right)} \tag{2.110}$$

For a system to converge, it is necessary that the corresponding $J_{ex,\min}$ is positive. This requires that

$$\mu_2 < \frac{2}{P_{x_f} \left(L + 2\Delta_{eq}\right)} \tag{2.111}$$

The condition in Eq. (2.111) is also a sufficient condition for the convergence of the FxLMS algorithm. Based on the same necessary condition as in the steady state, $J_{ex}(n)$ in Eq. (2.58) is a positive function of $\mathbf{c}(n)$ that,

$$J_{ex}(n) > 0 \quad \forall n \tag{2.112}$$

According to Lyapunov stability theory, if for some μ_2, the difference of $J_{ex}(n)$ is negative such as

$$\Delta J_{ex}(n) = J_{ex}(n+1) - J_{ex}(n) < 0 \quad \forall n \tag{2.113}$$

then $J_{ex}(n)$ is a Lyapunov function and the system is uniformly asymptotically stable in the Lyapunov sense. In this case, the system converges to its equilibrium point at the origin, i.e. $\mathbf{c}(n) \to 0$. From Eq. (2.52), it can be shown that when $\mathbf{c}(n) \to 0$, the adaptive

filter weight converges to the optimum filter weight, i.e. $\mathbf{W}_2(n) \to \mathbf{W}_{2,opt}$. Therefore, it can be stated that $\Delta J_{ex}(n) < 0$ is a sufficient condition for FxLMS convergence.

$\Delta J_{ex}(n)$ is also negative. When the algorithm is far from being convergent, EMSE is greater than its steady state value, $J_{ex} > J_{ex,\min}$. Therefore,

$$J_{ex}(n) > \frac{h}{m\sigma_s^2} \quad \forall n \tag{2.114}$$

Apply $\sum_{q=0}^{Q-1} w_{1T,q}^2$ to both sides of Eq. (2.114)

$$\sum_{q=0}^{Q-1} w_{1T,q}^2 J_{ex}(n-q) > \sum_{q=0}^{Q-1} w_{1T,q}^2 \frac{h}{m\sigma_s^2} \tag{2.115}$$

Eq. (2.115) is equivalent to

$$\sum_{q=0}^{Q-1} w_{1T,q}^2 J_{ex}(n-q) > \frac{h}{m} \tag{2.116}$$

If $m > 0$ then Eq. (2.116) can be rewritten as

$$-m\sum_{q=0}^{Q-1} w_{1T,q}^2 J_{ex}(n-q) + h < 0 \tag{2.117}$$

which is equivalent to

$$J_{ex}(n+1) - J_{ex}(n) < 0 \tag{2.118}$$

Therefore, for $m > 0$, the difference of the proposed Lyapunov function is negative

$$\Delta J_{ex}(n) < 0 \quad \forall n \tag{2.119}$$

From the above discussion, it can be concluded that for $m > 0$, $J_{ex}(n)$ is a Lyapunov function. Since the existence of the Lyapunov function is a sufficient condition for stability, it can be stated that $m > 0$ is the sufficient condition for convergence. Based on Eq. (2.104), $m > 0$ requires that

$$2 - \mu_2 P_{x_f} \left(L + 2\Delta_{eq} \right) > 0 \tag{2.120}$$

The sufficient condition for FxLMS convergence is therefore

$$\mu_2 < \frac{2}{\left(L + 2\Delta_{eq} \right) P_{x_f}} \tag{2.121}$$

The convergence condition given by Eq. (2.121) is applicable to any arbitrary secondary path. To ensure the fastest convergence rate, the optimum FxLMS convergence condition is derived below. According to the Lyapunov stability theory, the difference of the Lyapunov function must be minimum. Based on Eq. (2.106), this difference function can be obtained as

$$\Delta J_{ex}(n) = -m \sum_{q=0}^{Q-1} w_{1T,q}^2 J_{ex}(n-q) + h \tag{2.122}$$

When the algorithm is far from being minimum MSE, $J_{ex}(n) \ll J_{\min}$, $\Delta J_{ex}(n)$ can be approximated as

$$\Delta J_{ex}(n) = -m \sum_{q=0}^{Q-1} w_{1T,q}^2 J_{ex}(n-q) \tag{2.123}$$

Since $J_{ex}(n)$ is a positive definite function and $m > 0$, to minimize $\Delta J_{ex}(n)$, m is maximized with respect to μ_2. Therefore,

$$\left[\frac{\partial m}{\partial \mu_2}\right]_{\mu_{2,opt}} = 0 \tag{2.124}$$

where $\mu_{2,opt}$ denotes the optimized step-size. By substituting Eq. (2.104) into Eq. (2.124), it can be shown that

$$P_{x_f}\sigma_s^{-2}\left[2-2\mu_{2,opt}P_{x_f}\left(L+2\Delta_{eq}\right)\right]=0 \tag{2.125}$$

Solving Eq. (2.125) to obtain the optimum step-size

$$\mu_{2,opt}=\frac{1}{P_{x_f}\left(L+2\Delta_{eq}\right)} \tag{2.126}$$

It is noted that the optimized step-size is about half of the convergence bound for μ_2 and that Eq. (2.126) is valid for any arbitrary moving average secondary path.

Initial guess for filter coefficient

Although the optimized adaptive step-size is available, however, it is still not sufficient to adjust the filter coefficient vectors, $\mathbf{W}_1$ and $\mathbf{W}_2$, to their optimized values. For a highly nonlinear model, there are numerous solutions. If the initial filter coefficient vectors are improperly set, they will never be adjusted to the optimized values. The initial guessed values for each filter $\mathbf{W}_1$ and $\mathbf{W}_2$ are derived in the present section.

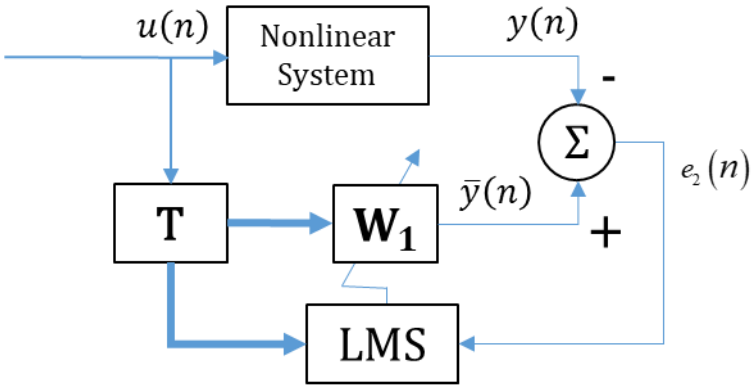

Figure 5 Schematic of a system identification algorithm.

As the system identification component of the control system seen in Figure 5, the wavelet transformed filter coefficient vectors $\mathbf{TW}_1$ represents the nonlinear system model. The difference between the output from the actual nonlinear system and the filter coefficient vectors is therefore

$$e_2(n) = y(n) - \mathbf{W}_1\mathbf{T}\mathbf{U}_2(n) \tag{2.127}$$

where

$$\mathbf{U}_2(n) = \left[u_2(n) \quad u_2(n-1) \quad \cdots \quad u_2(n-N+1)\right]^T \tag{2.128}$$

Noted that $u_2(n)$ here comes from the input signal directly since control is not yet engaged and initial guesses not yet provided. To solve $\mathbf{W}_1$ with N unknow values, it requires N equations. Since the wavelet transformed filter coefficient vectors represents the system, the equivalent conditions in Eq. (2.127) is sufficient for time

$(n-1)$ to $(n-N)$. Assume the wavelet transformed filter coefficient vectors $\mathbf{TW}_1$ fully represents the nonlinear system. Since

$$\mathbf{E}_2(n) = \mathbf{Y}(n) - \mathbf{W}_1\mathbf{T}\mathbf{X}_2(n) \tag{2.129}$$

where

$$\mathbf{E}_2(n) = \begin{bmatrix} e_2(n) & e_2(n-1) & \cdots & e_2(n-N+1) \end{bmatrix}^T \tag{2.130}$$

$$\mathbf{Y}(n) = \begin{bmatrix} y_2(n) & y_2(n-1) & \cdots & y_2(n-N+1) \end{bmatrix}^T \tag{2.131}$$

$$\mathbf{X}_2(n) = \begin{bmatrix} \mathbf{U}_2(n) & \mathbf{U}_2(n-1) & \cdots & \mathbf{U}_2(n-N+1) \end{bmatrix} \tag{2.132}$$

the difference between the output of the model system and the filter coefficient vectors should be zero, that is

$$0 = \mathbf{Y}(n) - \mathbf{W}_1\mathbf{T}\mathbf{X}_2(n) \tag{2.133}$$

By manipulating Eq. (2.133), the filter coefficient vectors $\mathbf{W}_1$ can be solved as follow

$$\mathbf{W}_1 = \mathbf{Y}(n)\mathbf{X}_2^{-1}(n)\mathbf{T}^{-1} \tag{2.134}$$

Then, Eq. (2.134) can be used as the initial guess for the filter coefficient vectors $\mathbf{W}_1$ in the system identification component. To properly control the input signal, the filter coefficient vectors $\mathbf{W}_2$ in the FxLMS algorithm is presented in Figure 6. Again the wavelet transformed filter coefficient vectors $\mathbf{TW}_1$ is assumed to fully represent the nonlinear system FxLMS.

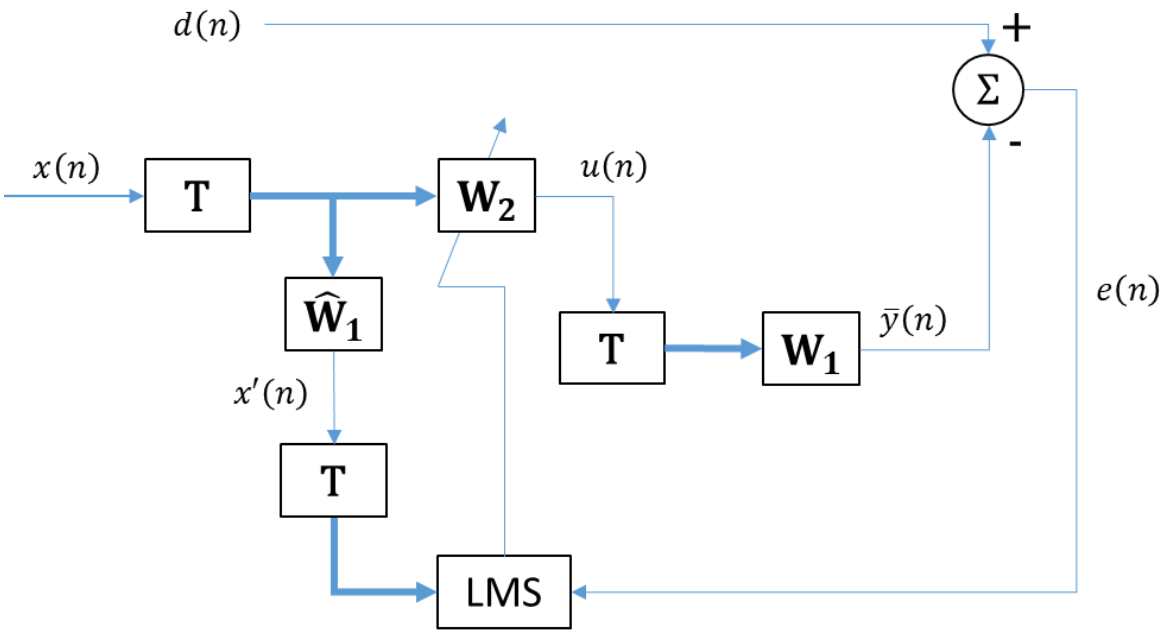

Figure 6 Schematic of a FxLMS algorithm with $\mathbf{TW}_1$ representing the nonlinear system.

The difference between the desired target $d(n)$ and the output $\bar{y}(n)$ is

$$e(n) = d(n) - \bar{y}(n) \tag{2.135}$$

When $\bar{y}(n)$ is perfectly controlled, $e(n)$ is zero. Then Eq. (2.135) can be rewritten as

$$d(n) = \bar{y}(n) \tag{2.136}$$

where

$$\bar{y}(n) = \mathbf{W}_1\mathbf{T}\mathbf{U}_2(n) \tag{2.137}$$

and

$$u_2(n) = \mathbf{W}_2\mathbf{T}\mathbf{X}(n) \tag{2.138}$$

By substituting Eq. (2.138) into Eq. (2.137), one has

$$\begin{aligned}\bar{y}(n) &= \mathbf{W}_1\mathbf{T}\left[\mathbf{W}_2\mathbf{T}\mathbf{X}(n) \quad \mathbf{W}_2\mathbf{T}\mathbf{X}(n-1) \quad \cdots \quad \mathbf{W}_2\mathbf{T}\mathbf{X}(n-N+1)\right] \\ &= \mathbf{W}_1\mathbf{T}\mathbf{W}_2\mathbf{T}\left[\mathbf{X}(n) \quad \mathbf{X}(n-1) \quad \cdots \quad \mathbf{X}(n-N+1)\right]\end{aligned} \tag{2.139}$$

To solve $\mathbf{W}_2$ with N unknown values, it requires N equations. Assume that Eq. (2.139) is valid in previous time steps, then Eq. (2.139) can be rewritten as

$$\begin{aligned}\bar{y}(n-1) &= \mathbf{W}_1\mathbf{T}\mathbf{W}_2\mathbf{T}\left[\mathbf{X}(n-1) \quad \mathbf{X}(n-2) \quad \cdots \quad \mathbf{X}(n-N)\right] \\ \bar{y}(n-2) &= \mathbf{W}_1\mathbf{T}\mathbf{W}_2\mathbf{T}\left[\mathbf{X}(n-2) \quad \mathbf{X}(n-3) \quad \cdots \quad \mathbf{X}(n-N-1)\right] \\ &\vdots \\ \bar{y}(n-N) &= \mathbf{W}_1\mathbf{T}\mathbf{W}_2\mathbf{T}\left[\mathbf{X}(n-N) \quad \mathbf{X}(n-N-1) \quad \cdots \quad \mathbf{X}(n-2N+1)\right]\end{aligned} \tag{2.140}$$

By solving Eq. (2.139) and Eq. (2.140), the initial guess for the filter coefficient vectors $\mathbf{W}_2$ is obtained.

CHAPTER III

GRAZING CONTROL OF A VIBRO-IMPACT OSCILLATOR*

Introduction

Impact oscillators are found in many applications. It is common for these applications to undergo the inadvertent state of grazing bifurcation. Vibro-impact incited grazing and route-to-chaos are difficult to control. The Newtonian model of a vibro-impact system rich of complex nonlinear behaviors is considered for the mitigation of impact induced instability and grazing. A novel concept developed in the previous chapter capable of simultaneous control of vibration amplitude in the time-domain and spectral response in the frequency-domain is applied to formulate a viable control solution. The developed controller explores wavelet adaptive filters and filtered-x least mean square algorithm to the successful moderation of the grazing and dynamic instability of the non-smooth system. The qualitative behavior of the controlled impact oscillator follows a definitive fractal topology before settling into a stable manifold. The controlled response is categorically quasi-periodic and of the prescribed vibration amplitude and frequency spectrum. [93]

*Reprinted with permission from "Mitigating Grazing Bifurcation and Vibro-Impact Instability in Time-Frequency Domain" by Chi-Wei Kuo, C. Steve Suh, 2016. Journal of Applied Nonlinear Dynamics, Volume 5(2), Pages 169-184, Copyright [2016] by L&H Scientific Publishing, LLC.

Vibro-Impact Oscillator Model

Grazing bifurcation induced by the collision of a periodic orbit with a switching manifold in a non-smooth system is potent in generating complex dynamics. The dynamic behavior in the immediate neighborhood of grazing experienced by an impact oscillator is inherently unstable [10]. The one degree-of-freedom vibro-impact model shown in Figure 7 [23] that describes the motion of the cart at low speed subject to a force of a sinusoidal profile is considered. The dynamic equation of the vibro-impact motion defined using the specified coordinate system is

$$M\ddot{x} + R\dot{x} + Kx = A\omega^2 \sin(\omega t) - k_{wall}(x-d)H[x-d] \tag{3.1}$$

where M is the mass of the moving cart, R is the damping coefficient, K is the stiffness of the spring, A is the excitation amplitude, and ω is the excitation frequency. The impact wall is located at $x = d$ and its stiffness is k_{wall} which is assumed to be much greater than K. The stiffness of the spring is dictated by a Heaviside function, $H[x-d]$. Eq. (3.1) can be further manipulated to be of the following dimensionless form [24]:

$$\ddot{y} = \alpha\,\omega^2 \sin(\omega\tau) - 2\xi\dot{y} - y - \beta(y-e)H[y-e] \tag{3.2}$$

where $y = x/x_0$ is the dimensionless displacement, $\dot{y} = \dot{x}/x_0$ is the dimensionless velocity, and $\ddot{y} = \ddot{x}/x_0$ is the dimensionless acceleration. The first term on the right hand side of Eq. (3.2) is the excitation force with $\alpha = A/x_0$ being the dimensionless excitation amplitude and $\tau = \omega_n t$ being the dimensionless time in which $\omega_n = \sqrt{K/M}$ defines the nature frequency. Also, $\xi = c/(2M\omega_n)$ is the damping ratio, $\beta = k_{wall}/K$ is the stiffness

ratio, and $e = d/x_0$ is the dimensionless gap. The arbitrary reference distance is defined at $x_0 = 1\,\text{mm}$.

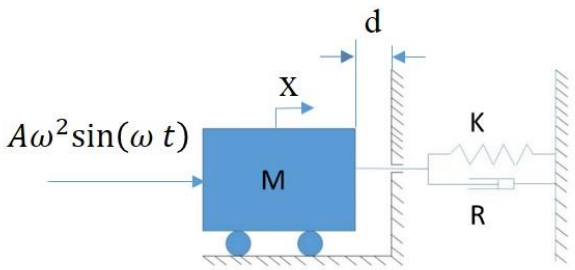

Figure 7 Vibro-impact model system [23].

Grazing Bifurcation of Vibro-Impact Oscillator

The time response of the vibro-impact model system corresponding to the parameters tabulated in Table 1 and subject to zero initial position and zero initial velocity is shown in Figure 8. It is noted that the system parameters are adopted from [95] and that the integration time step used is 0.001 sec.

Table 1 Dimensionless parameters of the vibro-impact model

Excitation Amplitude α	0.702
Excitation Frequency ω	0.8
Damping ξ	0.01
Stiffness Ratio β	29
Position of the wall e	1.26

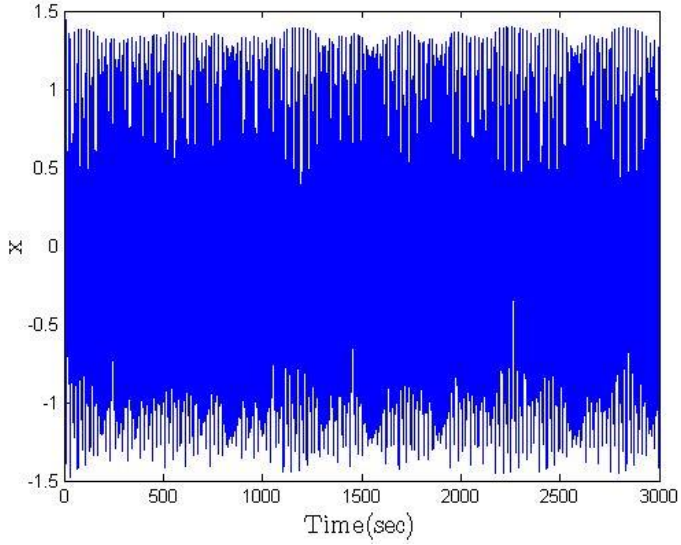

Figure 8 Time response of vibro-impact model system without controller.

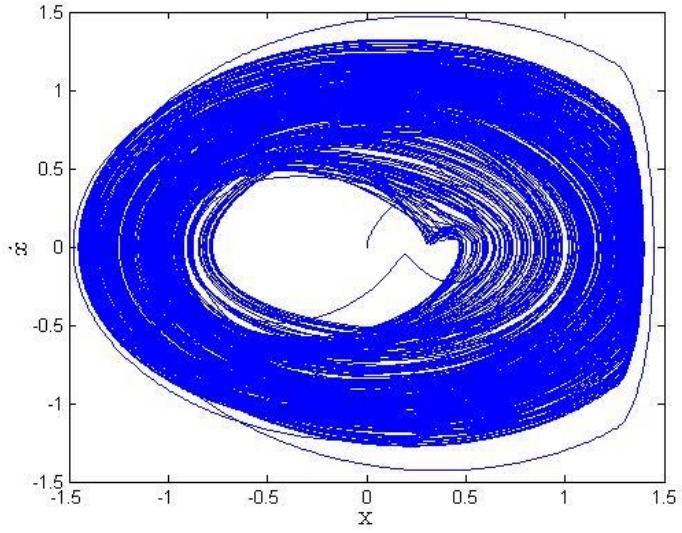

Figure 9 Phase portrait of uncontrolled response.

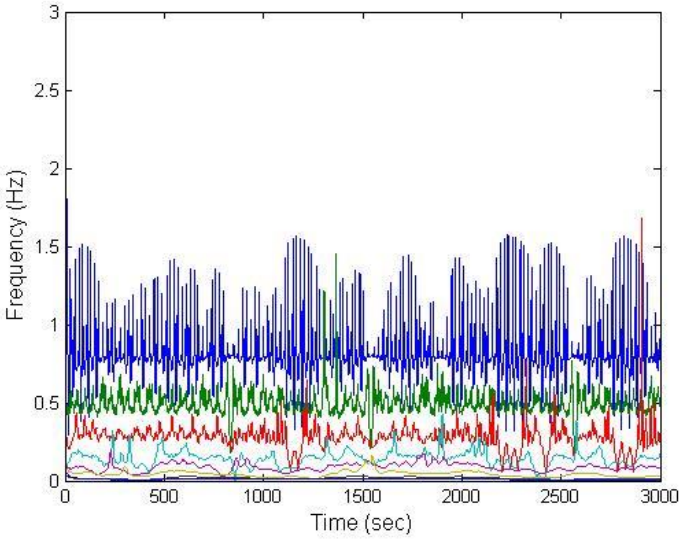

Figure 10 Instantaneous frequency of uncontrolled impact oscillator.

In the corresponding phase portrait shown in Figure 9, the trajectory on the right represents the discontinuous condition near where the wall is. The figure indicates an unstable motion recognized as grazing. The cluster of trajectories seen in the center of the figure registers the singularities fundamental to the vibro-impact dynamics of the oscillator. As seen in Figure 10 where the corresponding instantaneous frequency response is presented, the particular bifurcated state of instability is broadband and of a time-varying (non-stationary) spectrum. Together the 2 figures convey a state of instability that is bounded in the time-domain while simultaneously becoming unstably broadband in the frequency-domain due to the rapid switching of infinite numbers of unstable periodic orbits (UPOs) [81]. In order to effectively mitigate grazing bifurcation and prevent further dynamic deterioration, control needs to be performed in the time and

frequency domains concurrently. With the location and the stability of the corresponding equilibrium point varying in time, the impact oscillator is seen to undergo non-stationary route-to-chaos, which is one of the basic properties universal of all temporal nonlinear processes. The vibro-impact system is also highly sensitive to initial conditions. A minor deviation between two adjacent initial trajectories may diverge exponentially with the progression in time, thus implying that a small perturbation could render the system unstable. The figures necessarily indicate that the impact oscillator is difficult to control with linear control theory

Controlled Response

To mitigate the instability state of the broadband response shown in Figure 8, the nonlinear vibro-impact system is incorporated into the wavelet-based time-frequency control scheme given in Figure 4. The initial filter vectors for both the filters are $[0.01 \cdots 0.01]^T$ which is an $N \times 1$ matrix. Step sizes μ_1 and μ_2 for both the LMS filters are set to be 10^{-7}, and N, the data size, is arbitrarily selected as 2048. The desired target is a sinusoidal function $\alpha \sin\left(\omega_{ta} t\right)$ with the desired frequency $\omega_{ta} = 0.8$ and the corresponding desired amplitude $\alpha = 1$

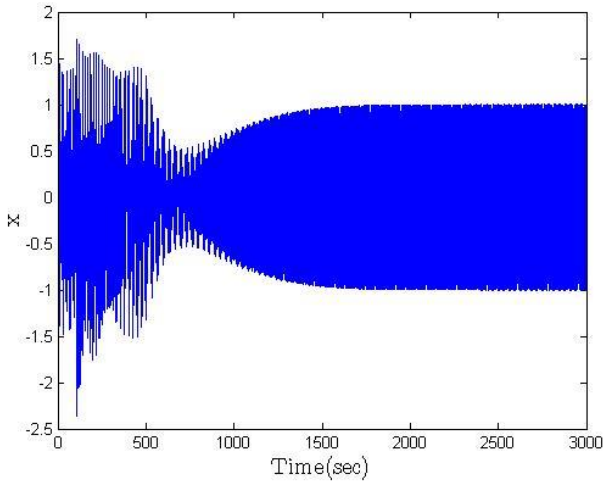

Figure 11 Time Response of controlled impact oscillator with a desired amplitude of 1.

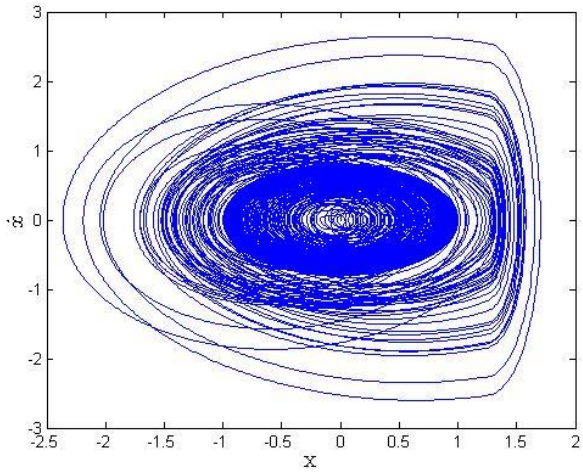

Figure 12 Phase portrait of controlled response with a desired amplitude of 1.

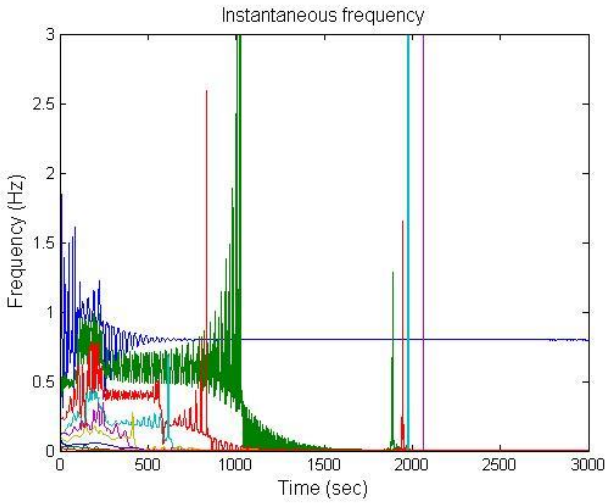

Figure 13 Instantaneous frequency of controlled response with a desired amplitude of 1.

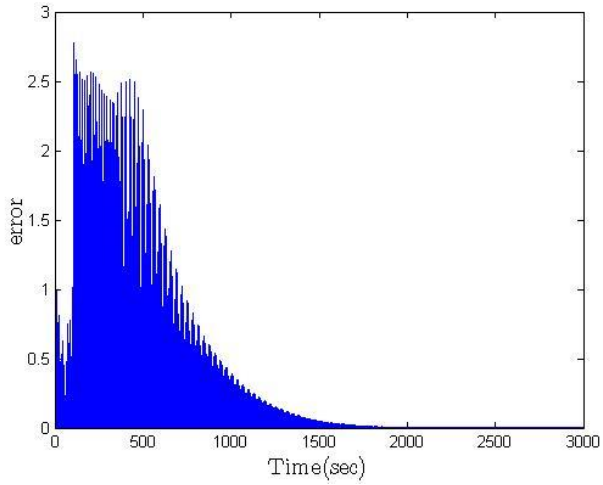

Figure 14 Error tracking of controlled response with a desired amplitude of 1.

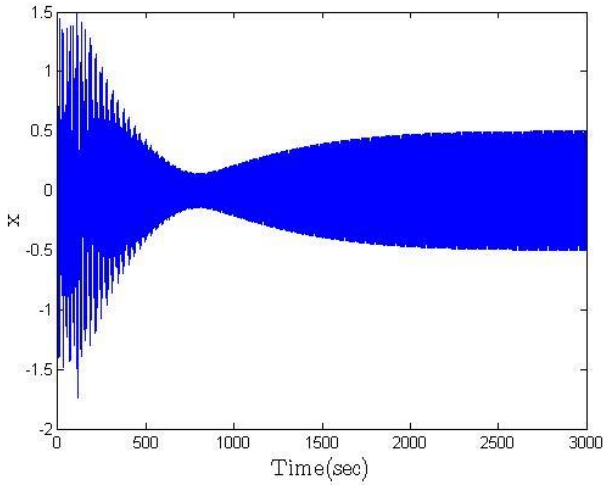

Figure 15 Time Response of controlled impact oscillator with a desired amplitude of 0.5.

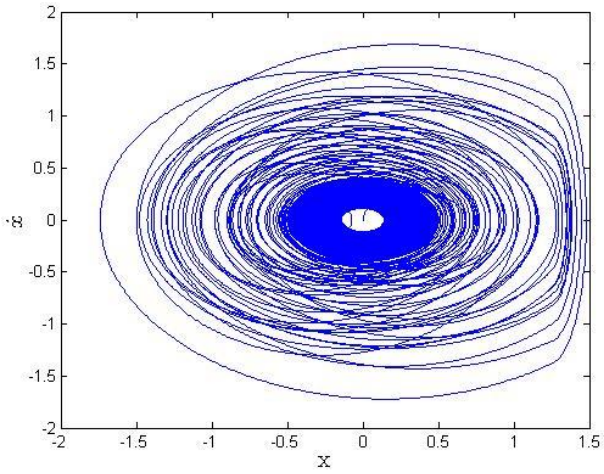

Figure 16 Phase portrait of controlled response with a desired amplitude of 0.5.

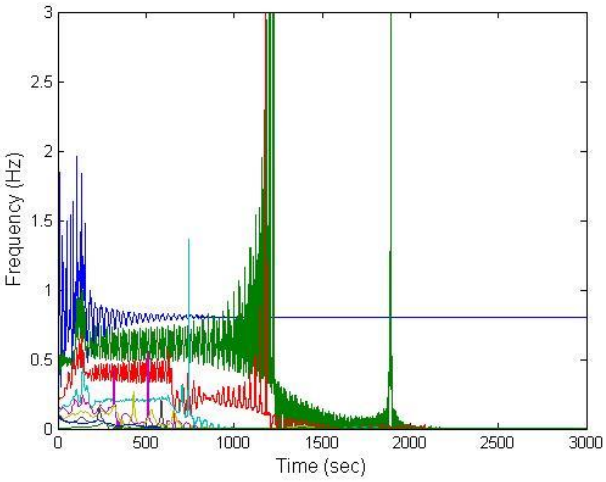

Figure 17 Instantaneous frequency of controlled response with a desired amplitude of 0.5.

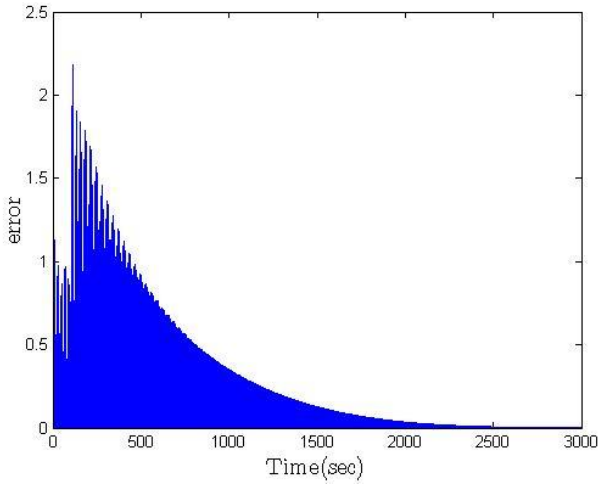

Figure 18 Error tracking of controlled response with a desired amplitude of 0.5.

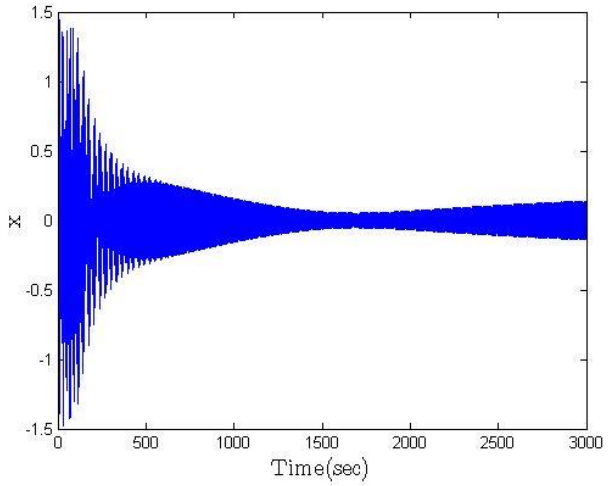

Figure 19 Time Response of controlled impact oscillator with a desired amplitude of 0.2.

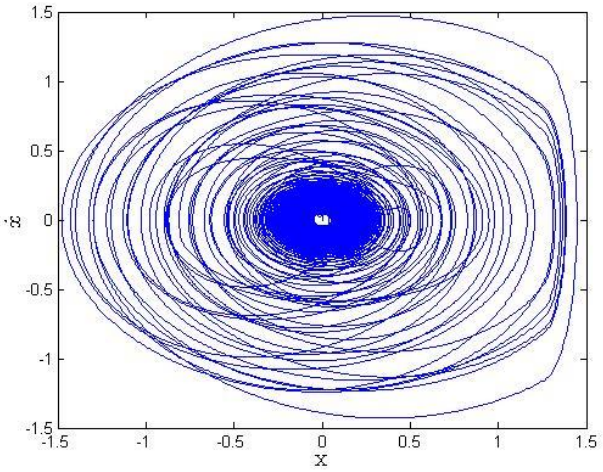

Figure 20 Phase portrait of controlled response with a desired amplitude of 0.2.

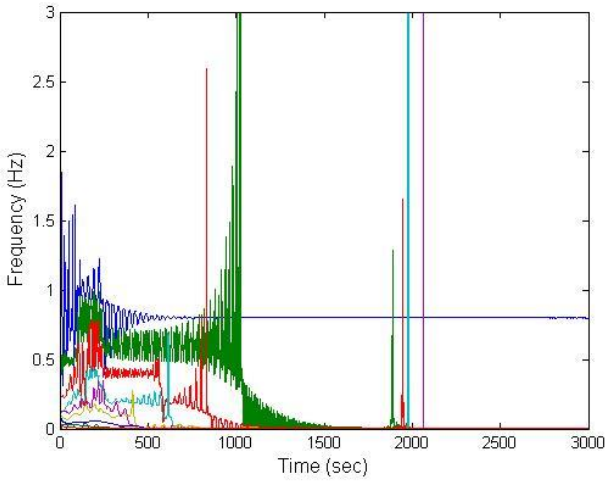

Figure 21 Instantaneous frequency of controlled response with a desired amplitude of 0.2.

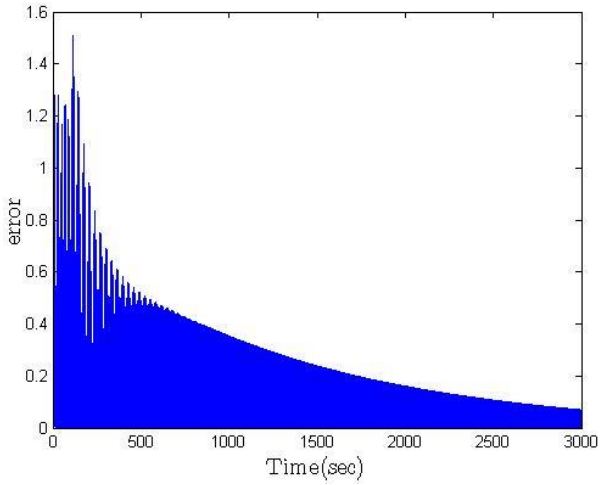

Figure 22 Error tracking of controlled response with a desired amplitude of 0.2.

The time response in Figure 11 shows that the response becomes steady after the controller is brought online at t = 100 sec. The corresponding phase portrait in Figure 12

indicates a limit-cycle bounded between +1 and -1, thus signifying that the oscillator is now in a state of stable motion. In addition, given the finite number of time-invariant frequency components, the corresponding instantaneous frequency in Figure 13 shows that the system response after the controller is brought online is quasi-periodic. The resulted state of stability of the discontinuous system is further ascertained by the rapid diminishing absolute error plotted in Figure 14 in which the time response is seen to rapidly converge to the desired target response.

There are scenarios in which vibration amplitude needs be kept within a tight range of tolerance to ensure collision-free motions. In the followings the desired amplitude is further reduced to 0.5 and 0.2 to facilitate much greater safety margin using the nonlinear controller. The step sizes μ_1 and μ_2 for the two adaptive filters are kept the same as the previous case. Results shown in Figure 15-Figure 18 are, respectively, the time response, phase portrait, instantaneous frequency response, and error that correspond to the case of 0.5 target amplitude. It is evident that all the controlled responses in the time-domain are of the desired amplitude. The controlled frequency response is both bounded and periodic. The time response, phase portrait, instantaneous frequency response, and error that correspond to the case of a much tighter target amplitude, being set at 0.2, are given in Figure 19-Figure 22. Unlike Figure 16 and Figure 18, the error seen in Figure 22 is a transient state that eventually settles into a steady state of zero magnitude, at which point the impact oscillator follows the desired target with the prescribed frequency response.

Poincaré sections are employed in the followings to further demonstrate the performance of the controller design. Figure 23 is the corresponding Poincaré section of the uncontrolled vibro-impact system responses shown in Figure 8 and Figure 9. No fractal patterns of any discernible scale can be identified in the figure. In conjunction with Figure 10 where the instantaneous frequency response is seen to be broadband and time-varying (non-stationary), it is evident that the motion state of the uncontrolled system is chaotic. Figure 24, Figure 26, and Figure 28 are the Poincaré sections associated with the 3 desired targets before the controller is activated. There are no identifiable patterns or structures as expected. After the controller is applied, as is readily evident from Figure 25, Figure 27, and Figure 29, as $\mathbf{t} \to \infty$ all the 3 cases of response converge to a stable manifold with a readily discernible, definitive topology. The well-defined fractal structures signify that the grazing state is effectively mitigated, and instability is superseded by a stable state of motion characterized by a limit-cycle. As is indicated by the instantaneous frequency responses in Figure 13, Figure 17, and Figure 21, the controlled motions of the impact oscillator are all quasi-periodic responses of finite, time-invariant frequency components. The motion of the harmonically excited vibro-impact system under the jurisdiction of the nonlinear time-frequency controller has become stationary, bounded, and predictable, wholly complying with the prescribed target response that is of the specific, desired temporal and spectral properties.

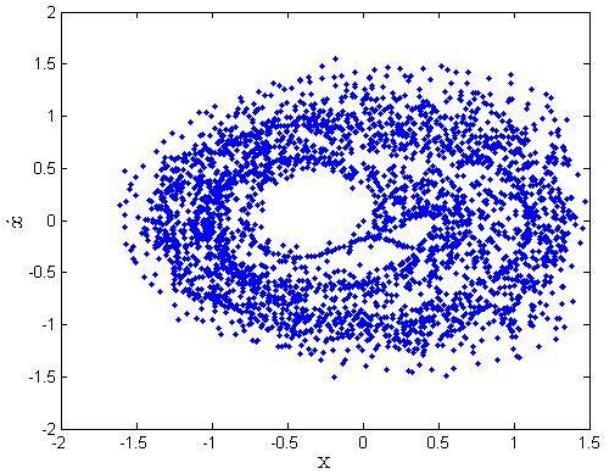

Figure 23 Poincare section of uncontrolled system response.

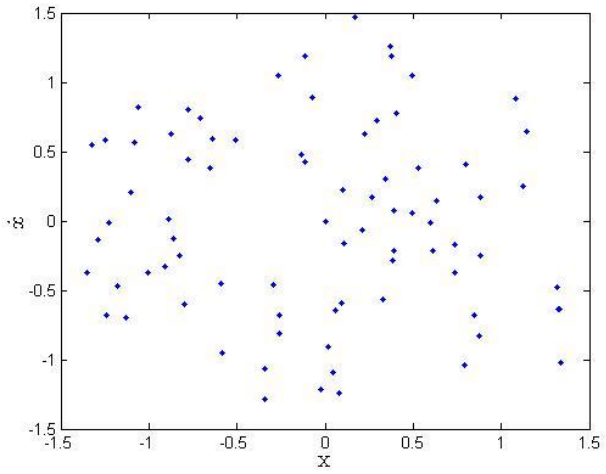

Figure 24 Poincare section of controlled system response with a desired amplitude of 1 (before controller is brought online).

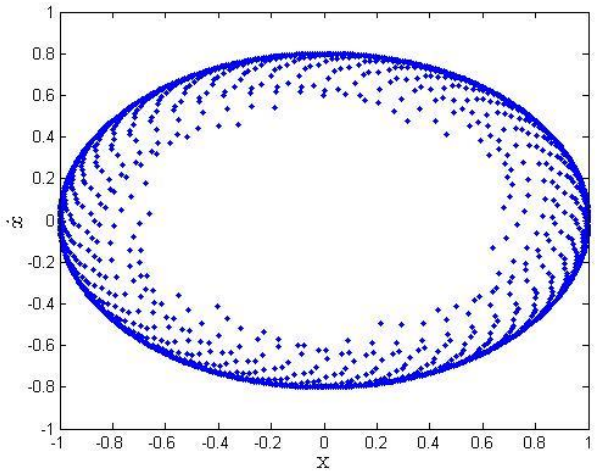

Figure 25 Poincare section of controlled system response with a desired amplitude of 1 (after controller is brought online).

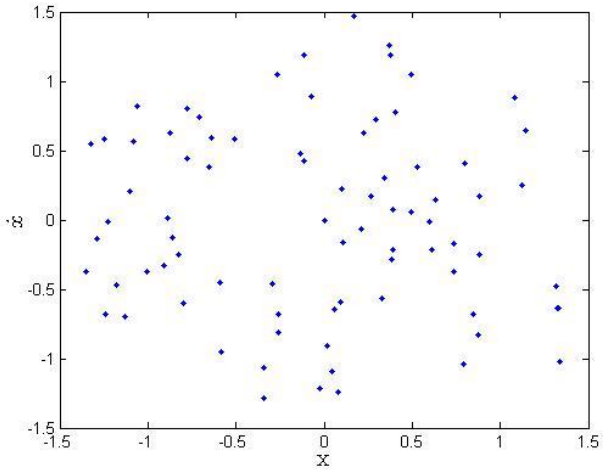

Figure 26 Poincare section of controlled system response with a desired amplitude of 0.5 (before controller is brought online).

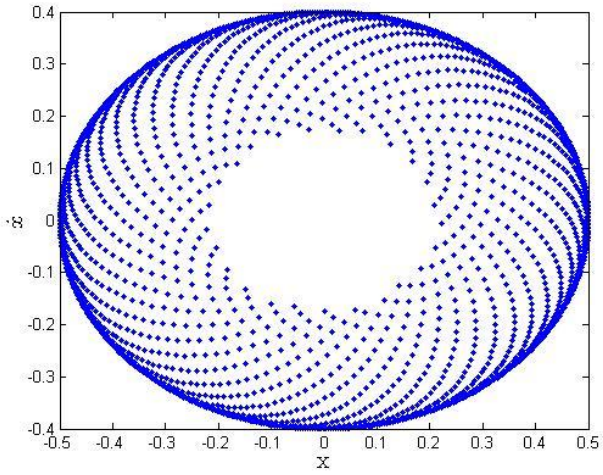

Figure 27 Poincare section of controlled system response with a desired amplitude of 0.5 (after controller is brought online).

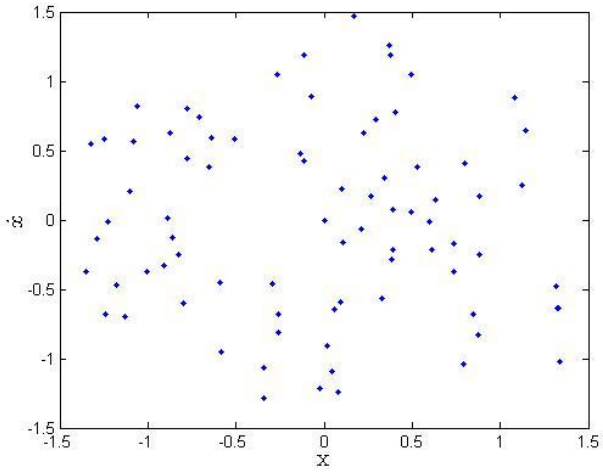

Figure 28 Poincare section of controlled system response with a desired amplitude of 0.2 (before controller is brought online).

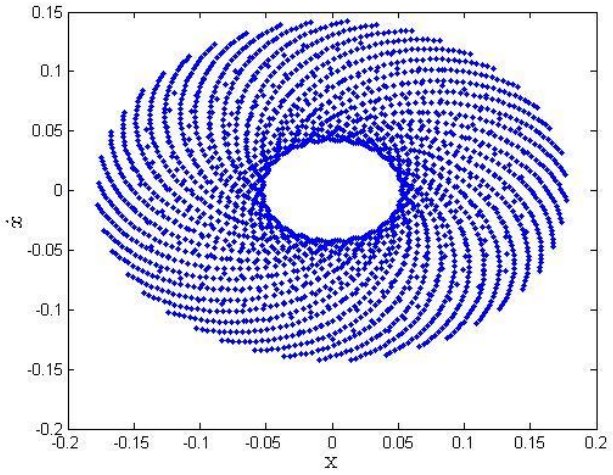

Figure 29 Poincare section of controlled system with a desired amplitude of 0.2 (after controller is brought online).

Summary

Vibro-impact systems are prone to dynamic instability. Non-smooth behaviors inherent of such systems such as grazing are detrimental because they impart strong nonlinearity to the systems' time responses and cede to frequency responses that are non-stationary and broadband. These imply that both the time and frequency responses need be considered if discontinuity and instability are to be effectively negated. The developed wavelet-based time-frequency controller with parallel on-line modeling was shown to control and stabilize the dynamic response of the impact oscillator to follow a desired harmonic target of a specified amplitude. Instantaneous frequency along with Poincare sections were employed to show the motion state of the oscillator in the time-frequency domain before and after the controller was applied. The controller demonstrated the ability to reduce the vibration amplitude of the system, which is

important for preventing the system from impacting the boundary. In addition, the controller design was shown to be effective in resolving grazing behaviors and also in rendering dynamic stability that is qualitatively a limit-cycle. The controlled motions of the vibro-impact system were all unconditionally stationary, quasi-periodically stable, and of the time and frequency characteristics dictated by the prescribed target response, thus demonstrating the feasibility of the simultaneous time-frequency controller design in stabilizing the discontinuous vibro-impact system.

CHAPTER IV

CONTROL OF A NON-AUTONOMOUS TIME-DELAYED SYSTEM WITH CUBIC ORDER FEEDBACK*

Introduction

Time-delayed feedback of a small magnitude can perturb a nonlinear dynamic system to exhibit complex dynamical responses including route-to-chaos. Such motions are harmful as they negatively impact the stability and thus output quality. The performance, quality, and capacity can be improved enormously with a viable control solution. The novel nonlinear time-frequency control theory formulated in Chapter II is explored to formulate a control methodology feasible for the mitigation of a non-autonomous time-delayed oscillator having several higher order nonlinear feedback. Featuring wavelet adaptive filters for simultaneous time-frequency resolution and filtered-x least mean square algorithm for system identification, the controller design is shown to successfully moderate the dynamic instability of the time-delayed feedback system with various time-delay parameters ranging from 0.22 sec to 0.3 sec. The validity of the controller design is demonstrated by evaluating its performance against PID and Fuzzy logic in controlling displacement and frequency responses with the most chaotic dynamic response time-delay parameter. [94]

---

*Reprinted with permission from "A case of mitigating non-autonomous time-delayed system with cubic order feedback" by Chi-Wei Kuo, C. Steve Suh, 2017. Journal of the Franklin Institute, Volume 354, Pages 6651-6671, Copyright [2017] by Elsevier Ltd.

Non-Autonomous Time-Delayed Feedback Oscillator Model

Consider the non-autonomous time-delayed feedback oscillator with high-order external forcing terms below

$$\ddot{x}+\omega_0^2 x-\alpha_1\dot{x}+\alpha_2\dot{x}^3=k\cos\left(\omega_f t\right)+\beta_1\left[\dot{x}\left(t-t_d\right)-\dot{x}\left(t\right)\right]+\beta_2\left[\dot{x}\left(t-t_d\right)-\dot{x}\left(t\right)\right]^3 \quad (4.1)$$

The oscillator which is subjected to time-delays and nonlinear feedback gains was found to display rich dynamics including double Hopf bifurcation and chaotic response [47]. In the following sections the innate dynamics of the oscillator is explored first to study the sensitivity of the system's response to slightly different time-delay inputs. All the system parameters in Eq. (4.1) are assumed to be positive with the following values: $a_1=12.2$, $a_2=0.3$, $\beta_1=6.5$, $\beta_2=1$, and $k=12$. The external driving frequency is set at $\omega_f=2$ rad/s and the characteristic frequency of the oscillator is $\omega_0=10$ rad/s. A dynamic model of the time-delayed feedback oscillator is built in MATLAB/Simulink and numerically time-integrated using a fourth-order Runge–Kutta algorithm. The initial velocity and displacement are both zeros. An integration time step of 10^{-6} sec is used for all the three cases investigated in the present section

Nonlinearity of Time-Delayed Feedback Oscillator

The time-delay parameter set for the first case is $t_d=0.22$ sec. The corresponding time response of the oscillator shown in Figure 30(a), though bounded, is a state of dynamic instability. As will be made explicit later, the t_d being considered renders a bifurcated route-to-chaos behavior that is also of broad spectral bandwidth.

The associated phase portrait in Figure 30(b) conveys a better picture of the time-delayed feedback system. The cluster of trajectories seen in the center of the figure registers the singularities fundamental to the time-delayed feedback dynamics of the oscillator. Together the two figures indicate that the response is bounded in the time-domain while simultaneously becoming unstably broadband in the frequency-domain due to the rapid switching of the infinite number of unstable periodic orbits (UPOs). It is infeasible to mitigate such a state of instability with linear control theory because of the higher-order feedback term in the equation of motion. When the time-delay parameter t_d is set to be 0.27 sec, the system displays the most prominent nonlinear behavior of all the cases considered. Figure 31(a) and Figure 31(b) show a chaotic state of response with many different frequencies and evidences of discontinuity. Figure 32 presents the responses of the last case in which $t_d = 0.3$ sec. Although the time response seems to convey a false sense of bounded, stable state of motion, however, not unlike Figure 31(b), the phase portrait in Figure 32(b) suggests multiple UPOs. The UPOs in the phase portraits that correspond to the 3 different time-delay parameters indicate the level of difficulty in regulating the system with contemporary control approach. To address the nonlinearity due to the time-delay feedback gain dictated by the higher order feedback terms in Eq. (4.1), a nonlinear control methodology is required to ensure stability.

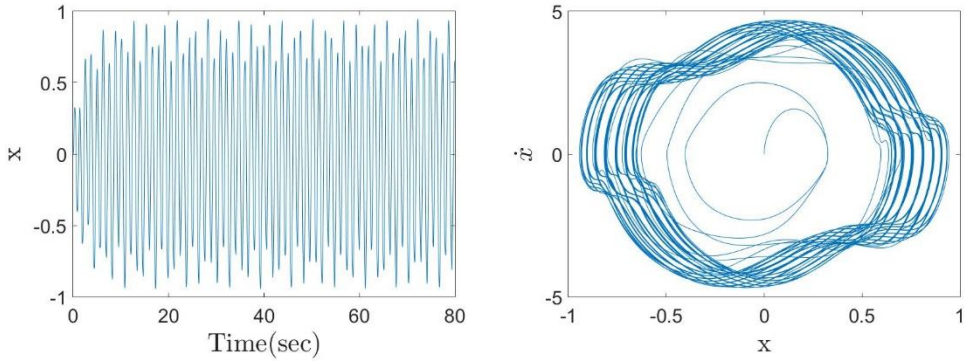

(a) **(b)**

Figure 30 (a) Time response and (b) phase portrait of the time-delayed feedback oscillator with time-delay t_d = 0.22 sec.

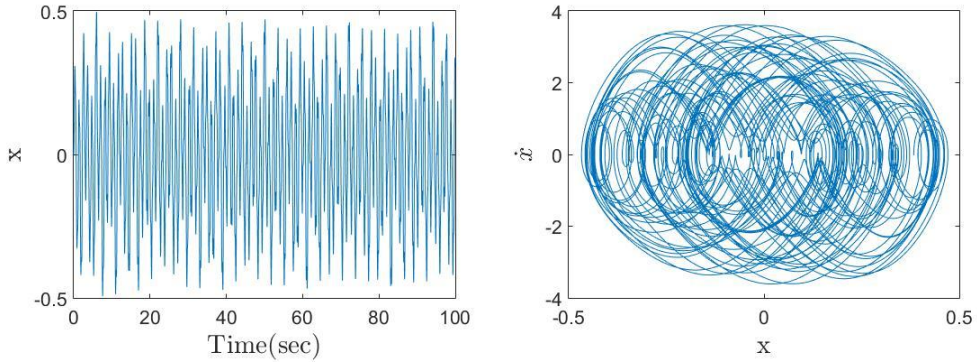

(a) **(b)**

Figure 31 (a) Time response and (b) phase portrait of the time-delayed feedback system with time-delay t_d = 0.27 sec.

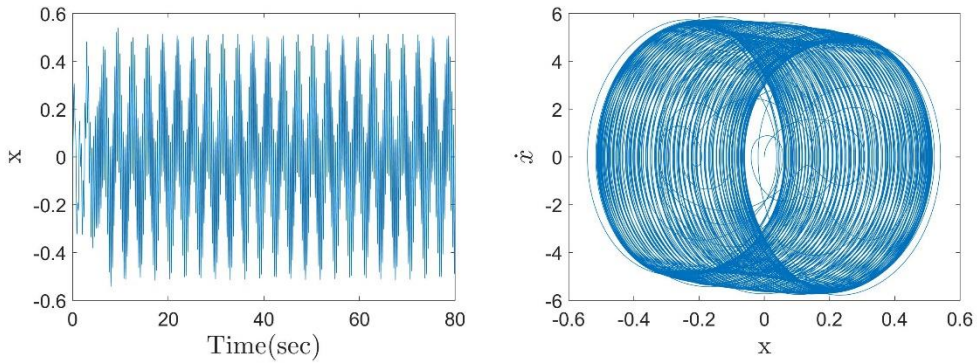

(a) **(b)**

Figure 32 (a) Time response and (b) phase portrait of the time-delayed feedback system with time-delay t_d = 0.3 sec.

Controlled Response

In the present section the wavelet-based time-frequency control concept is explored and evaluated to establish its feasibility in mitigating the complex states of dynamic instability of the time-delayed feedback oscillator whose nonlinear motions were seen in Figure 30-Figure 32. The nonlinear system is incorporated into the control scheme given in Figure 6 and identical integration time step and time-delay are used to maintain consistency. The $N \times 1$ initial filter vectors for both the filters are $\begin{bmatrix} 0.0045 & \cdots & 0.0045 \end{bmatrix}^T$ where the data collection size N is discretionarily selected as 256. The optimization step sizes, μ_1 and μ_2, of both the LMS filters are 10^{-16}. The desired target is a sinusoidal function, $\alpha \cos(\omega_{ta} t)$, where the target frequency is $\omega_{ta} = 2$ rad/s and the amplitude is $\alpha = 0.4$. The time response in Figure 33(a) corresponds to the case in which $t_d = 0.22$ sec. Once the system response reaches steady-state the

controller is brought online at $t = 30$ sec. The difference between the controlled response and the desired target in Figure 33(b) is satisfactory. In contrast with Figure 30(b) where the spectral response was broad in bandwidth, the phase portrait in Figure 30(c) indicates that the oscillator is now in a quasi-periodic state of stable motion moving in a limit-cycle bounded between -0.9 and $+0.9$. The corresponding instantaneous frequency in Figure 33(d) also attests to the same observation by showing that the system response is a bandwidth-limited temporal-modal structure [78] indicative of dynamic instability and route-to-chaos. After the controller is applied, the response stabilizes into a stable manifold of a definitive topology characteristically different from Figure 30(d) in which a discontinuous motion is indicated.

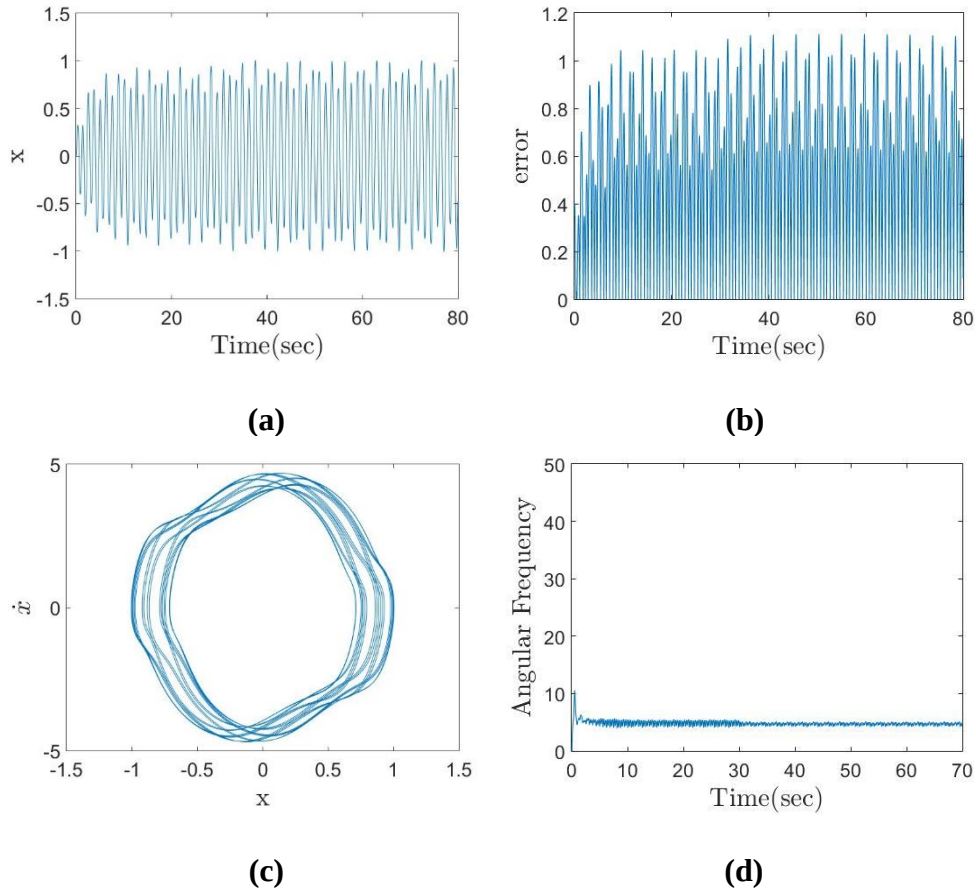

Figure 33 (a) Time response, (b) Error response, (c) Phase portrait, and (d) Instantaneous frequency of the time-delayed feedback oscillator with controller initiated at time t = 30 sec and time-delay t_d = 0.22 sec.

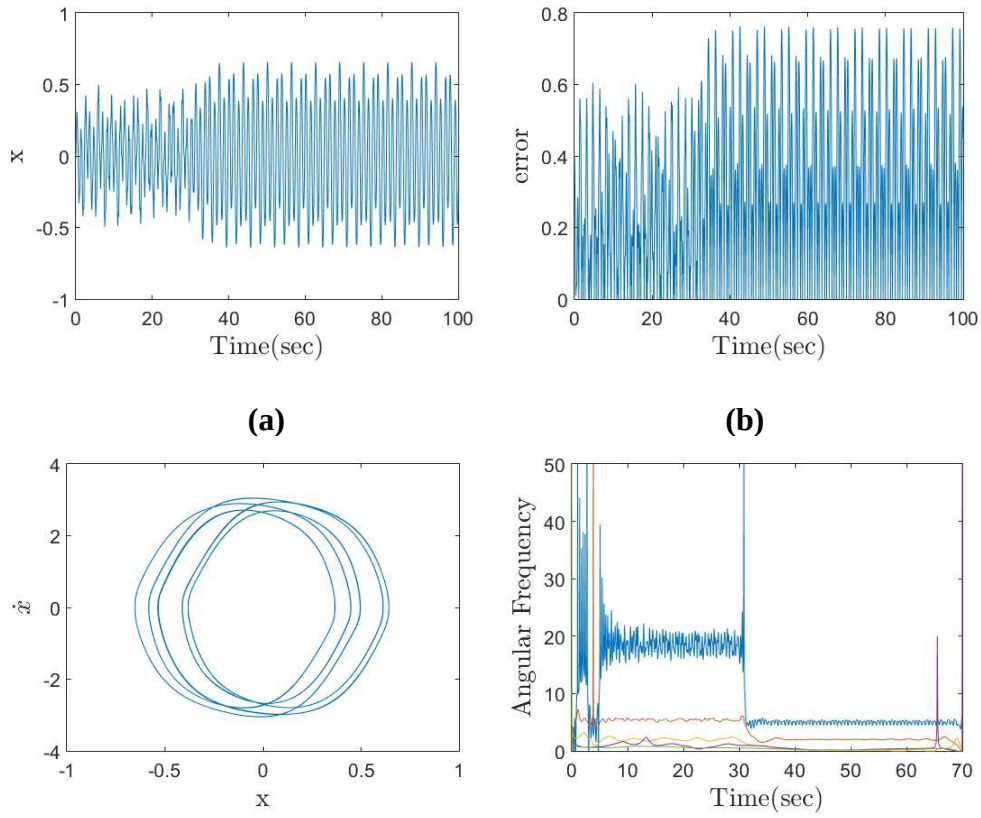

Figure 34 (a) Time response, (b) Error response, (c) Phase portrait, and (d) Instantaneous frequency of the time-delay feedback system with controller initiated at time t = 30 sec and time-delay t_d = 0.27 sec.

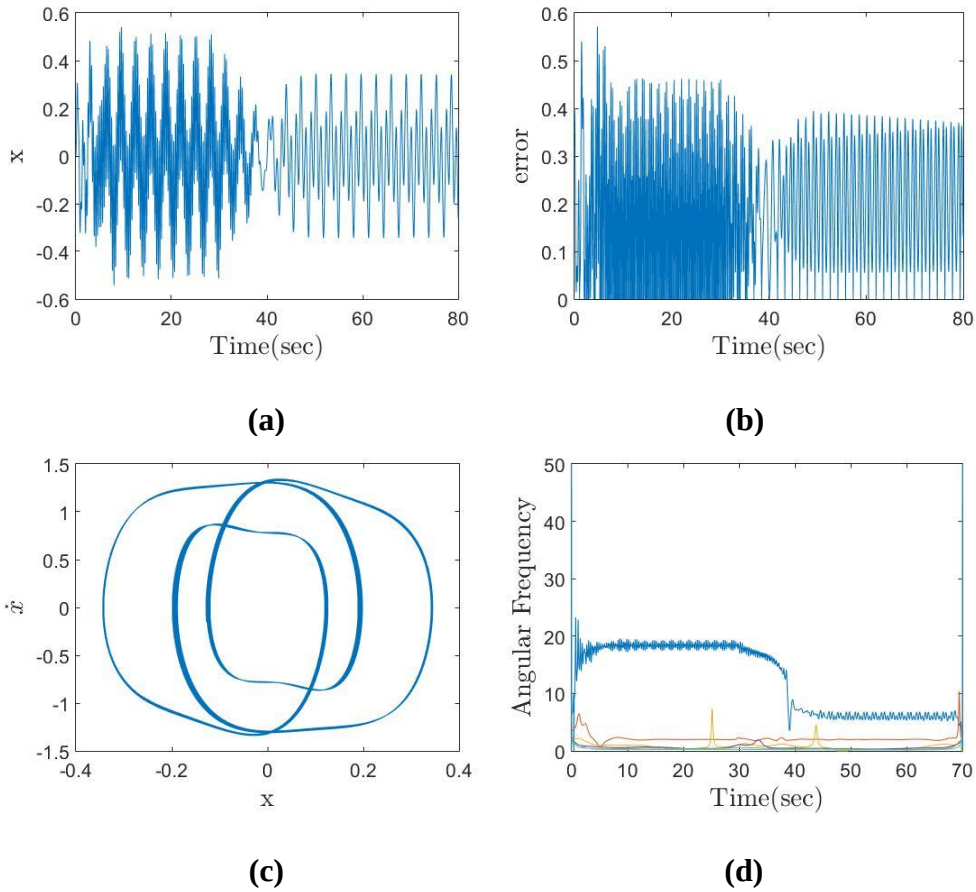

Figure 35 (a) Time response, (b) Error response, (c) Phase portrait, and (d) Instantaneous frequency of the time-delay feedback oscillator with controller initiated at time t = 30 sec and time-delay t_d = 0.3 sec.

The time-delayed feedback oscillator displayed the most prominent nonlinear behaviors of all the cases considered with $t_d = 0.27$. Following the same desired target the chaotic oscillator is seen in Figure 34(a) to respond in no time to the exertion of the controller initiated at time t = 30sec. The associated phase portrait in Figure 34(c) indicates a stable motion of quasi-periodic type. The corresponding instantaneous frequency for the controlled response in Figure 34(d) shows that as soon as the controller

is engaged the broad bandwidth chaotic motion is negated and the oscillator is stabilized into following a time-invariant spectrum of a finite number of frequencies. This is also supported by Figure 34(b) in which the difference between the desired target and the controlled output in Figure 34(b) is periodic, thus stationary.

The controller demonstrates similar performance for the case with time-delay $t_d = 0.3$. After turning on the controller at time t = 30 sec to track the desired target with the frequency $\omega_{ta} = 2$ and amplitude $\alpha = 0.4$, the time response in Figure 35(a) is effectively mitigated. The phase portrait in Figure 35(c) indicates the controlled response is a limit-cycle type of motion whose spectral response in Figure 35(d) is characteristically similar to Figure 35(d). That is, the driving frequency of the oscillator at $\omega_f = 2$ is properly tracked despite of the omnipresent linear and cubic order feedback gains. The manifold of many UPOs in Figure 32(b) signifying the state of dynamic instability is reduced to a stable state of quasi-periodic motion characterized by 4 definitive temporal-modal structures. Figure 33-Figure 35 show that the motions of the harmonically excited non-autonomous time-delayed feedback oscillator under the jurisdiction of the nonlinear time-frequency controller are without exception stationary, bounded, and predictable, complying with the prescribed target response having specific temporal and spectral properties.

The nonlinear time-frequency control concept is evaluated in this section against 2 types of common controller designs, namely, PID and fuzzy logic control (FLC), for performance in mitigating the time-delayed feedback induced instabilities seen in Figure 30-Figure 32. The PID scheme employed for tracking the output displacement of the

time-delayed oscillator in Eq. (4.1) is illustrated in Figure 36. The PID controller is designed based on the following,

$$u(n) = k_p e(n) + k_i \left[u(n-1) + \frac{e(n) + e(n-1)}{2} dt \right] + k_d \frac{e(n) - e(n-1)}{dt} \tag{4.2}$$

where $u(n)$ is the output from the controller, dt is the integration time step, $e(n)$ is the error between the desired signal and the actual output from the system. Control parameters k_p, k_i, and k_d are proportional gain, integral gain, and derivative gain, respectively. The optimal gain values selected for the PID controller are $k_p = 1110.26$, $k_i = 0$, and $k_d = 0$.

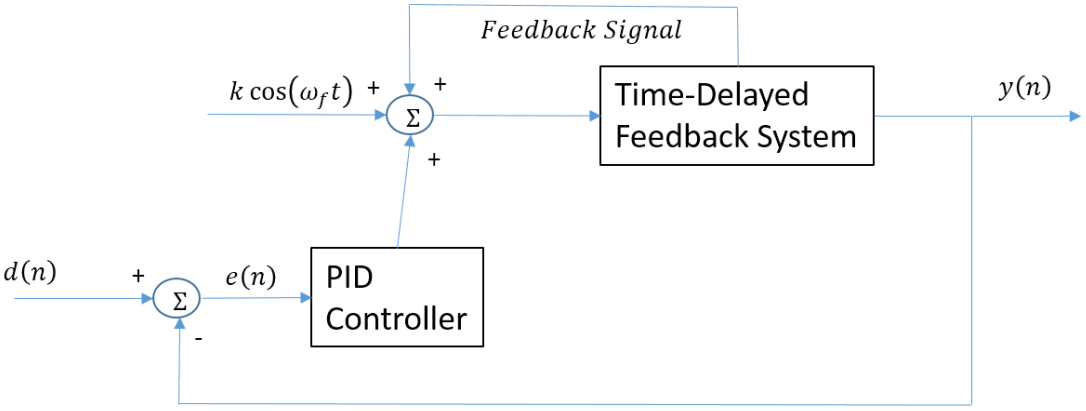

Figure 36 PID controller for displacement tracking of time-delayed feedback system.

The FLC scheme employed for the output signal tracking of the time-delayed system is illustrated in Figure 37 where $e(n)$ is the error between the desired target, $d(n)$, and the actual output signal, $y(n)$.

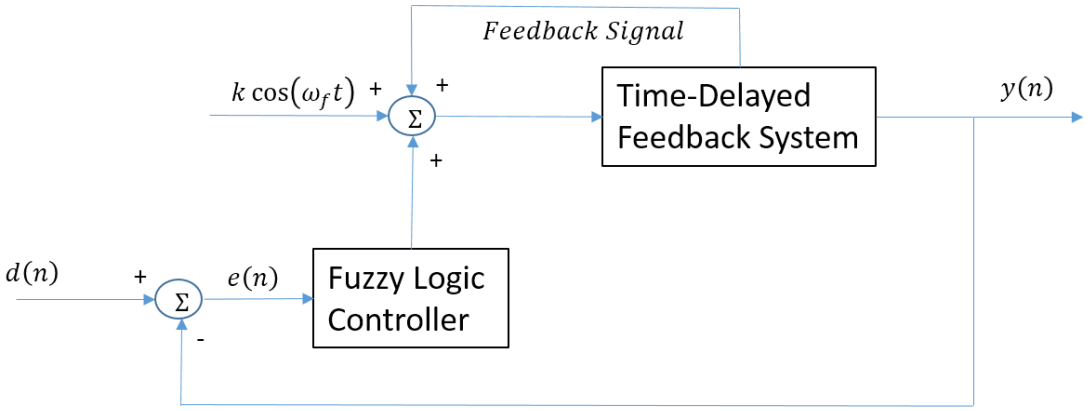

Figure 37 FLC for displacement tracking of time-delayed feedback system.

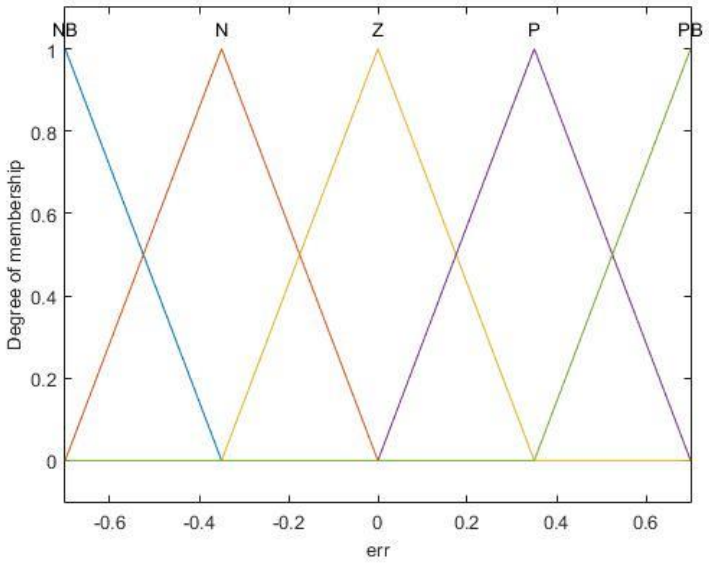

Figure 38 Input membership function.

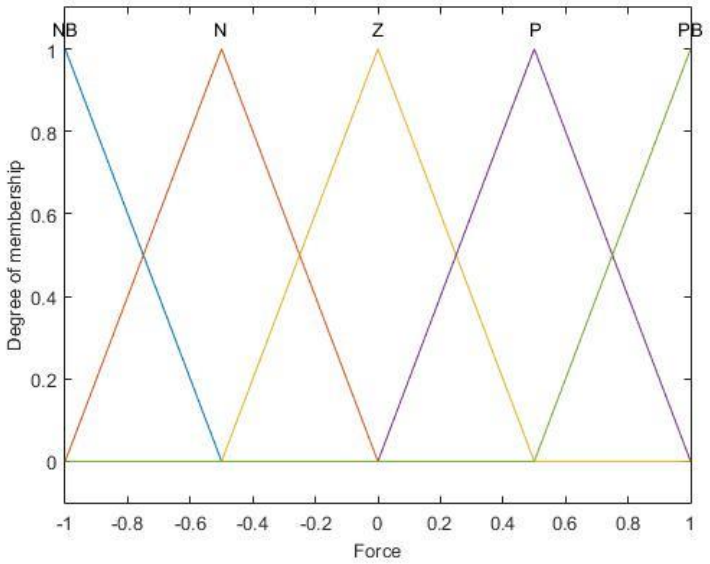

Figure 39 Output membership function.

Table 2 Fuzzy Rules

Rule	Description
1	If (err is NB) then (Force is NB)
2	If (err is N) then (Force is N)
3	If (err is Z) then (Force is Z)
4	If (err is P) then (Force is P)
5	If (err is PB) then (Force is PB)

$e(n)$ is selected as the input to the fuzzy logic controller. The corresponding membership functions and fuzzy rules are indicated in Figure 38 and Figure 39 and Table 1, where NL, NB, N, Z, P, PB, and PL stand for negative large, negative big, negativity, zero, positive, positive big, and positive large, respectively.

Although increasing the number of fuzzy rules can potentially improve performance, the fuzzy logic controller is deliberately designed to be simple out of the following considerations. The first is that the controlled output from the fuzzy logic controller relies extremely on the input. The second is that the feedback signal of the time-delayed system can be considered as the noise that distorts the information pertaining to the true dynamic state of the system. The particular effect becomes more prominent when the system reaches steady-state and induces severe chattering in the output signal [96]. The fuzzy rules presented in Table 2 are the result of considering the above which is also tested to be sufficient for demonstration purpose.

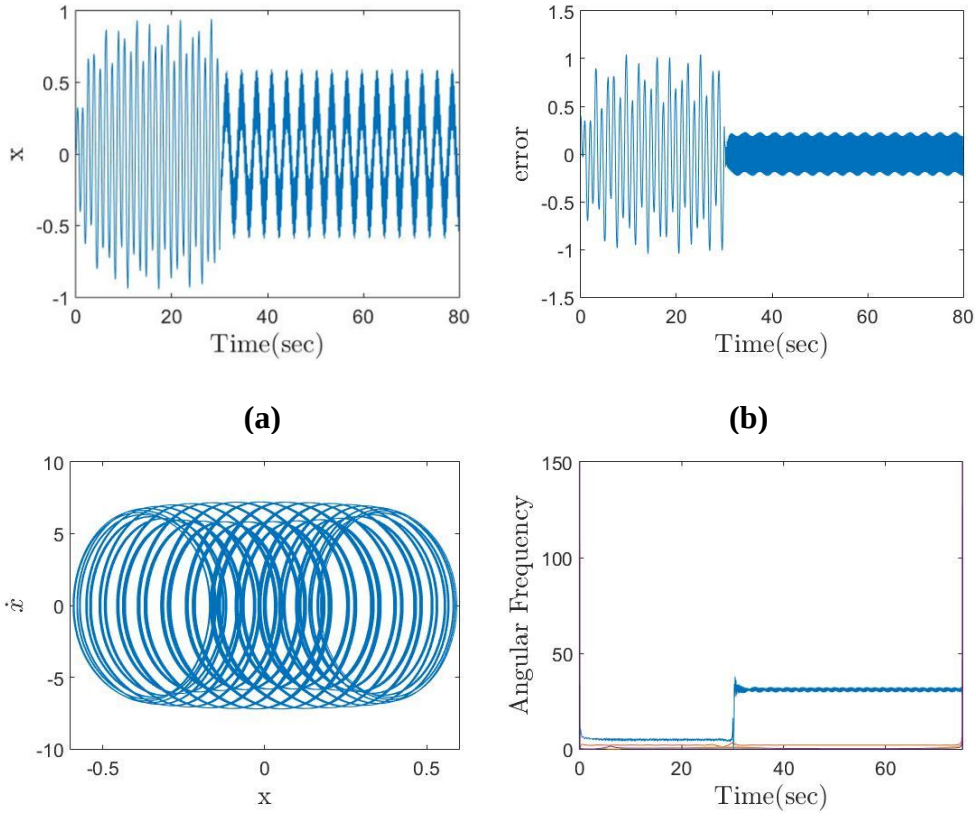

Figure 40 (a) Time response, (b) Error response, (c) Phase portrait, and (d) Instantaneous frequency of the time-delayed feedback system with PID controller initiated at time t = 30 sec and time-delay t_d = 0.22 sec.

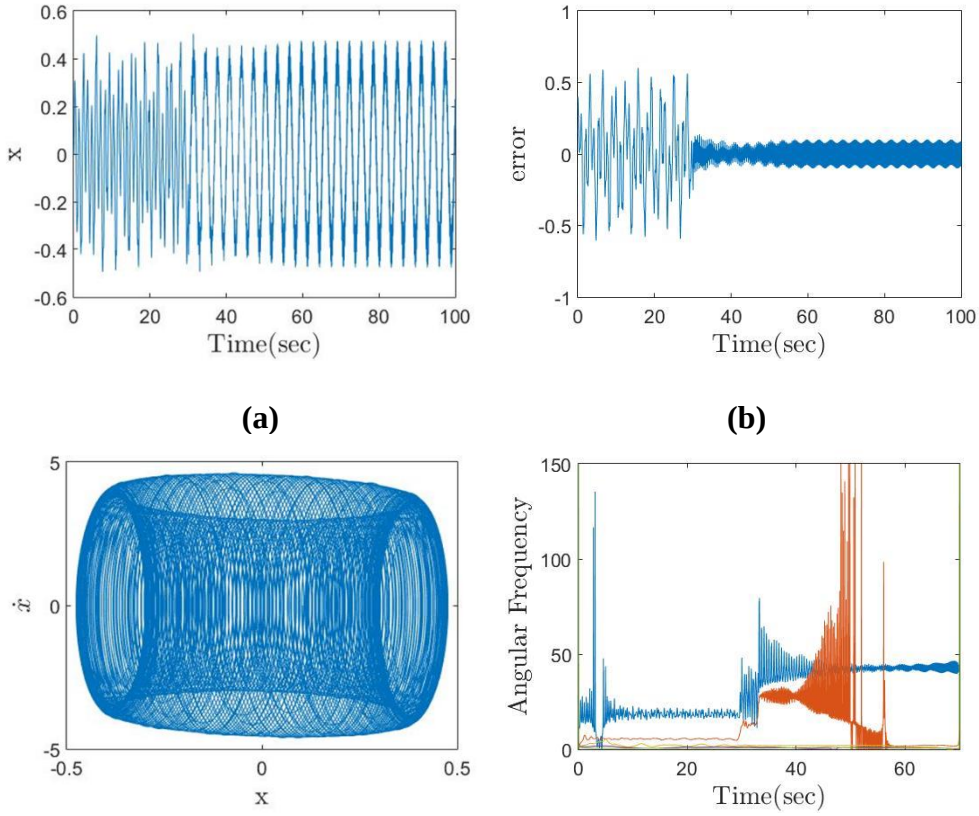

Figure 41 (a) Time response, (b) Error response, (c) Phase portrait, and (d) Instantaneous frequency of the time-delayed feedback system with PID controller initiated at time t = 30 sec and time-delay t_d = 0.27 sec.

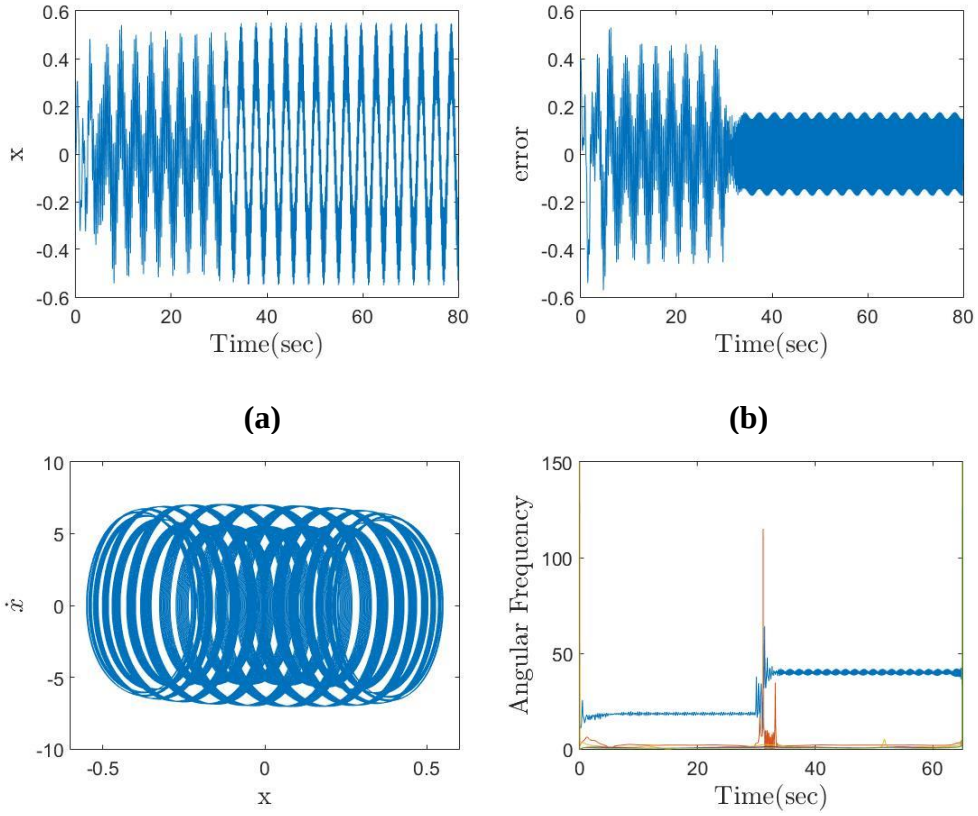

Figure 42 Time response, (b) Error response, (c) Phase portrait, and (d) Instantaneous frequency of the time-delay feedback system with PID controller initiated at time t = 30 sec and time-delay t_d = 0.3 sec.

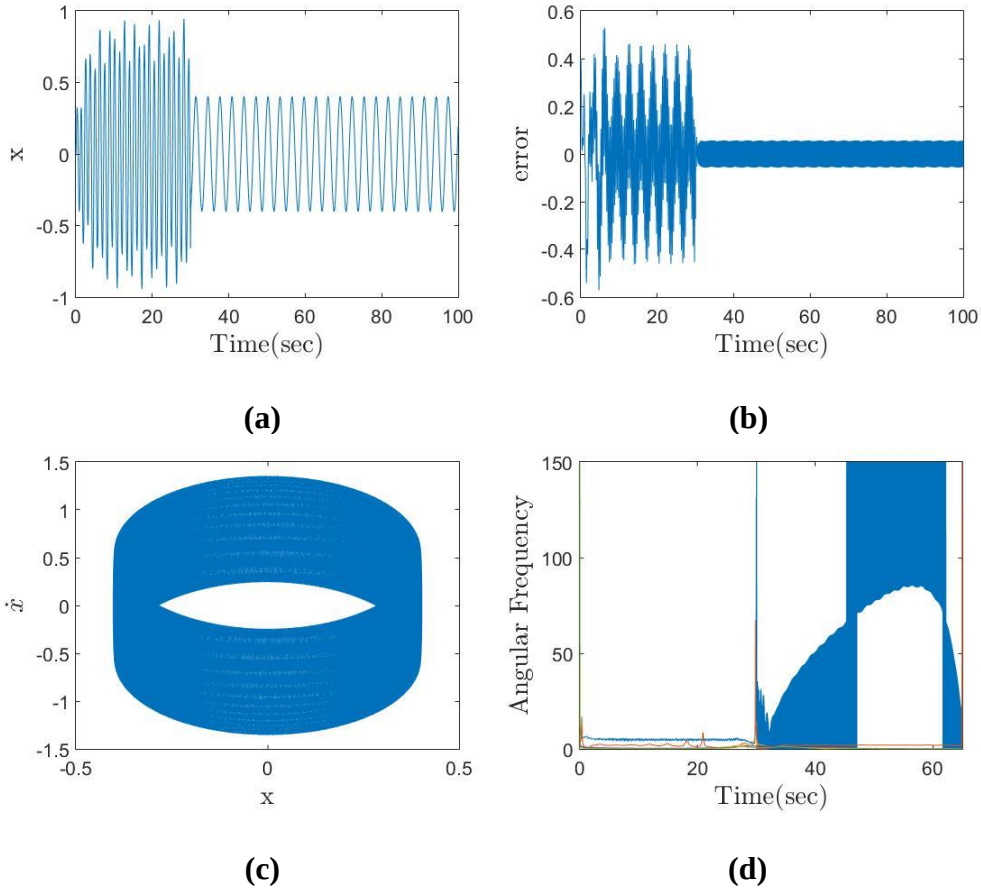

Figure 43 (a) Time response, (b) Error response, (c) Phase portrait, and (d) Instantaneous frequency of the time-delay feedback system with Fuzzy controller initiated at time t = 30 sec and time-delay t_d = 0.22 sec.

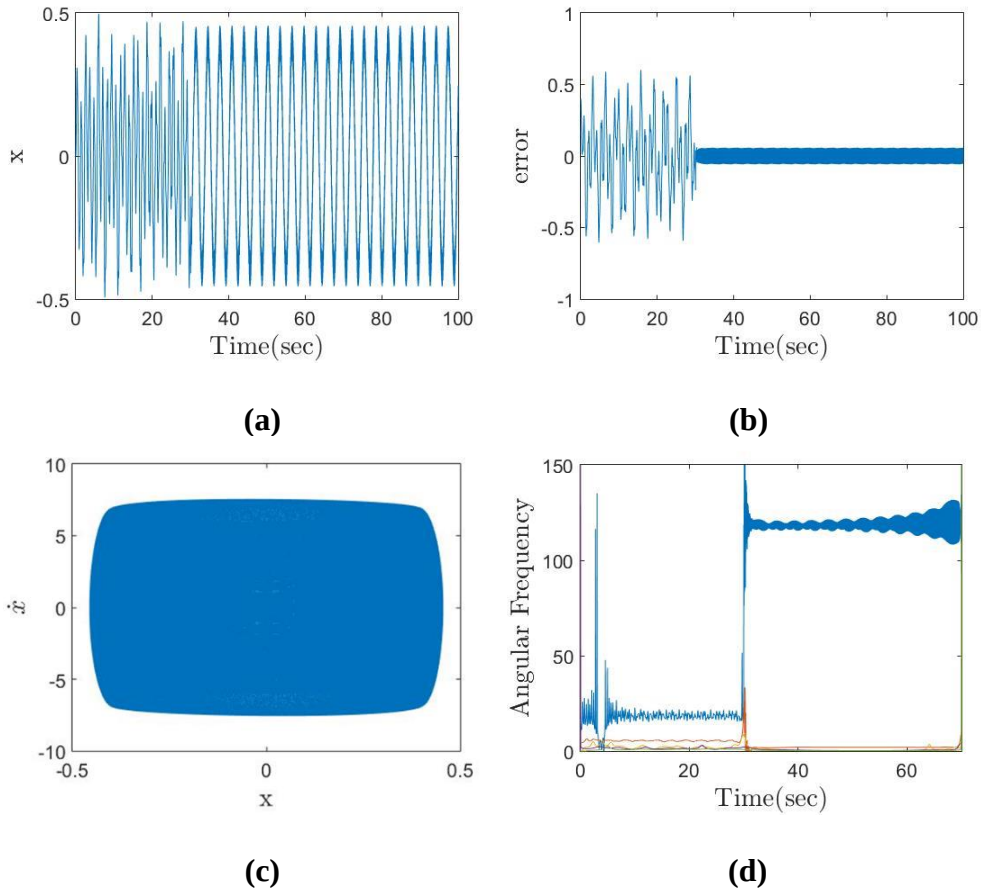

Figure 44 (a) Time response, (b) Error response, (c) Phase portrait, and (d) Instantaneous frequency of the time-delay feedback system with Fuzzy controller initiated at time t = 30 sec and time-delay t_d = 0.27 sec.

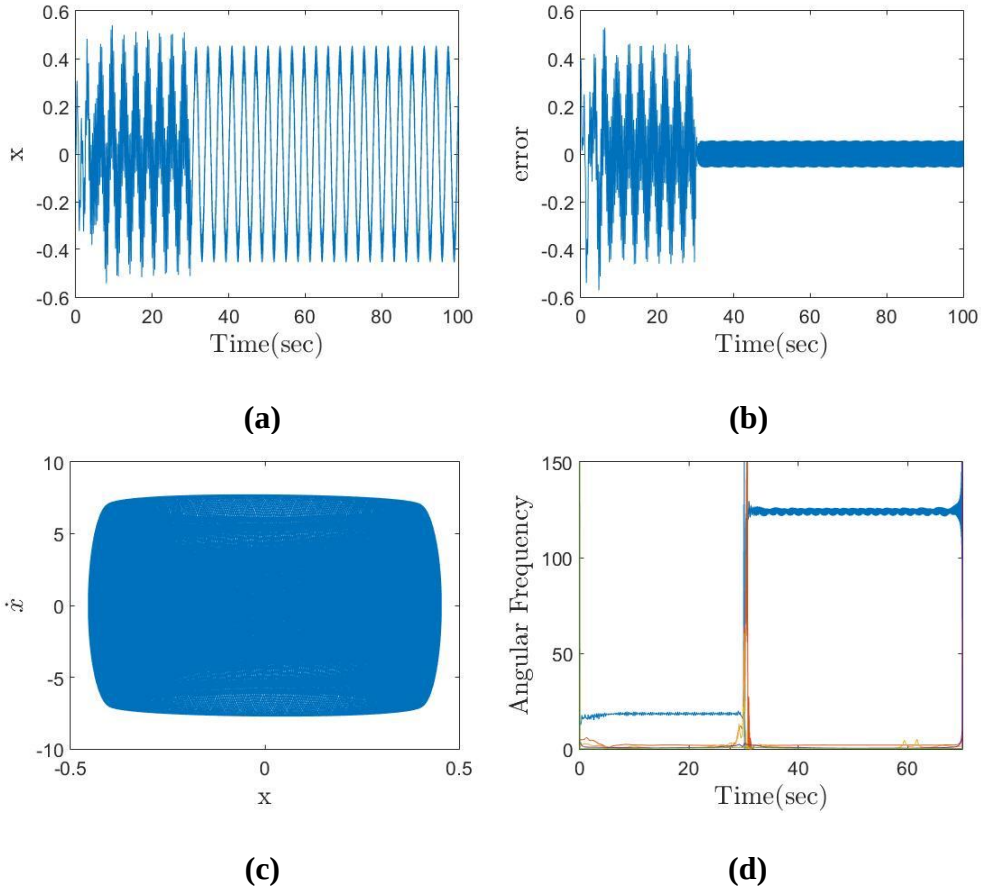

Figure 45 (a) Time response, (b) Error response, (c) Phase portrait, and (d) Instantaneous frequency of the time-delay feedback system with Fuzzy controller initiated at time t = 30 sec and time-delay t_d = 0.3 sec.

The time-delayed feedback system is subsequently engaged with the PID and fuzzy logic controllers for the same 3 time-delay values considered in Figure 30-Figure 32. System parameters used in Figure 33-Figure 35 are also adopted to ensure a common basis for evaluation. Figure 40(a) is the time response of the PID control with $t_d = 0.22$ sec. The controller is initiated at $t = 30$ sec. The phase portrait in Figure 40(c) indicates that the oscillator is in a bifurcated state of quasi-periodic motion and the

instantaneous frequency response in Figure 40(d) shows that a high frequency component is generated as a result. The feedback PID control is seen to instigate an artificial high frequency response that serves to destabilize the oscillator with its bandwidth-limited temporal-modal oscillations [78]. The PID design is applied to the time-delayed feedback system with delayed parameter equals to 0.27 sec and the corresponding responses are presented in Figure 41. Chatter remains prominent in the time response after the controller is brought online at $t = 30$ sec. The phase portrait in Figure 41(c) shows a toroid that is also a closure of unstable manifolds. The corresponding instantaneous frequency in Figure 41(d) confirms an initially quasi-periodic motion of the broadband frequency kind quickly breaking down to a chaotic response. This is the most unstable response of the three time-delayed feedback cases considered herein. The responses of the system with $t_d = 0.3$ sec are presented in Figure 42. They are similar to the responses in Figure 40 except for the observation that the bandwidth-limited temporal-modal oscillations of the high frequency response is alarmingly worse. Figure 43-Figure 45 are the corresponding fuzzy logic controlled responses of the system with t_d being 0.22 sec, 0.27 sec and 0.3 sec, respectively. Although the error chattering in each time responses is comparable to those with the PID controller, the instantaneous frequency plots in Figure 43(d), Figure 44(d), and Figure 45(d) show that the high frequency responses as the results of the control action are non-stationary (time-varying) and broad in bandwidth, thus necessarily indicating that the dynamic state of motion is fast deteriorating under the auspice of the controller. The

corresponding phase portraits in Figure 43-Figure 45 also attest that the system remains highly bifurcated as an aperiodic motion after the controller was initiated.

Both the PID and fuzzy logic controllers induce a high frequency noise after the control action is applied. This is attributed to the fact that the feedback feature inherent of the controller design inadvertently perturbs the oscillator with the higher order nonlinear terms. The instantaneous frequency responses of the time-frequency control indicate that the controller successfully mitigates the noise and stabilizes the time-delay feedback system. PID and fuzzy logic control are seen to reduce the difference between the output and desired signals slightly better than the time-frequency control. However, the error responses of the time-frequency controller are within tolerance and not affecting the proper functioning of the dynamic system. The high frequency responses and broadband temporal-modal oscillations seen in Figure 40-Figure 45 could negatively impact the system with significantly higher power consumption, render poor accuracy, and destabilize the system to ultimate physical deterioration. The time-frequency controller in contrast is feasible for the proper mitigation of the time-delayed feedback oscillator without the issues intimately associated with the PID and fuzzy logic control methodologies.

Concluding Remarks

Time-delayed feedback systems are sensitively prone to dynamic instability characterized by nonlinear, nonstationary time response and broad bandwidth spectral response. Such a state of instability in manufacturing would result in premature tool

breakage, increased wear rate, and poor work piece quality. The solution presented in the chapter can improve the performance, quality, and capacity of manufacturing enormously by applying the feedback force since sometimes the time-delay parameter cannot be adjusted. A wavelet-base time-frequency controller with parallel online modeling was designed and subsequently implemented to control and stabilize the dynamic response of the non-autonomous time-delayed feedback system following a desired harmonic target of a specified frequency and amplitude. The non-autonomous time-delayed feedback oscillator with various time-delay parameters were studied. With the controlled motions being unconditionally stationary and quasi-periodically stable, the controller demonstrated the ability to mitigate the severe complex state of unstable motions dictated by the higher order feedback system.

CHAPTER V

TIME-DELAYED VIBRO-IMPACT OSCILLATOR

Time-delayed vibro-impact oscillators are commonly found in engineering. Chaotic motion and ultimate damage are probable if these oscillators are not properly controlled. Knowing the dynamic characteristics of these systems is essential to controlling them. In this chapter, system parameters such as delayed time and driving frequency are considered to generate system responses that are subsequently processed using phase plot and instantaneous frequency. As discussed in previous chapters, changing driving frequency affects system responses in a profound way and time-delay may destabilize a system into catastrophe. The behaviors of time-delayed vibro-impact systems are significantly more complex than those of the two oscillators discussed in Chapter III and Chapter IV, for the reason that such systems demonstrate not only vibro-impact gracing instability but also time-delayed induced chaos.

Model System

Grazing bifurcation generated by the collision of a periodic orbit with a switching manifold in a non-smooth system is potent for generating complex dynamics. The dynamic behaviors in the immediate neighborhood of grazing experienced by an impact oscillator are inherently unstable. The one degree-of-freedom vibro-impact model shown in Figure 7 considers the motion of the cart at low speed subject to a force

of a sinusoidal profile. The corresponding dynamic equation of the vibro-impact motion defined using the specified coordinate system is

$$M\ddot{x} + R\dot{x} + Kx = A\omega^2 \sin(\omega t) - k_{wall}(x-d)H[x-d] \tag{5.1}$$

where M is the mass of the moving cart, R is the damping coefficient, K is the stiffness of the spring, A is the excitation amplitude, and ω is the excitation frequency. The impact wall is located at $x = d$ and its stiffness is k_{wall} which is assumed to be much greater than K. The stiffness of the spring is dictated by a Heaviside function, $H[x-d]$. Eq. (5.1) can be further manipulated to be of the following dimensionless form:

$$\ddot{y} = \alpha\ \omega^2 \sin(\omega\tau) - 2\eta\dot{y} - y - \beta(y-e)H[y-e] \tag{5.2}$$

where $y = x/x_0$ is the dimensionless displacement, $\dot{y} = \dot{x}/x_0$ is the dimensionless velocity, and $\ddot{y} = \ddot{x}/x_0$ is the dimensionless acceleration. The first term on the right-hand side of Eq. (5.2) is the excitation force with $a = A/x_0$ being the dimensionless excitation amplitude and $\tau = \omega_n t$ being the dimensionless time in which $\omega_n = \sqrt{K/M}$ defines the nature frequency. Also, $\eta = c/(2M\omega_n)$ is the damping ratio, $\beta = k_{wall}/K$ is the stiffness ratio, and $e = d/x_0$ is the dimensionless gap where x_0 is defined as the arbitrary reference distance.

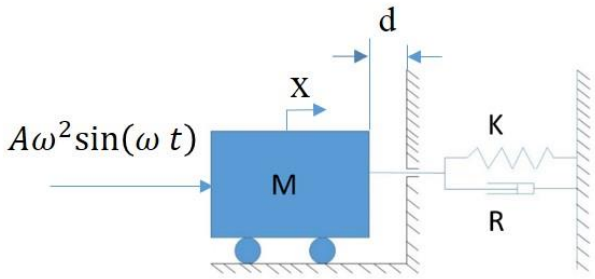

Figure 46 Time-delayed vibro-impact model system.

When a time-delayed reaction damping force from the wall is considered, the equation of motion becomes

$$\ddot{y} = \alpha\,\omega^2 \sin(\omega\tau) - 2\eta\dot{y} - y - \beta(y-e)H[y-e] - \gamma\dot{y}[t-t_d]H[y[t-t_d]-e] \qquad (5.3)$$

where γ is the damping factor, e is the damping ratio from the wall, and t_d is the time-delay parameter. The damping force is interpreted as a delayed feedback response of the cart impacting the wall.

Dynamics and System Properties

In the following sections the innate dynamics of the oscillator is explored first to study the sensitivity of the system's response to slightly different time-delay inputs. All the system parameters in Eq. (5.3) are assumed to be positive with the following values: $\alpha = 0.7$, $e = 1.26$, $\beta = 29$, $\eta = 0.01$, and $\gamma = 0.1$. The external driving frequency is set at $\omega = 0.8$ rad/s. A dynamic model of the time-delayed feedback oscillator is built in MATLAB/Simulink and numerically time-integrated using a fourth-order Runge–Kutta

algorithm. The initial velocity and displacement are both zeros. An integration time step of 10^{-3} sec is used for all the three cases investigated in the present section.

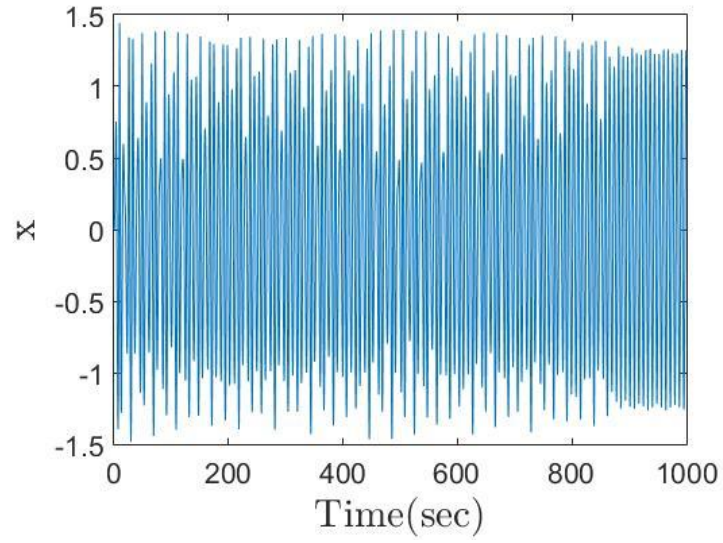

(a)

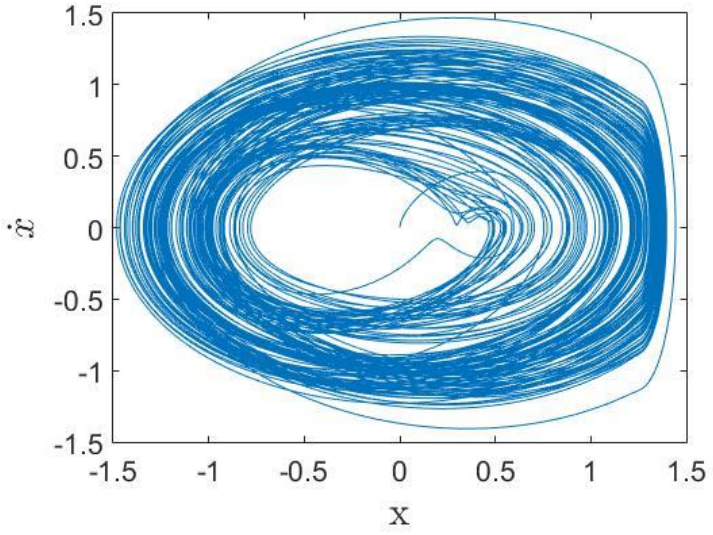

(b)

Figure 47 (a) Time response and (b) phase portrait of the time-delayed vibro-impact oscillator with time-delay t_d = 0.05 sec.

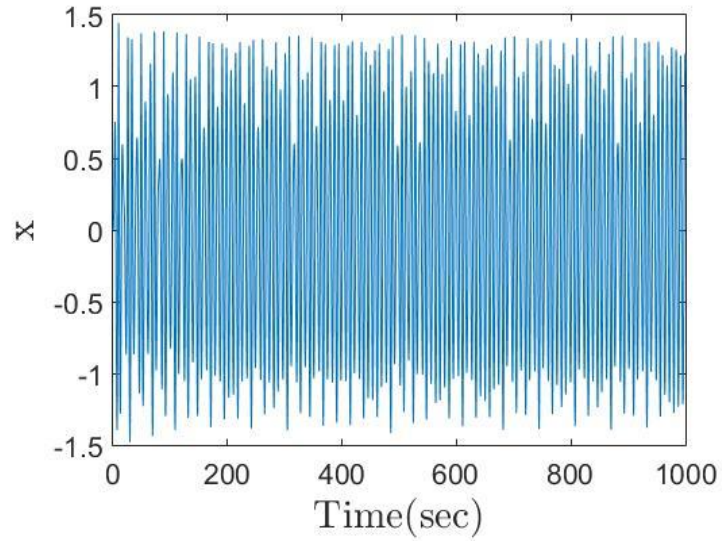

(a)

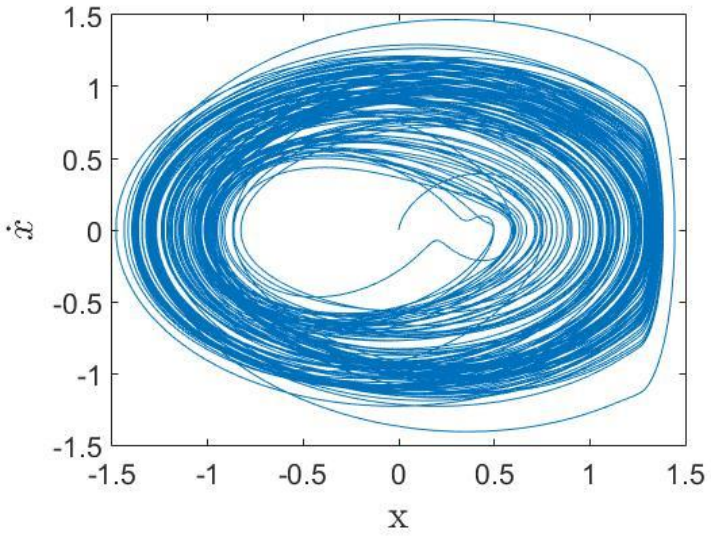

(b)

Figure 48 (a) Time response and (b) phase portrait of the time-delayed vibro-impact oscillator with time-delay t_d = 0.1 sec.

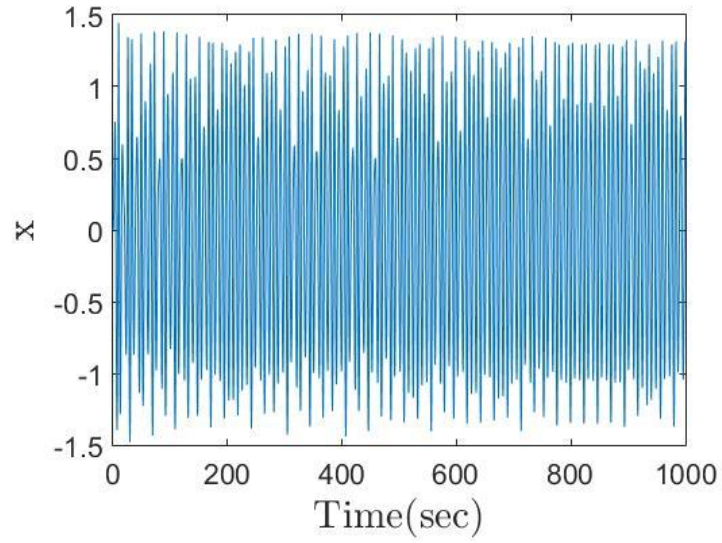

(a)

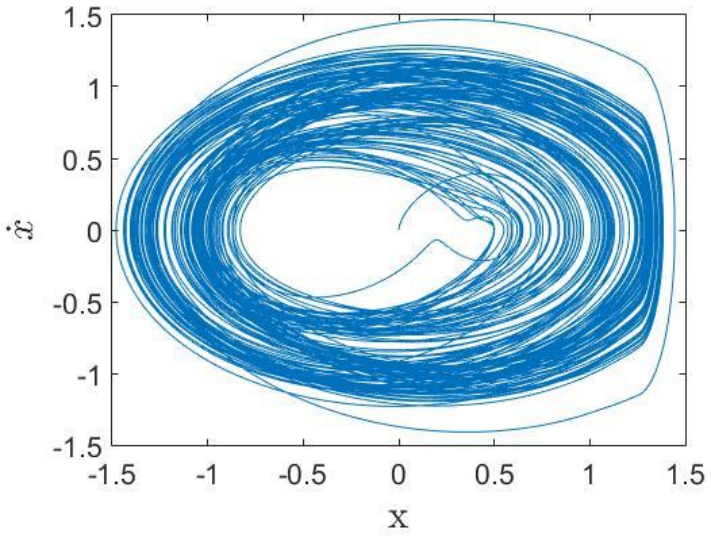

(b)

Figure 49 (a) Time response and (b) phase portrait of the time-delayed vibro-impact oscillator with time-delay t_d = 0.15 sec.

The time-delay parameter set for the first case is $t_d = 0.05$ sec. The corresponding time response of the oscillator shown in Figure 47(a), though bounded, is

a state of dynamic instability. As will be made explicit later, the particular t_d being considered renders a bifurcated route-to-chaos behavior that is also of broad spectral bandwidth. The associated phase portrait in Figure 47(b) conveys a better picture of the time-delayed feedback system. The cluster of trajectories seen in the center of the figure registers the singularities fundamental to the time-delayed feedback dynamics of the oscillator. Together the two figures indicate that the response is bounded in the time-domain while simultaneously becoming unstably broadband in the frequency-domain due to the rapid switching of the infinite number of unstable periodic orbits (UPOs). It is infeasible to mitigate such a state of instability with linear control theory because of the feedback term in the equation of motion. When the time-delay parameter t_d is set to be 0.1 sec, the system displays similar nonlinear behaviors. Figure 48(a) and Figure 48(b) show a chaotic state of response with a large number of different frequencies and evidences of discontinuity. Figure 49 presents the responses of the last case in which $t_d = 0.15$ sec. The phase portrait indicates similar chaotic motion. In Figure 49(a), there is no converge response seen after 900 sec. Comparing all the time responses, time-delay parameter affects the system more significantly when its value becomes larger. The UPOs in the phase portraits that correspond to the 3 different time-delay parameters indicate the level of difficulty in regulating the system with contemporary control approach. To address the nonlinearity due to the time-delayed feedback gain dictated by the impact feedback terms in Eq. (5.1), a nonlinear control methodology is required to ensure stability.

Bifurcation Analysis

To investigate the impact of time delay parameter a bifurcation analysis is performed. With the same parameter and simulation environment, frequency is increased from 0.79 to 0.81. The result presented in Figure 50 shows a prominent section of bifurcation between 0.8 and 0.802, which is a small range of frequency. However, as the time-delay parameter is increased from $t_d = 0$ to $t_d = 0.15$, the frequency range that registers bifurcation becomes wider, indicating that time-delay is significant in perturbing the system to chaotic state. To control this highly nonlinear time-delayed vibro-impact oscillator, a wavelet-based time-frequency control scheme is developed in the next chapter.

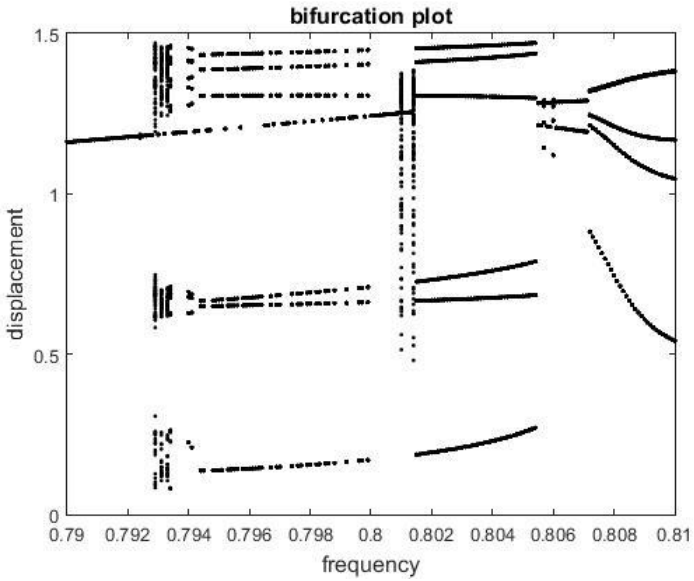

(a)

Figure 50 Bifurcation analysis results with time-delay (a) $t_d = 0$, (b) $t_d = 0.05$, (c) $t_d = 0.1$, and (d) $t_d = 0.15$.

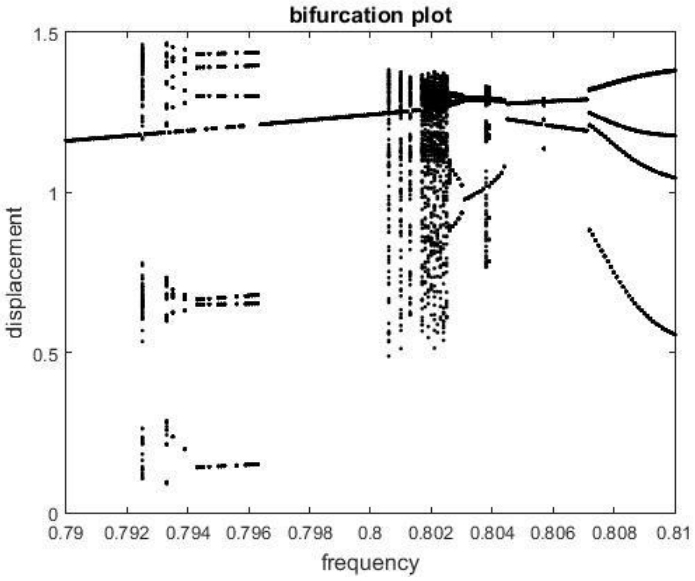

(b)

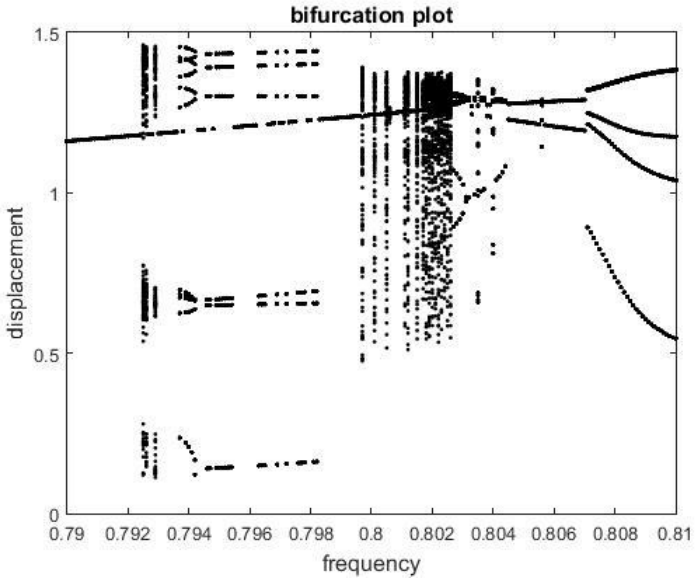

(c)

Figure 50 Continued.

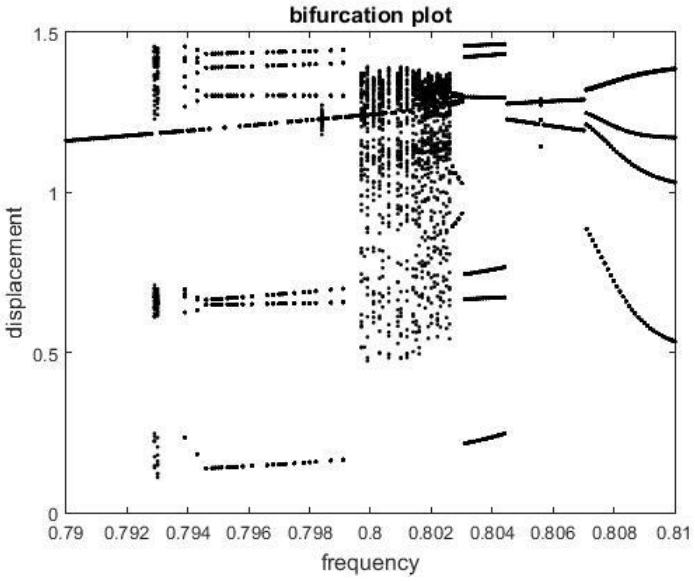

(d)

Figure 50 Continued.

CHAPTER VI

CONTROL OF TIME-DELAYED VIBRO-IMPACT OSCILLATOR

Adaptability of Time-Frequency Control

In the present chapter the wavelet-based time-frequency control concept with local adaptability is explored and evaluated to establish its feasibility in mitigating the complex state of dynamic instability of the time-delayed feedback oscillator which demonstrates nonlinear bifurcated behaviors as seen in Figure 47-Figure 49 in Chapter V. The nonlinear system is incorporated into the control scheme given in Figure 6 and identical integration time step and time-delay t_d are employed to maintain consistency. The $N \times 1$ initial filter vectors for both filters are calculated following the algorithm elaborated in Chapter II. Regression step sizes are adjusted by meeting the conditions given in Eq. (2.44) and Eq. (2.126) in Chapter II. The data size N is discretionarily selected as 256. The desired target is a sinusoidal function, $\alpha \sin(\omega t)$, where the target frequency is $\omega = 0.8$ rad/s and the amplitude is $\alpha = 0.7$. The time response in Figure 51(a) corresponds to the case in which $t_d = 0.05$ sec. Once the system response reaches steady-state the controller is brought online at $t = 300$ sec. The difference between the controlled response and the desired target in Figure 51(b) is satisfactory. In contrast with Figure 47(b) where the spectral response is broad in bandwidth, the phase portrait in Figure 51(c) indicates that the oscillator is now in a periodic state of stable motion moving in a limit-cycle bounded between -0.6 and +0.6. The corresponding instantaneous frequency in Figure 51(d) also attests to the same observation by showing

that the system response is a bandwidth-limited temporal-modal structure indicative of dynamic instability and route-to-chaos. After the controller is applied, the response stabilizes into a stable manifold of a definitive topology characteristically different from Figure 47(a) where a discontinuous motion is indicated. This instability state of motion is seen to abruptly return at the moment the controller is brought offline at $t = 900$ sec. Without the auspice of the nonlinear time-frequency controller the oscillator displays deteriorating time response (Figures 51(a) and 51(b)) and time-varying, broad bandwidth spectral response (Figure 51(d)) that are characteristically chaotic.

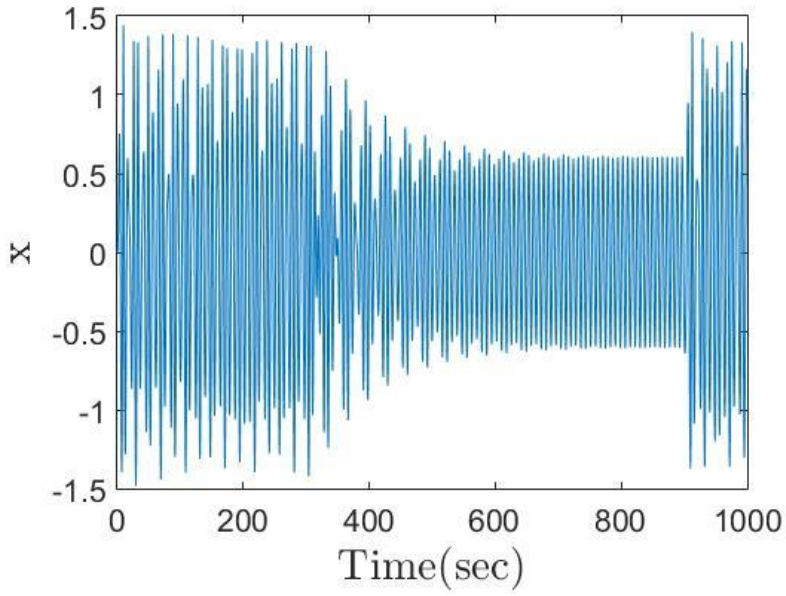

(a)

Figure 51 (a) Time response, (b) Error response, (c) Phase portrait, and (d) Instantaneous frequency of the time-delayed vibro-impact oscillator with controller initiated at t = 300 sec, closed at t = 900 sec, and time-delay t_d = 0.05 sec.

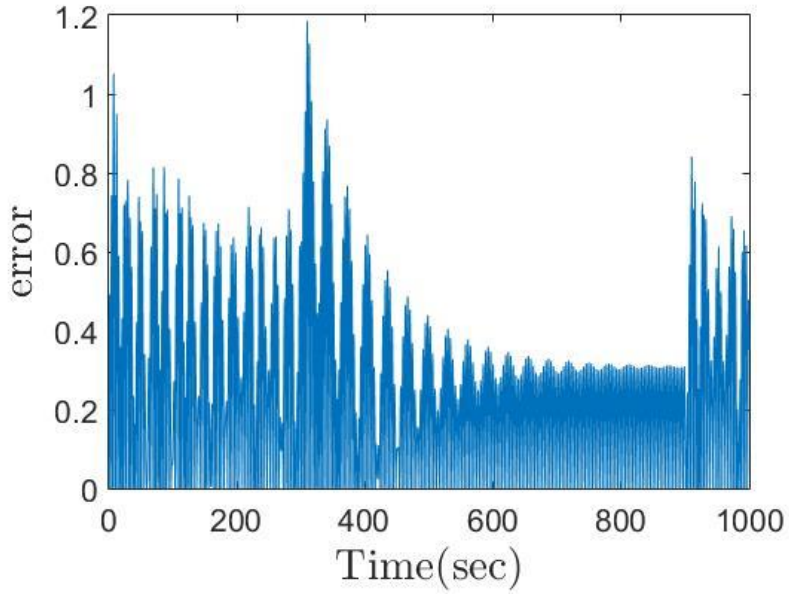

(b)

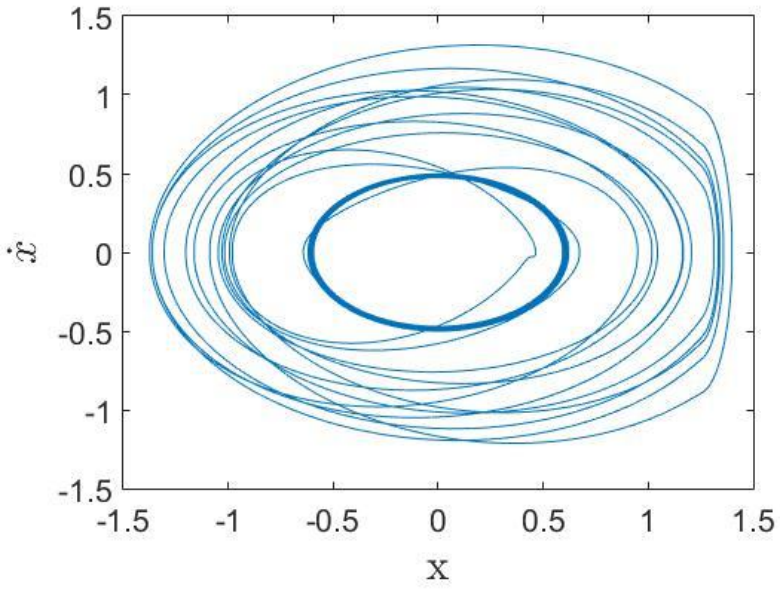

(c)

Figure 51 Continued.

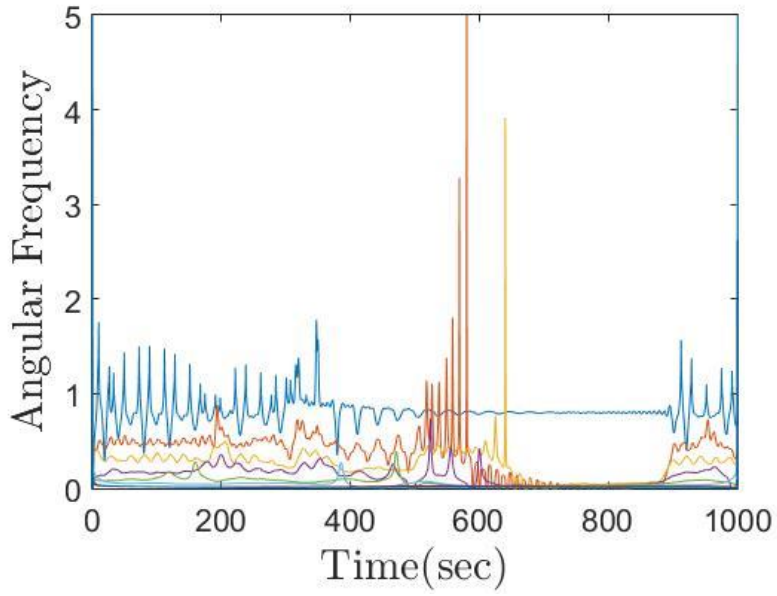

(d)

Figure 51 Continued.

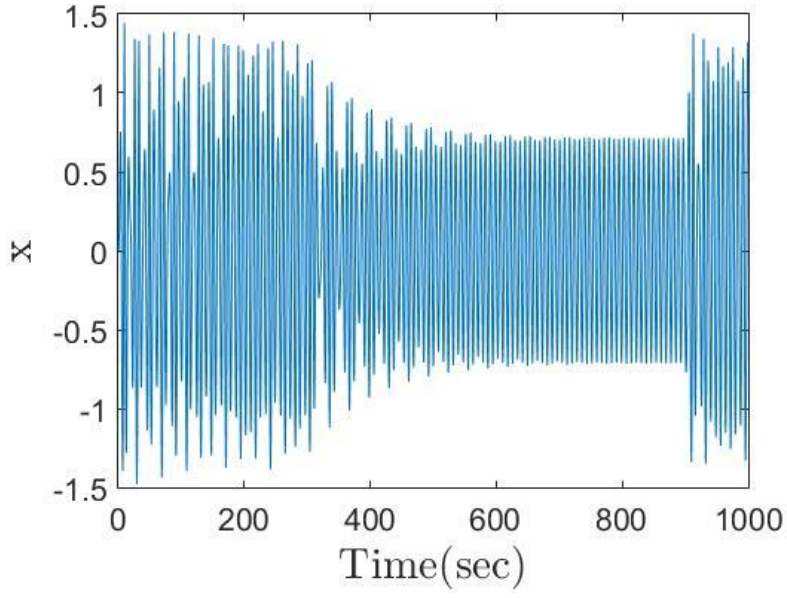

(a)

Figure 52 (a) Time response, (b) Error response, (c) Phase portrait, and (d) Instantaneous frequency of the time-delayed vibro-impact oscillator with controller initiated at t = 300 sec, closed at t = 900 sec, and time-delay t_d = 0.1 sec.

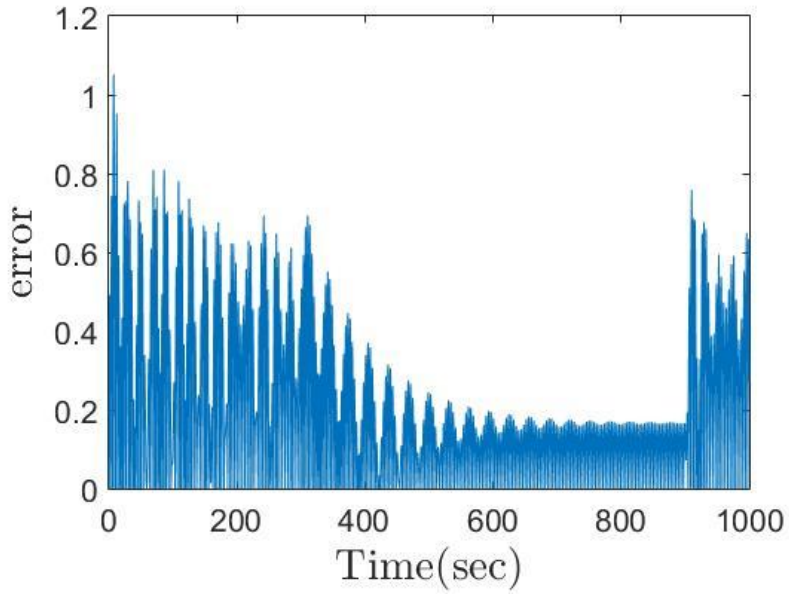

(b)

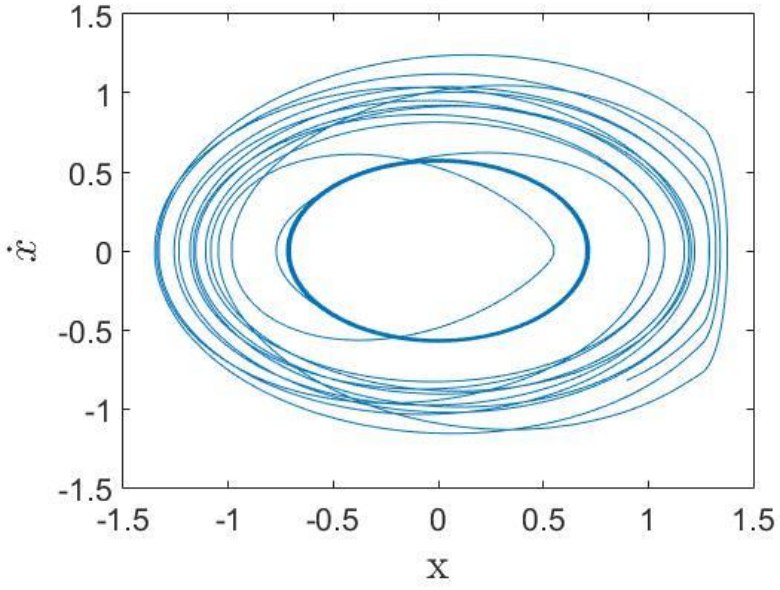

(c)

Figure 52 Continued.

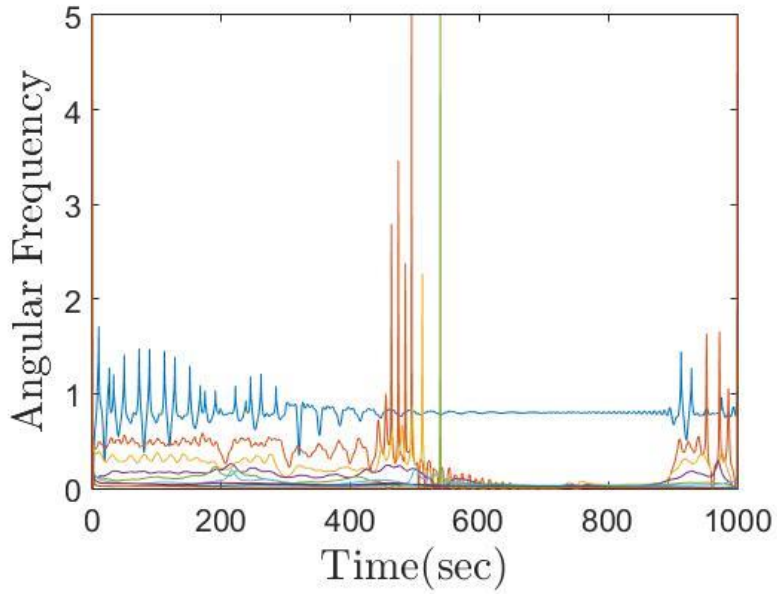

(d)

Figure 52 Continued.

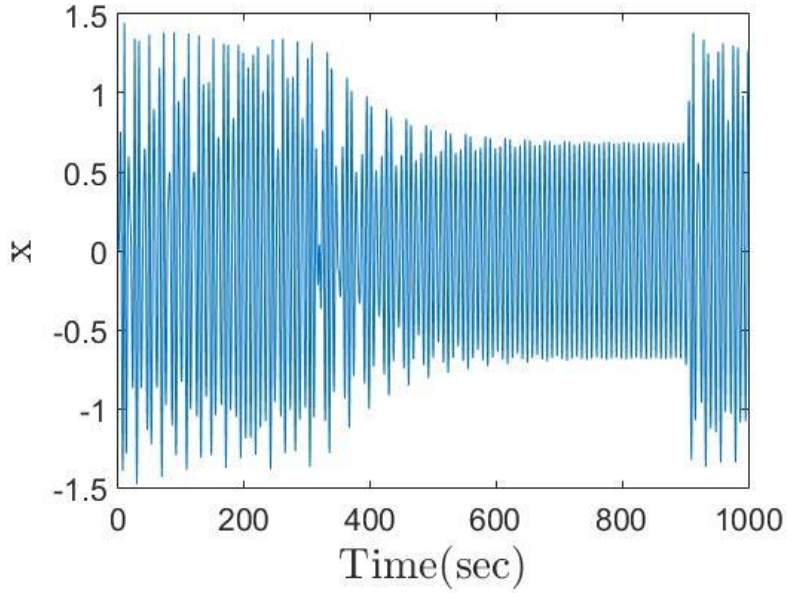

(a)

Figure 53 (a) Time response, (b) Error response, (c) Phase portrait, and (d) Instantaneous frequency of the time-delayed vibro-impact oscillator with controller initiated at t = 300 sec, closed at t = 900 sec, and time-delay t_d = 0.15 sec.

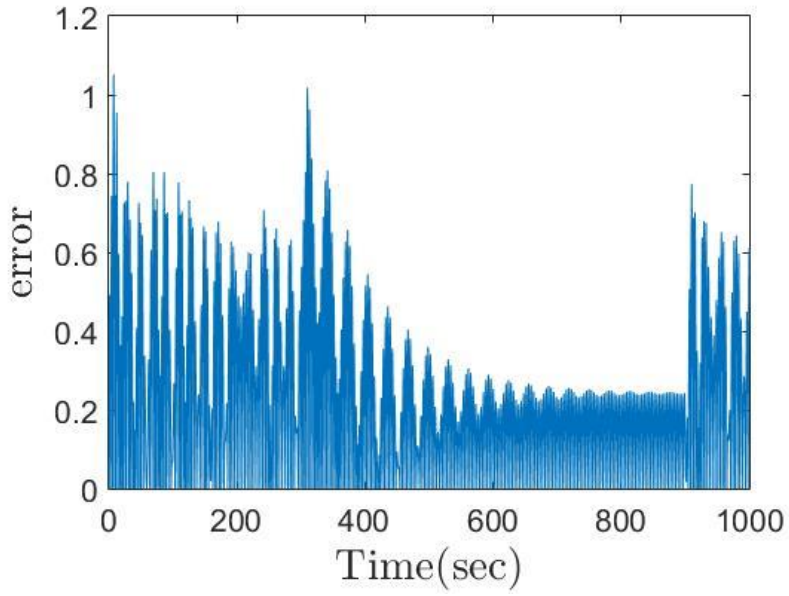

(b)

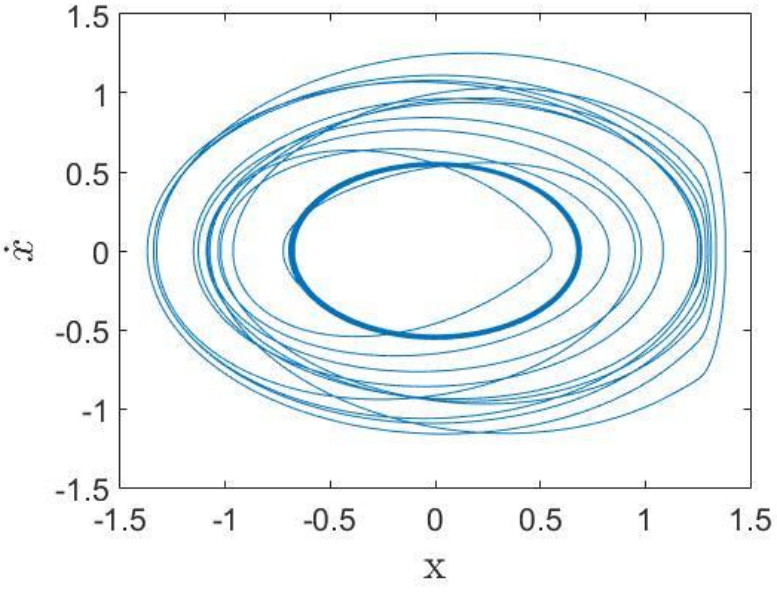

(c)

Figure 53 Continued.

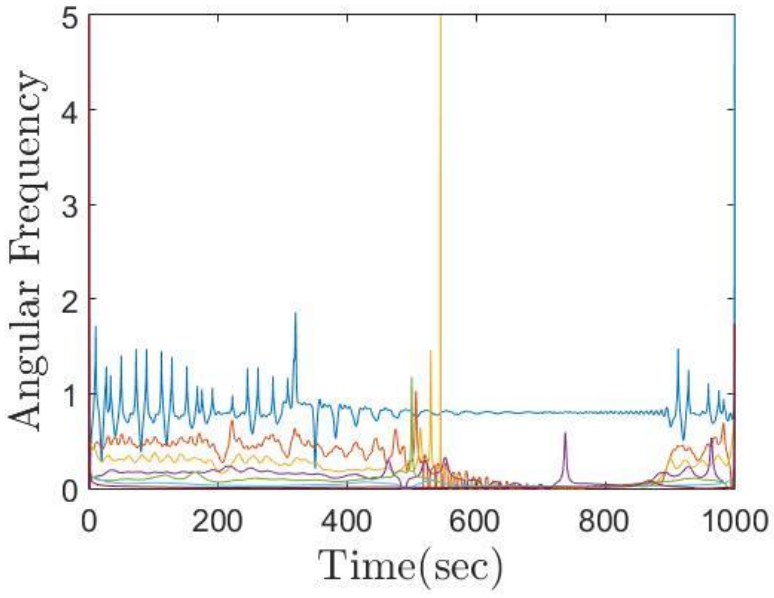

(d)

Figure 53 Continued.

The time-delayed vibro-impact oscillator also displays highly nonlinear behaviors in the case with $t_d = 0.1$. Following the same desired target, the chaotic oscillator is seen in Figure 52(a) to respond in no time to the exertion of the controller initiated at time $t = 300$ sec. The associated phase portrait in Figure 52(c) indicates a stable motion of periodic type. The corresponding instantaneous frequency for the controlled response in Figure 52(d) shows that as soon as the controller is engaged the broad bandwidth chaotic motion is negated and the oscillator is stabilized into following a time-invariant spectrum of a finite number of frequencies. This is also supported by Figure 52(b) in which the difference between the desired target and the controlled output in Figure 52(b) is periodic, thus stationary. The noted periodicity and stationarity are

lost upon the disengagement of the controller at t=900s. Chaotic response is seen to restore just as the case with $t_d = 0.1$.

The controller demonstrates similar performance for the case with time-delay $t_d = 0.15$. After turning on the controller at time $t = 300$ sec to track the desired target with $\omega = 0.8$ and $\alpha = 0.7$, the time response in Figure 53(a) is effectively mitigated. The phase portrait in Figure 53(c) indicates the controlled response is a limit-cycle type of motion whose spectral response in Figure 53(d) is characteristically not unlike Figure 53(d). That is, the driving frequency of the oscillator at $\omega = 0.8$ is properly tracked despite of the omnipresent vibro-impact feedback gains. The manifold of many UPOs in Figure 49(b) signifying the state of dynamic instability re-emerges along with the unstable state of aperiodic motions when the controller is turned off at t=900s as seen in Figure 53(d). Figure 51-Figure 53 show that the motions of the harmonically excited time-delayed vibro-impact oscillator under the jurisdiction of the nonlinear time-frequency controller are without exception stationary, bounded, and predictable, complying with the prescribed target response having specific temporal and spectral properties.

Evaluation of Controlled Performance

The nonlinear time-frequency controller design is evaluated in this section against 2 common controller designs, namely, PID and fuzzy logic control (FLC), for performance in mitigating the time-delayed feedback induced instabilities seen in Figure 47-Figure 49. The PID scheme employed for tracking the output displacement of the

time-delayed vibro-impact oscillator in Eq. (6.1) is given in Figure 54. The PID controller is designed based on the followings,

$$u(n) = k_p e(n) + k_i \left[u(n-1) + \frac{e(n) + e(n-1)}{2} dt \right] + k_d \frac{e(n) - e(n-1)}{dt} \tag{6.1}$$

where $u(n)$ is the output from the controller, dt is the integration time step, $e(n)$ is the error between the desired signal and the actual output from the system. Control parameters k_p, k_i, and k_d are proportional gain, integral gain, and derivative gain, respectively. The optimal gain values selected for the PID controller are $k_p = 2.2083$, $k_i = 0$, and $k_d = 0$.

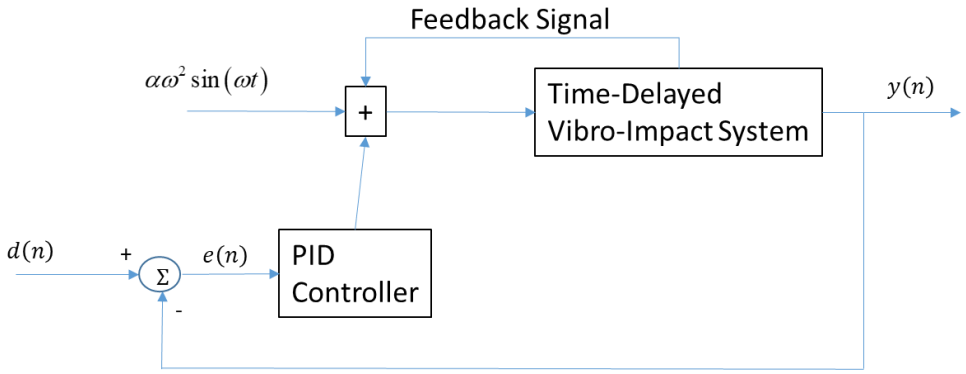

Figure 54 Displacement tracking of time-delayed vibro-impact oscillator using PID.

The FLC scheme employed for output signal tracking of the time-delayed system is found in Figure 55 with $e(n)$ being the error between the desired target, $d(n)$, and the output signal, $y(n)$.

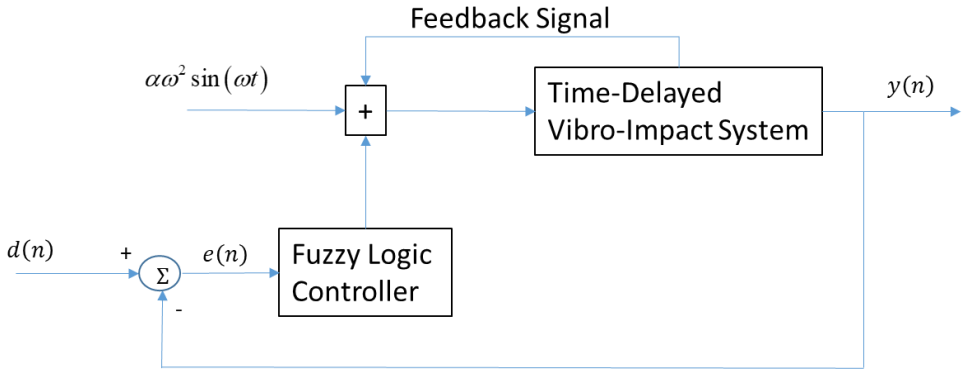

Figure 55 Displacement tracking of time-delayed vibro-impact oscillator using FLC.

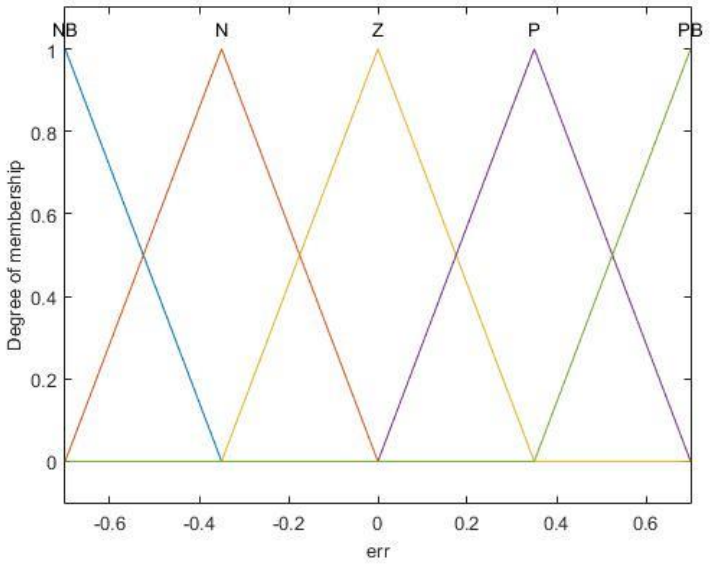

Figure 56 Input membership function

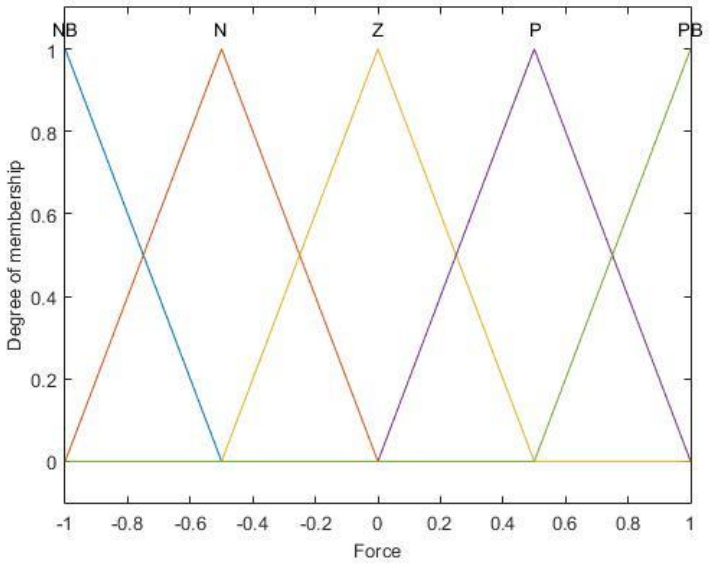

Figure 57 Output membership function

Table 3 Fuzzy Rules of Fuzzy Logic Controller

Rule	Description
1	If (err is NB) then (Force is NB)
2	If (err is N) then (Force is N)
3	If (err is Z) then (Force is Z)
4	If (err is P) then (Force is P)
5	If (err is PB) then (Force is PB)

$e(n)$ is selected as the input to the fuzzy logic controller. The corresponding membership functions and fuzzy rules are indicated in Figure 56, Figure 57 and Table 3, where NL, NB, N, Z, P, PB, and PL stand for negative large, negative big, negativity, zero, positive, positive big, and positive large, respectively.

Although increasing the number of fuzzy rules can potentially improve performance, the fuzzy logic controller is deliberately designed to be simple out of the following considerations. The first is that the controlled output from the fuzzy logic controller relies extremely on the input. The second is that the feedback signal of the time-delayed vibro-impact system can be considered as the noise that distorts the information pertaining to the true dynamic state of the system. The effect becomes more prominent when the system reaches steady-state and induces severe chattering in the output signal. The fuzzy rules presented in Table 3 are the result of considering the above which is also tested to be sufficient for demonstration purpose.

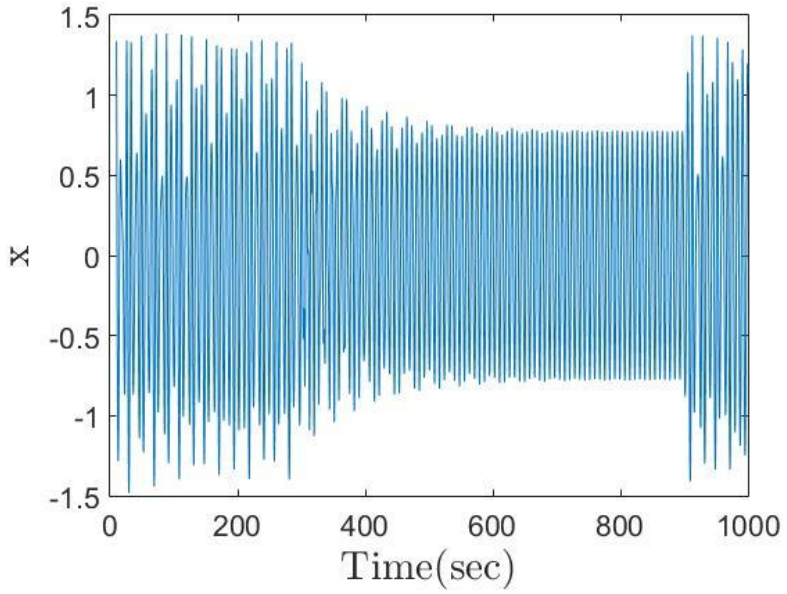

(a)

Figure 58 (a) Time response, (b) Error response, (c) Phase portrait, and (d) Instantaneous frequency of the time-delayed vibro-impact oscillator with PID controller initiated at t = 300 sec, closed at t = 900 sec, and time-delay t_d = 0.05 sec.

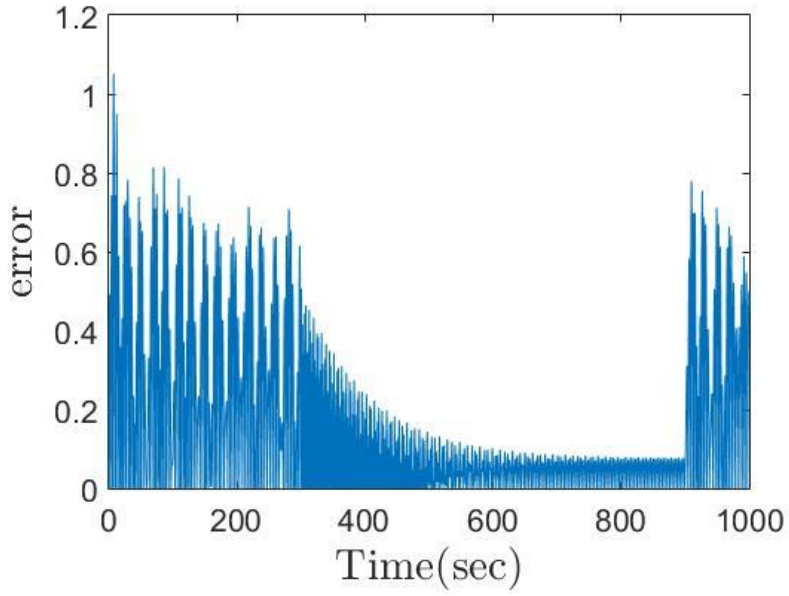

(b)

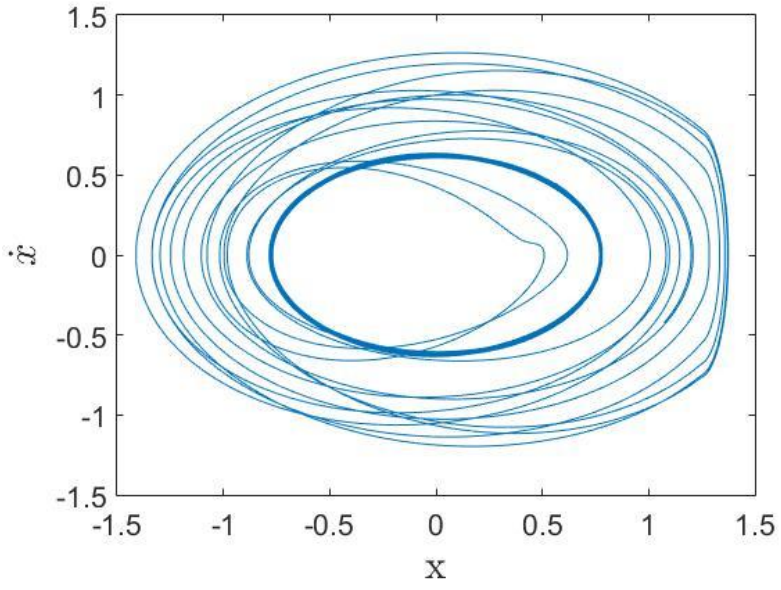

(c)

Figure 58 Continued.

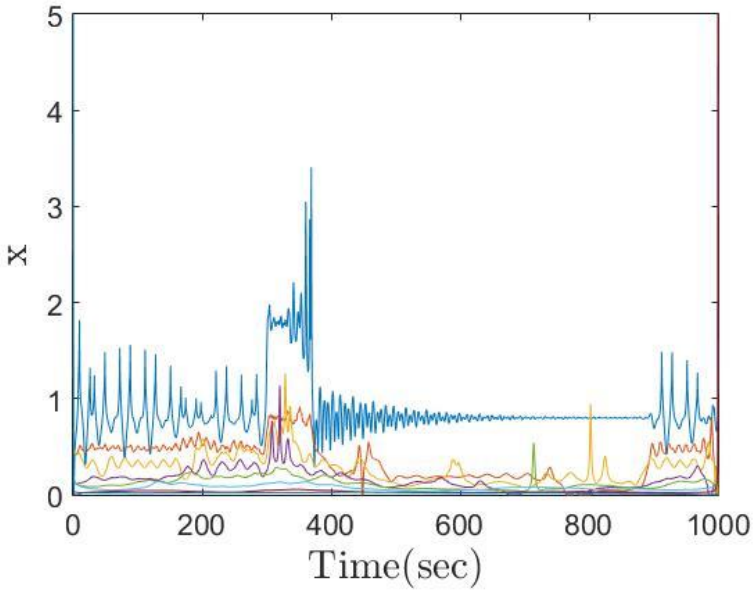

(d)

Figure 58 Continued.

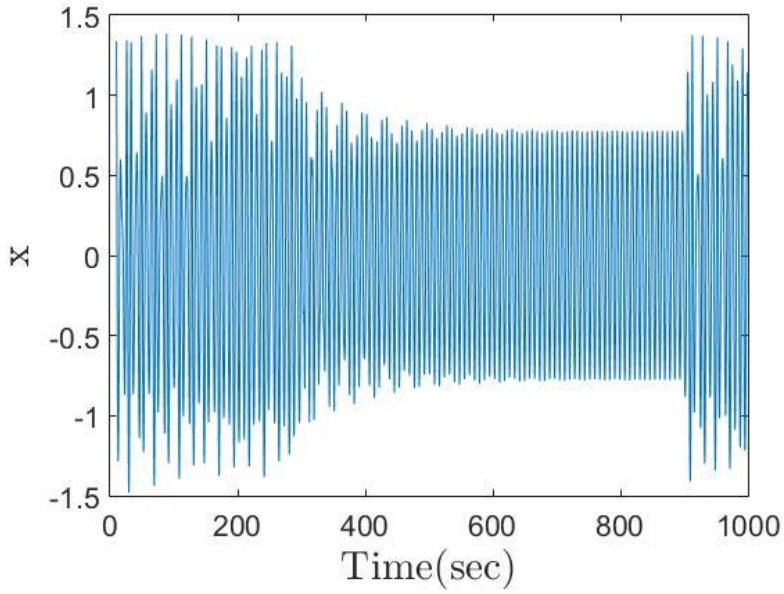

(a)

Figure 59 (a) Time response, (b) Error response, (c) Phase portrait, and (d) Instantaneous frequency of the time-delayed vibro-impact oscillator with PID controller initiated at t = 300 sec, closed at t = 900 sec, and time-delay t_d = 0.1 sec.

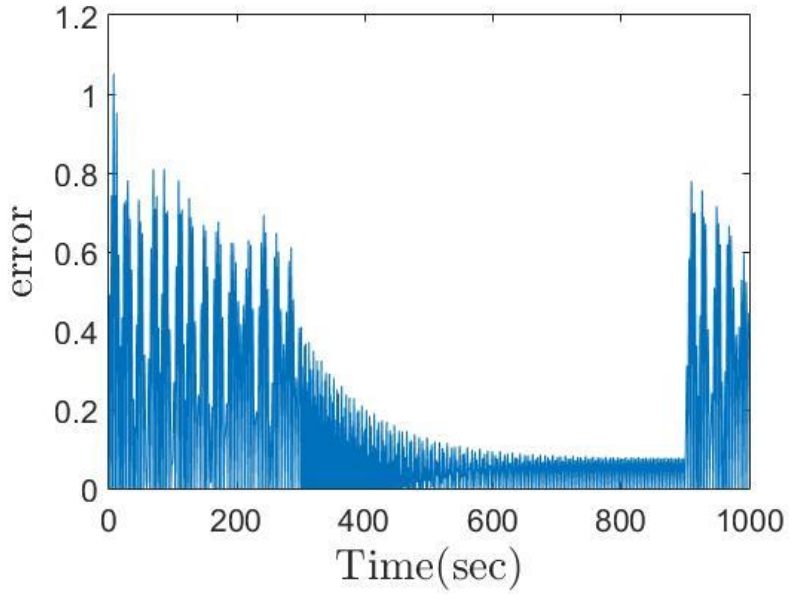

(b)

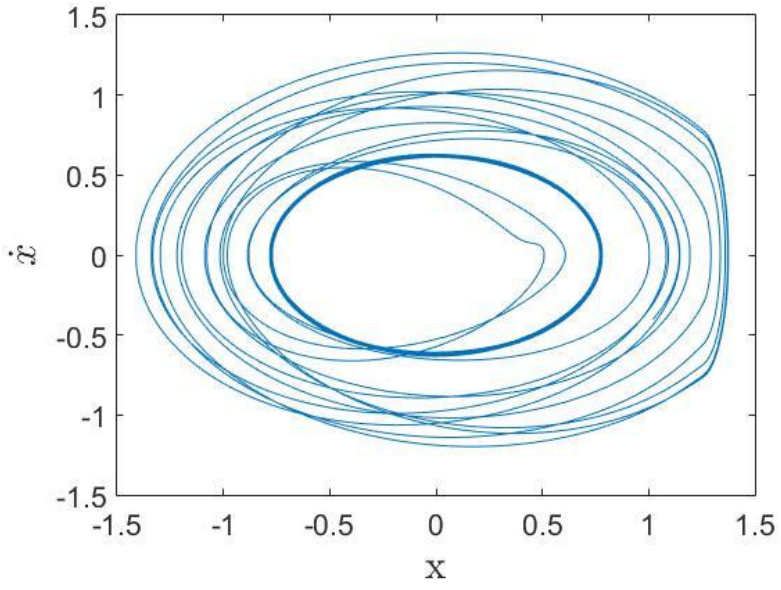

(c)

Figure 59 Continued.

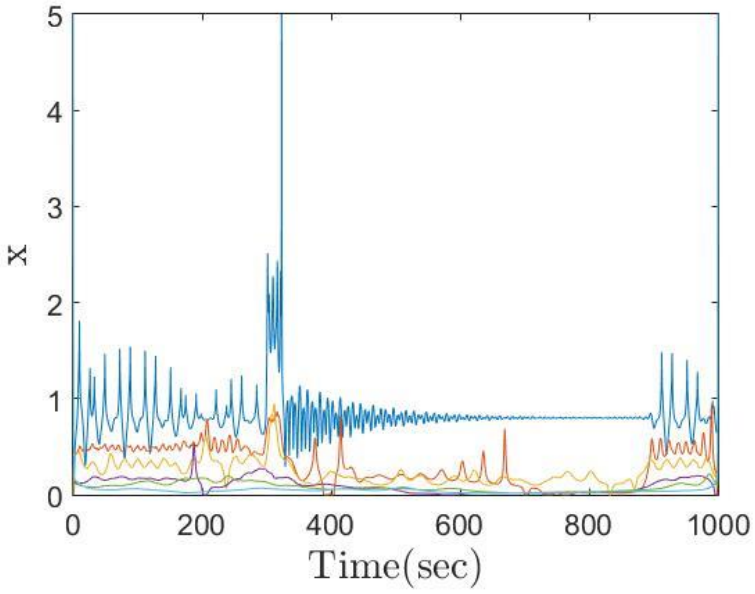

(d)

Figure 59 Continued.

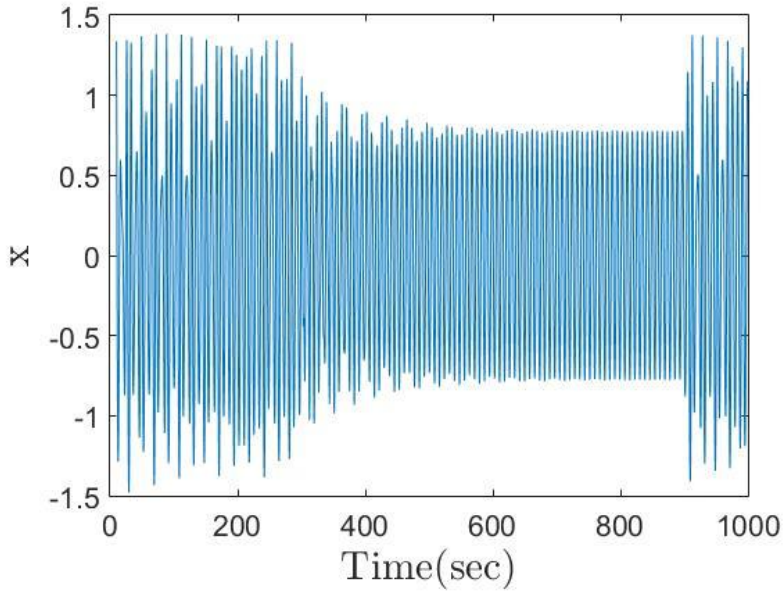

(a)

Figure 60 (a) Time response, (b) Error response, (c) Phase portrait, and (d) Instantaneous frequency of the time-delayed vibro-impact oscillator with PID controller initiated at t = 300 sec, closed at t = 900 sec, and time-delay t_d = 0.15 sec.

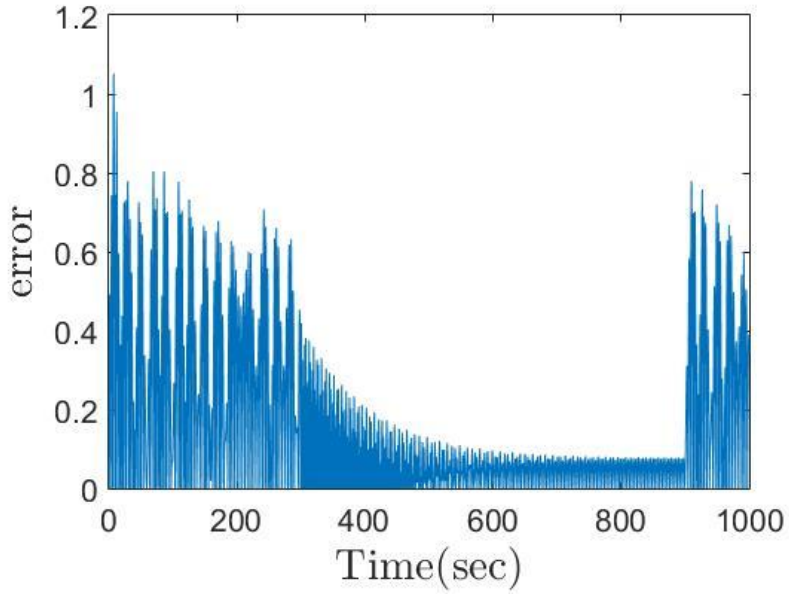

(b)

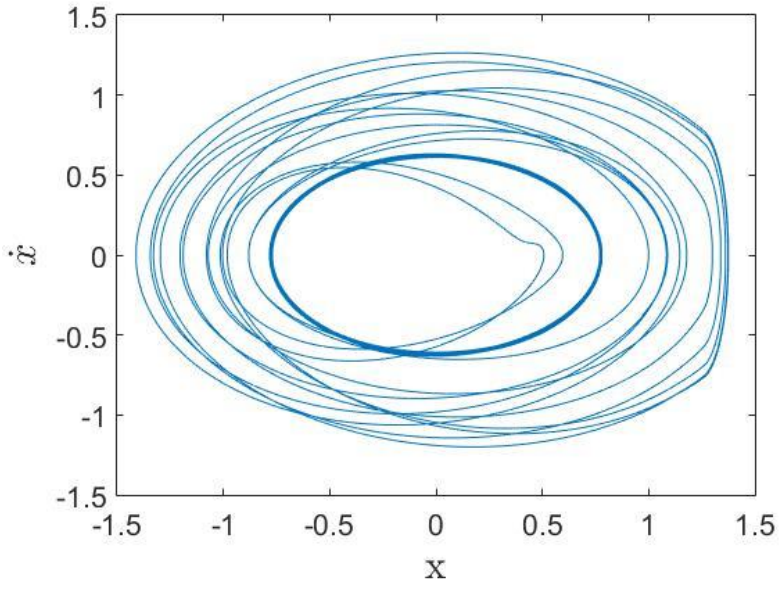

(c)

Figure 60 Continued.

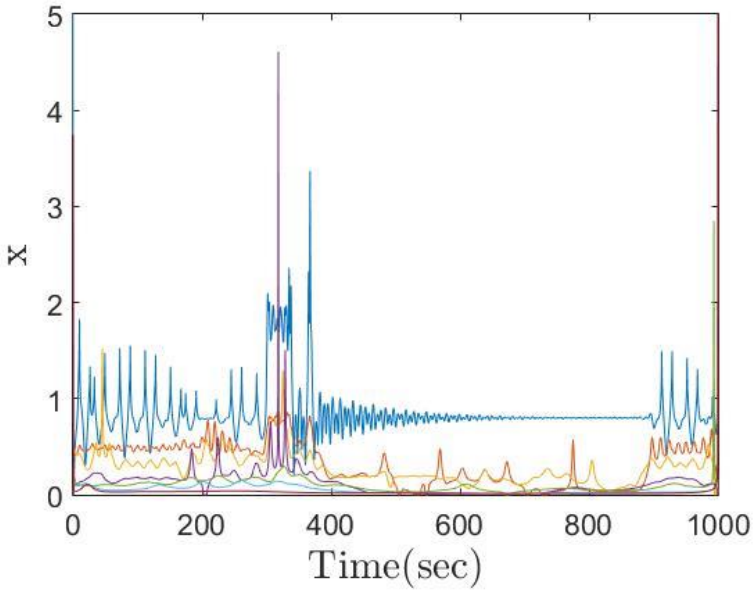

(d)

Figure 60 Continued.

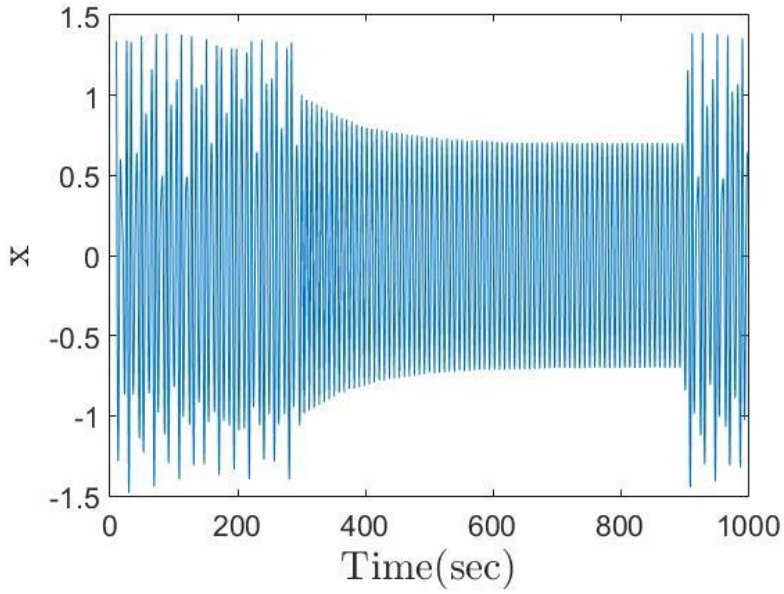

(a)

Figure 61 (a) Time response, (b) Error response, (c) Phase portrait, and (d) Instantaneous frequency of the time-delayed vibro-impact oscillator with Fuzzy controller initiated at t = 300 sec, closed at t = 900 sec, and time-delay t_d = 0.05 sec.

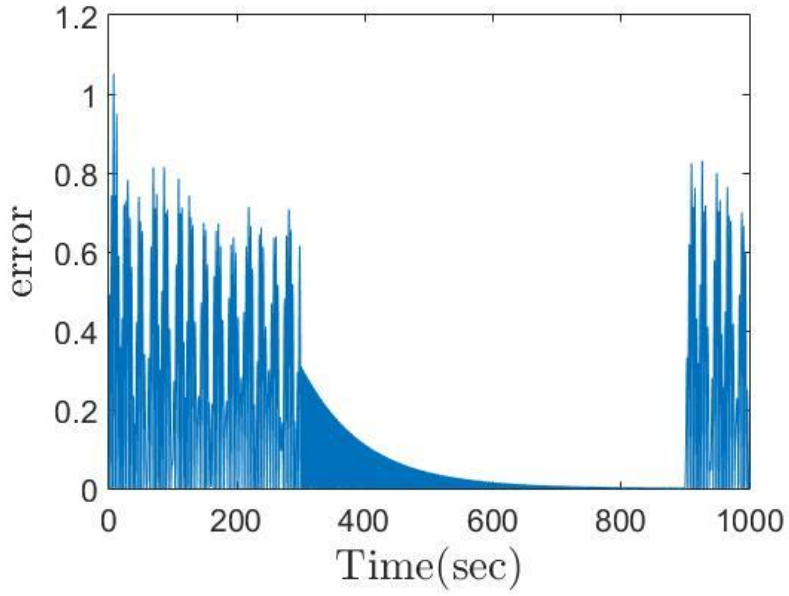

(b)

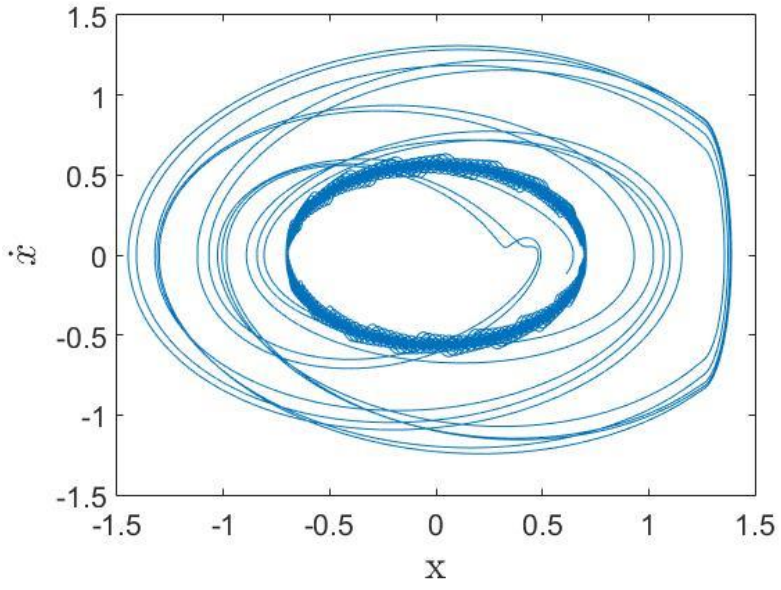

(c)

Figure 61 Continued.

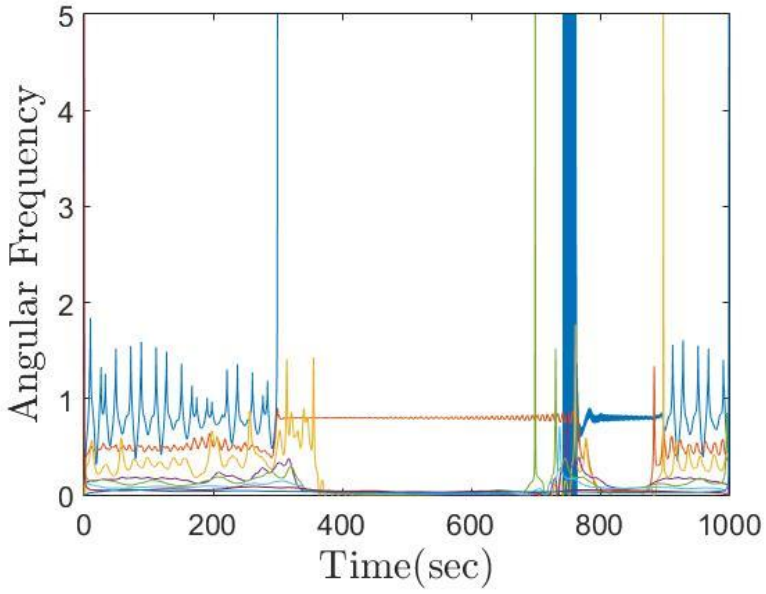

(d)

Figure 61 Continued.

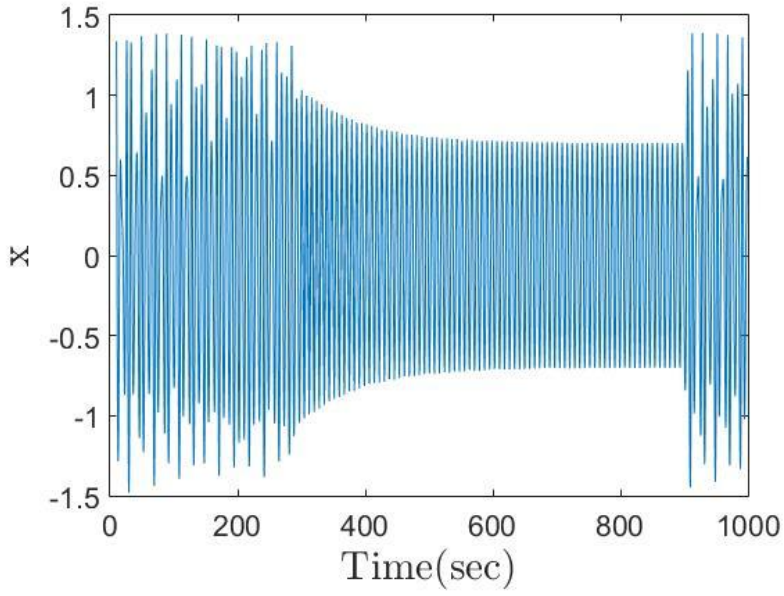

(a)

Figure 62 (a) Time response, (b) Error response, (c) Phase portrait, and (d) Instantaneous frequency of the time-delayed vibro-impact oscillator with Fuzzy controller initiated at t = 300 sec, closed at t = 900 sec, and time-delay t_d = 0.1 sec.

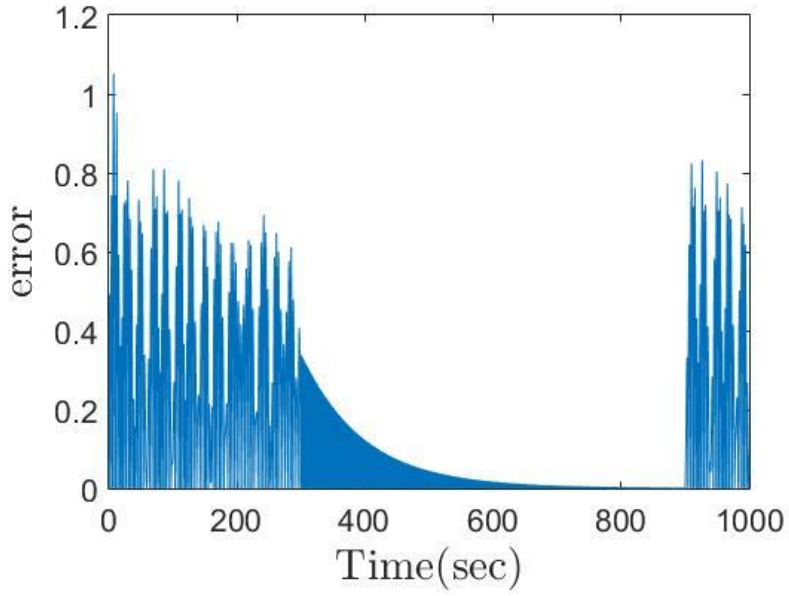

(b)

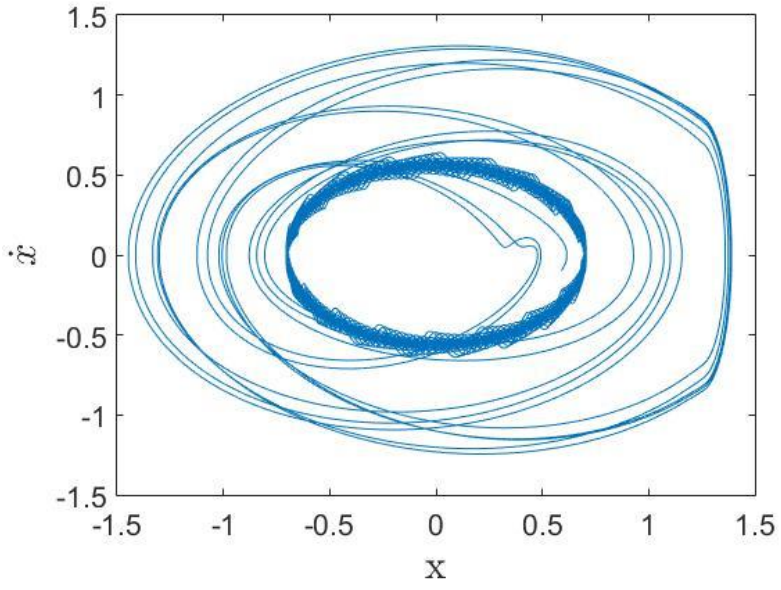

(c)

Figure 62 Continued.

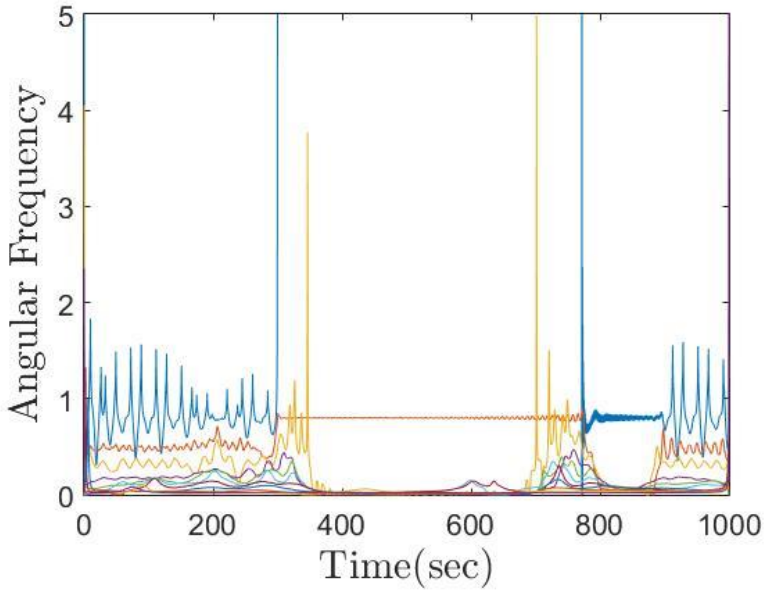

(d)

Figure 62 Continued.

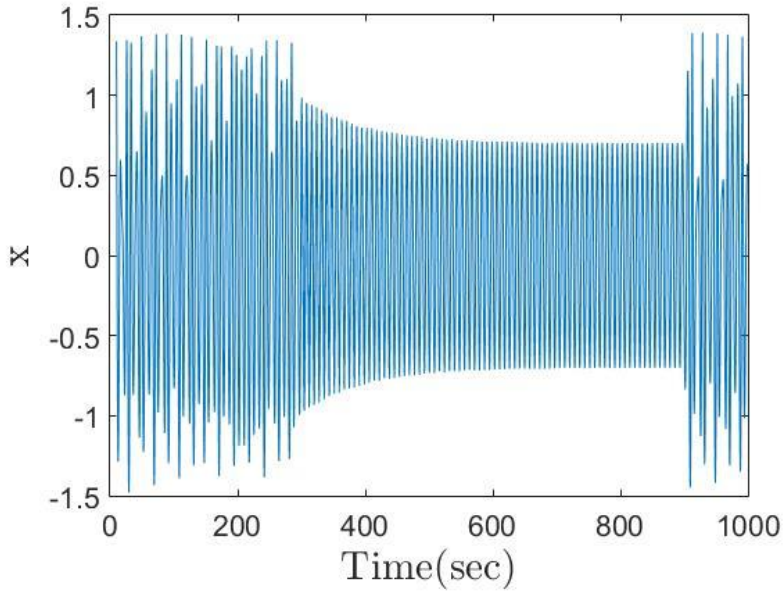

(a)

Figure 63 (a) Time response, (b) Error response, (c) Phase portrait, and (d) Instantaneous frequency of the time-delayed vibro-impact oscillator with Fuzzy controller initiated at t = 300 sec, closed at t = 900 sec, and time-delay t_d = 0.15 sec.

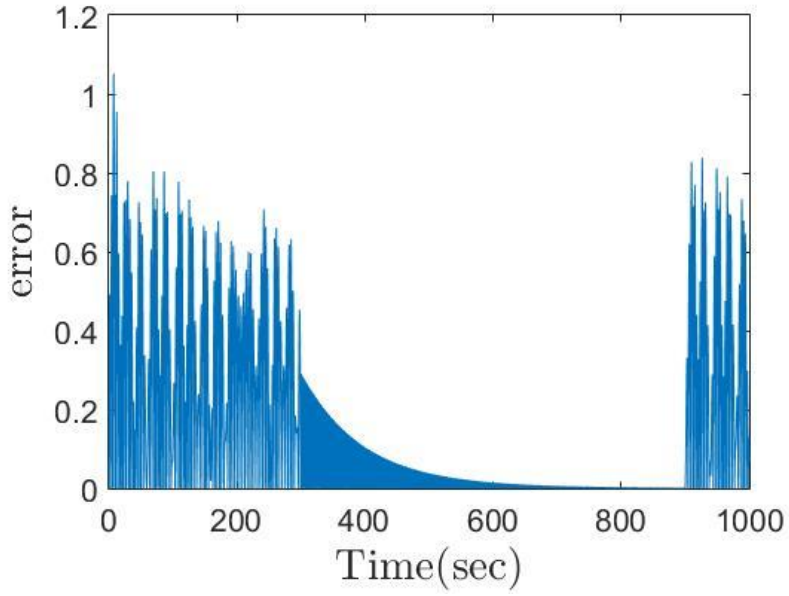

(b)

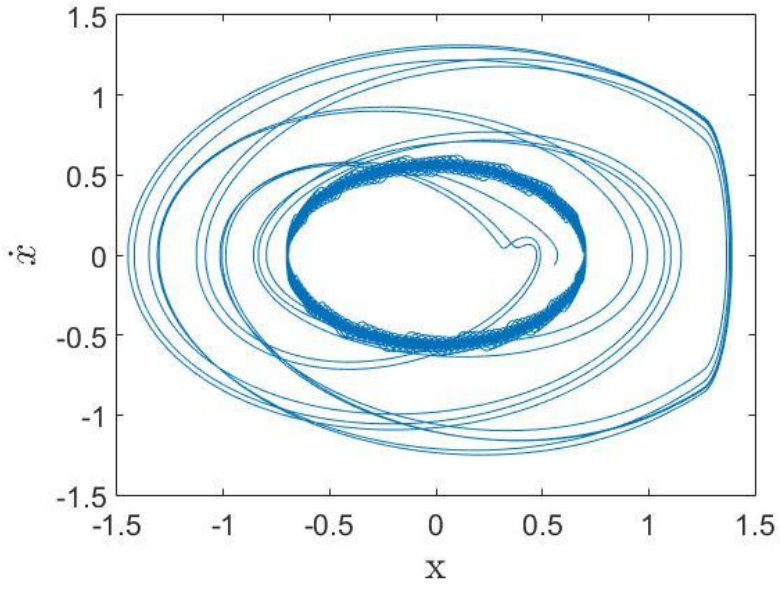

(c)

Figure 63 Continued.

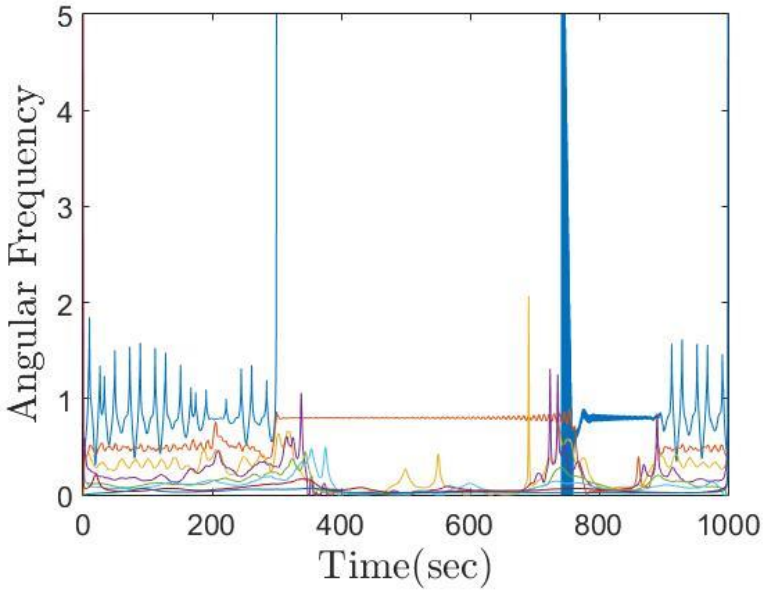

(d)

Figure 63 Continued.

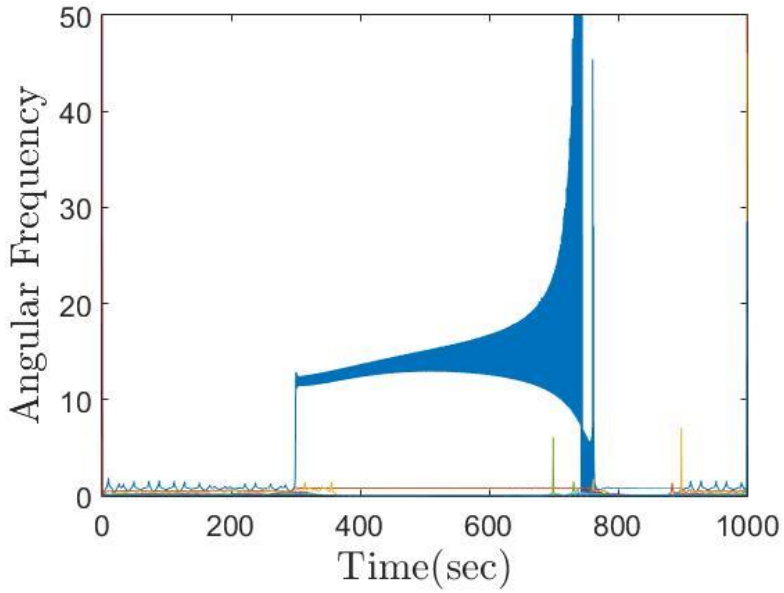

Figure 64 Wider frequency spectrum with Fuzzy controller initiated at t = 300 sec, closed at t = 900 sec, and time-delay t_d = 0.15 sec.

The time-delayed vibro-impact oscillator is engaged with the PID and fuzzy logic controllers for the same 3 time-delay values considered in Figure 47-Figure 49. System parameters used in Figure 51-Figure 53 are also adopted to ensure a common basis for evaluation. Figure 58(a) is the PID-controlled time response with $t_d = 0.05$ sec. The controller is initiated at $t = 300$. The phase portrait In Figure 58(c) indicates that the oscillator is in a broad bandwidth state of aperiodic motion and the instantaneous frequency response in Figure 58(d) shows that multiple frequency responses are generated as a result. The PID design is applied to the time-delayed feedback system with the delayed parameter equals to 0.1 sec and the corresponding responses are presented in Figure 59. Chatter remains prominent in the time response after the controller is brought online at $t = 300$. The phase portrait in Figure 59(c) shows a limit-cycle. The corresponding instantaneous frequency in Figure 59(d) confirms an initially quasi-periodic motion of the broadband frequency kind slowly converging to a weak aperiodic response. The responses of the system with $t_d = 0.15$ sec are presented in Figure 60. They are similar to the responses in Figure 58 and Figure 59 where bandwidth-limited temporal-modal oscillations of multiple frequency components are observed. Figure 61-Figure 63 are the fuzzy logic-controlled responses of the system with t_d = 0.05 sec, 0.1 sec and 0.15 sec, respectively. Although the error chattering in each time responses is comparable to those of the PID controller, the instantaneous frequency plot in Figure 64 shows that the high frequency responses as the results of the control action are non-stationary (time-varying) and broad in bandwidth, thus necessarily indicating that the dynamic state of motion is fast deteriorating under the jurisdiction of

the controller. The corresponding phase portraits in Figure 61-Figure 63 also attest that the system converges to broad bandwidth aperiodic motion after the controller is initiated.

Summary

The wavelet-based nonlinear time-frequency controller with parallel on-line modeling and local adaptability developed in Chapter II was implemented to control the time-delayed vibro-impact oscillator. The controller demonstrated the ability to reduce the vibration amplitude of the system, which is important for preventing the system from impacting the boundary. The controlled motions of the system were all unconditionally stationary, periodically stable, and of the time and frequency characteristics dictated by the prescribed target response, thus demonstrating the feasibility of the simultaneous time-frequency controller design in stabilizing the discontinuous vibro-impact system. The two common controller designs, namely PID and fuzzy logic controllers, all induced a multi-frequency noise after the control action was applied. This was attributed to the fact that the feedback features inherent of the controller design inadvertently perturbed the oscillator with the nonlinear and time-delay terms. The instantaneous frequency responses of the time-frequency control indicated that the controller successfully mitigated the noise and stabilized the time-delayed vibro-impact system. PID and fuzzy logic controllers on the other hand were seen to reduce the difference between the output and desired signals slightly better than the time-frequency control. However, the error responses of the time-frequency controller were within tolerance and not affecting the

proper functioning of the dynamic system. The broadband temporal-modal oscillations seen in Figure 58-Figure 60 and high frequency responses in Figure 61-Figure 63 negatively impact the system with significantly higher power consumption, render poor accuracy, and destabilize the system to eventual physical deterioration. The time-frequency controller in contrast is feasible for the proper mitigation of the time-delayed vibro-impact oscillator without the issues that are intimately associated with the PID and fuzzy logic control methodologies.

CHAPTER VII

CONCLUSIONS AND RECOMMENDATIONS

Conclusion

In Chapter II, a novel nonlinear control theory was presented. By synergizing system identification LMS and Filtered-x LMS algorithm, filters of local adaptability were developed to adjust the input force for mitigating nonlinear responses that are non-smooth and non-stationary. Wavelet filterbanks were employed to characterize the system in both the time and frequency domains, thus rendering simultaneous time-frequency control. With the optimization step size self-adaptive to system identification and control force input, convergence of the control methodology is unconditional. Derivation was also given to identify the optimal proper initial filter weights that ensured fast convergence rate and short response time. These novel features render the wavelet based nonlinear time-frequency control theory adaptive, intelligent, and universally applicable.

In Chapter III, the wavelet-based time-frequency controller with parallel on-line modeling developed in Chapter II was subsequently implemented to control and stabilize the dynamic response of a vibro-impact oscillator. The controller demonstrated the ability to reduce the vibration amplitude of the system, which is important for preventing the system from impacting the boundary. The controlled motions of the vibro-impact system were all unconditionally stationary, quasi-periodically stable, and of the time and frequency characteristics dictated by the prescribed target response, thus demonstrating

the feasibility of the simultaneous time-frequency controller design in stabilizing the discontinuous vibro-impact system.

In Chapter IV, a non-autonomous time-delayed feedback oscillator with high-order external forcing and various time-delay parameters was studied. Characterized by nonlinear, nonstationary time response and broad bandwidth spectral response, the oscillator was sensitive to the time-delay parameter. By implementing the wavelet-based time-frequency controller to adjust the input force to the system, the performance, quality, and capacity of the system response was significantly improved. With the controlled motions being unconditionally stationary and quasi-periodically stable, the controller demonstrated the ability to mitigate the severe complex state of unstable motions dictated by the higher order feedback system.

In Chapter V and Chapter VI, a novel time-delayed vibro-impact oscillator was investigated. By using phase portraits and bifurcation plots, it was seen that the oscillator is sensitively prone to dynamic instability characterized by nonlinear, nonstationary time response and broad bandwidth spectral response. Such a state of instability in manufacturing would result in premature tool breakage, increased wear rate, and poor workpiece quality. Improvements of the discontinuous system in performance and stability were consequential with the implementation of the wavelet-based time-frequency controller with parallel on-line modeling. The performance of the time-frequency control algorithm was evaluated against two popular control methodologies with the time-delay parameter as the controlled variable. The time-frequency controller demonstrated the most notable property in the frequency domain. As was evident in the

instantaneous frequency domain, the motions of the oscillator controlled by the time-frequency controller were unconditionally stable, stationary and periodic, while those controlled by PID and Fuzzy logic controllers were chattering and aperiodic.

Contribution and Impact

In this doctoral dissertation, a vibro-impact oscillator and a non-autonomous time-delayed feedback oscillator are investigated along with a newly formulated time-delayed vibro-impact oscillator. Characterized by nonlinear, nonstationary time response and broad bandwidth spectral response, and sensitively prone to dynamic instability, these three nonlinear systems are stochastic, aperiodic, and hard to control using classical approach. High frequency nonlinear responses are detrimental to system reliability and operation efficiency in terms of cost and power consumption. The wavelet-based time-frequency control theory developed in this work features parallel online modeling and local adaptability that generates optimal initial filter values and warrants unconditional, fast convergence. The local adaptability is novel, intelligent, self-adjusting, and universally applicable to addressing bifurcated and chaotic responses. Incorporating the control theory into designing dynamic systems governed by discontinuous, time-delayed nonlinear oscillators in particular would realize unconditional stability and high performance quality and operation efficiency.

Recommendation for Future Work

Although the wavelet-based time-frequency control theory is enhanced with the local adaptivity featuring self-adaptive optimization step size and optimal initial filter weights, other controller parameters such as the size of the wavelet filterbank and the order of the (Daubechies) decomposition and synthesis wavelet functions need be investigated to further evolve the control methodology. It is recommended that the numerical experiments considered in this dissertation be used to inspire the development of physical experiments, allowing comprehensive insight into the complex dynamics of the vibro-impact oscillator with time-delay effect to be generated.

REFERENCES

[1] Peterka, F., 1974, “Laws of impact motion of mechanical systems with one degree of freedom. I Theoretical analysis of n-multiple /1/n/-impact motions,” *Acta Technica CSAV,* Vol. 19(4), pp. 462−473.

[2] Thompson, J.M.T., and Ghaffari, R., 1983, “Chaotic dynamics of an impact oscillator,” *Physical Review A,* Vol. 27(3), pp. 1741−1743.

[3] Holmes, P. J., 1982, “The dynamics of repeated impacts with a sinusoidally vibrating table,” *Journal of Sound and Vibration,* Vol. 84(2), pp. 173–189.

[4] Whiston, G.S., 1987, “The vibro-impact response of a harmonically excited and preloaded one-dimensional linear oscillator,” *Journal of Sound and Vibration,* Vol. 115(2), pp. 303−319.

[5] Whiston, G.S., 1987, “Global dynamics of a vibro-impacting linear oscillator,” *Journal of Sound and Vibration,* Vol. 118(3), pp. 395−429.

[6] Whiston, G.S., 1992, “Singularities in vibro-impact dynamics,” *Journal of Sound and Vibration,* Vol. 152(3), pp. 427-460.

[7] Budd, C., and Dux, F., 1994, “Chattering and related behaviour in impact oscillators,” *Philosophical Transactions of the Royal Society of London. Series A: Physical and Engineering Sciences,* Vol. 347(1683), pp. 365-389.

[8] Budd, C., and Dux, F., 1994, “Intermittency in impact oscillators close to resonance,” *Nonlinearity,* Vol. 7(4), p. 1191.

[9] Gegg, B.C., Luo, A.C., and Suh, S.C., 2008, “Grazing bifurcations of a harmonically excited oscillator moving on a time-varying translation belt,” *Nonlinear Analysis: Real World Applications,* Vol. 9(5), pp. 2156-2174.

[10] Nordmark, A.B., 1991, “Non-periodic motion caused by grazing incidence in an impact oscillator,” *Journal of Sound and Vibration,* Vol. 145(2), pp. 279-297.

[11] Nordmark, A.B., 1992, "Effects due to low velocity impact in mechanical oscillators," *International Journal of Bifurcation and Chaos*, Vol. 02(03), pp. 597-605.

[12] Nordmark, A.B., 1997, "Universal limit mapping in grazing bifurcations," P*hysical Review E*, Vol. 55(1), pp. 266-270.

[13] Fredriksson, M.H., and Nordmark, A.B., 1997, "Bifurcations caused by grazing incidence in many degrees of freedom impact oscillators," *Proceedings of the Royal Society of London. Series A: Mathematical, Physical and Engineering Sciences*, Vol. 453(1961), pp. 1261-1276.

[14] Nordmark, A.B., 2001, "Existence of periodic orbits in grazing bifurcations of impacting mechanical oscillators," *Nonlinearity*, Vol. 14(6), pp. 1517-1542.

[15] Dankowicz, H., Piiroinen, P., and Nordmark, A.B., 2002, "Low-velocity impacts of quasiperiodic oscillations," *Chaos, Solitons & Fractals*, Vol. 14(2), pp. 241-255.

[16] Chillingworth, D.R.J., 2010, "Discontinuity geometry for an impact oscillator Dynamical Systems," *Dynamical Systems*, Vol. 17(4), pp. 389-420.

[17] Chillingworth, D.R.J., 2010, "Dynamics of an impact oscillator near a degenerate graze," *Nonlinearity*, Vol. 23(11), pp. 2723-2748.

[18] Chin, W., Ott, E., Nusse, H. E., and Grebogi, C., 1995, "Universal behavior of impact oscillators near grazing incidence," *Physics Letters A*, Vol. 201(2-3), pp. 197-204.

[19] Gorbikov, S.P., and Men'shenina, A.V., 2007, "Statistical description of the limiting set for chaotic motion of the vibro-impact system," *Automation and Remote Control*, Vol. 68(10), pp. 794-1800.

[20] de Weger, J., van de Water, W. and Molenaar, J., 2000, "Grazing impact oscillations," *Physical Review E*, Vol. 62(2), p. 2030.

[21] Lamba, H., 1995, "Chaotic, regular and unbounded behaviour in the elastic impact oscillator," *Physica D: Nonlinear Phenomena*, Vol. 82(1-2), pp. 117-135.

[22] Ing, J., Pavlovskaia, E., Wiercigroch, M., and Banerjee, S., 2007, "Experimental study of impact oscillator with one-sided elastic constraint," *Philosophical Transactions of the Royal Society A: Mathematical, Physical and Engineering Sciences*, Vol. 366(1866), pp. 679-705.

[23] Banerjee, S., Ing, J., Pavlovskaia, E., Wiercigroch, M., and Reddy, R.K., 2009, "Invisible grazings and dangerous bifurcations in impacting systems: the problem of narrow-band chaos," *Physical Review E*, Vol. 79(3), p. 037201.

[24] Ing, J., Pavlovskaia, E., Wiercigroch, M., and Banerjee, S., 2010, "Bifurcation analysis of an impact oscillator with a one-sided elastic constraint near grazing," *Physica D: Nonlinear Phenomena*, Vol. 239(6), pp. 312-321.

[25] Ivanov, A.P., 1993, "Stabilization of an impact oscillator near grazing incidence owing to resonance," *Journal of Sound Vibration*, Vol. 162, pp. 562-565.

[26] Lee, J.Y., and Yan, J.J., 2006, "Control of impact oscillator," *Chaos, Solitons & Fractals*, Vol. 28(1), pp. 136-142.

[27] Lee, J.Y., and Yan, J.J., 2007, "Position control of double-side impact oscillator," *Mechanical Systems and Signal Processing*, Vol. 21(2), pp. 1076-1083.

[28] Bishop, S.R., Wagg, D.J., and Xu, D., 1998, "Use of control to maintain period-1 motions during wind-up or wind-down operations of an impacting driven beam," *Chaos, Solitons & Fractals*, Vol. 9(1-2), pp. 261-269.

[29] Bichri, A., Belhaq, M., and Perret-Liaudet, J, 2011, "Control of vibroimpact dynamics of a single-sided Hertzian contact forced oscillator," *Nonlinear Dynamics*, Vol. 63(1-2), pp. 51-60.

[30] Awrejcewicz, J., Tomczak, K., and Lamarque, C.H., 1999, "Controlling systems with impacts," *International Journal of Bifurcation and Chaos*, Vol. 9(03), pp. 547-553.

[31] Ott, E., Grebogi, C., and Yorke, J.A., 1990, "Controlling chaos," *Physical Review Letters*, Vol. 64(11), pp. 1196-1199.

[32] Gritli, H., Belghith, S., and Khraief, N., 2014, “Control of chaos in an impact mechanical oscillator,” *Proceedings-Copyright IPCO*, pp. 116-122.

[33] De Souza, S.L., Caldas, I.L., Viana, R.L., and Balthazar, J.M., 2008, “Control and chaos for vibro-impact and non-ideal oscillators,” *Journal of Theoretical and Applied Mechanics*, Vol. 46(3), pp. 641-664.

[34] de Souza, S.L., and Caldas, I.L., 2004, “Controlling chaotic orbits in mechanical systems with impacts,” *Chaos, Solitons & Fractals*, Vol. 19(1), pp. 171-178.

[35] de Souza, S.L., Caldas, I.L., and Viana, R.L., 2007, “Damping control law for a chaotic impact oscillator,” *Chaos, Solitons & Fractals*, Vol. 32(2), pp. 745-750.

[36] Suh, C.S., and Liu, M.K., 2013. *Control of cutting vibration and machining instability: a time-frequency approach for precision, micro and nano machining*. John Wiley & Sons, Inc.

[37] Simos, C., Simos, H., Mesaritakis, C., Kapsalis, A., and Syvridis, D., 2014, "Pulse and noise properties of a two section passively mode-locked quantum dot laser under long delay feedback," *Optics Communications*, Vol. 313(0), pp. 248-255.

[38] Guillo-Sansano, E., Roscoe, A.J., Jones, C.E., and Burt, G.M., 2014, “A new control method for the power interface in power hardware-in-the-loop simulation to compensate for the time delay,” In *2014 49th International Universities Power Engineering Conference (UPEC)*, IEEE, pp. 1-5.

[39] Fraser, A.M., and Swinney, H.L., 1986, “Independent coordinates for strange attractors from mutual information,” *Physical Review A*, Vol. 33(2), p. 1134.

[40] Ge, Z.M., and Lee, C.I., 2005, "Control, anticontrol and synchronization of chaos for an autonomous rotational machine system with time-delay," *Chaos, Solitons & Fractals*, Vol. 23(5), pp. 1855-1864.

[41] Pierre, T., Bonhomme, G., and Atipo, A., 1996, “Controlling the chaotic regime of nonlinear ionization waves using the time-delay autosynchronization method,” *Physical Review Letters*, Vol. 76(13), p. 2290.

[42] Hu, H., Dowell, E.H., and Virgin, L.N., 1998, “Resonances of a harmonically forced Duffing oscillator with time delay state feedback,” *Nonlinear Dynamics*, Vol. 15(4), pp. 311-327.

[43] Rosenstein, M.T., Collins, J.J., and De Luca, C.J., 1993, “A practical method for calculating largest Lyapunov exponents from small data sets,” *Physica D: Nonlinear Phenomena*, Vol. 65(1-2), pp. 117-134.

[44] Bryant, P., Brown, R., and Abarbanel, H.D., 1990, "Lyapunov exponents from observed time series," *Physical Review Letters*, Vol. 65(13), pp. 1523-1526.

[45] Liebert, W., and Schuster, H.G., 1989, "Proper choice of the time delay for the analysis of chaotic time series," *Physics Letters A*, Vol. 142(2–3), pp. 107-111.

[46] Kugiumtzis, D., 1996, "State space reconstruction parameters in the analysis of chaotic time series — the role of the time window length," *Physica D: Nonlinear Phenomena*, Vol. 95(1), pp. 13-28.

[47] Suh, C.S., and Yang, B., 2004, "On the nonlinear features of time-delayed feedback oscillators," *Communications in Nonlinear Science and Numerical Simulation*, Vol. 9(5), pp. 515-529.

[48] Farmer, J.D., Ott, E., and Yorke, J.A., 1983, “The dimension of chaotic attractors,” *Physica D: Nonlinear Phenomena*, Vol. 7(1-3), pp. 153-180.

[49] Reddy, D.R., Sen, A., and Johnston, G.L., 2000, “Dynamics of a limit cycle oscillator under time delayed linear and nonlinear feedbacks,” *Physica D: Nonlinear Phenomena*, Vol. 144(3-4), pp. 335-357.

[50] Yu, P., Yuan, Y., and Xu, J., 2002, "Study of double Hopf bifurcation and chaos for an oscillator with time delayed feedback," *Communications in Nonlinear Science and Numerical Simulation*, Vol. 7(1–2), pp. 69-91.

[51] Mirafzal, S.H., Khorasani, A.M., and Ghasemi, A.H., 2016, “Optimizing time delay feedback for active vibration control of a cantilever beam using a genetic algorithm,” *Journal of Vibration and Control*, Vol. 22(19), pp. 4047-4061.

[52] Yuan, Y., Yu, P., Librescu, L., and Marzocca, P., 2004, "Aeroelasticity of time-delayed feedback control of two-dimensional supersonic lifting surfaces," *Journal of Guidance, Control, and Dynamics*, Vol. 27(5), pp. 795-803.

[53] Iñarrea, M., Lanchares, V., Pascual, A. I., and Salas, J. P., 2014, "Attitude stabilization of electrodynamic tethers in elliptic orbits by time-delay feedback control," *Acta Astronautica*, Vol. 96(0), pp. 280-295.

[54] Cao, J., Yuan, R., Jiang, H., and Song, J., 2014, "Hopf bifurcation and multiple periodic solutions in a damped harmonic oscillator with delayed feedback," *Journal of Computational and Applied Mathematics*, Vol. 263(0), pp. 14-24.

[55] Ma, S., Lu, Q., and Feng, Z., 2008, "Double Hopf bifurcation for van der Pol-Duffing oscillator with parametric delay feedback control," *Journal of Mathematical Analysis and Applications*, Vol. 338(2), pp. 993-1007.

[56] Zeng, H.B., He, Y., Wu, M., and She, J., 2015, "Free-matrix-based integral inequality for stability analysis of systems with time-varying delay," *IEEE Transactions on Automatic Control*, Vol. 60(10), pp. 2768-2772.

[57] Gurevich, S.V., 2014, "Time-delayed feedback control of breathing localized structures in a three-component reaction–diffusion system," *Philosophical Transactions of the Royal Society A: Mathematical, Physical and Engineering Sciences*, Vol. 372(2027), p. 20140014.

[58] Xu, S., Lam, J., Zhang, B., and Zou, Y. 2015, "New insight into delay-dependent stability of time-delay systems." *International Journal of Robust and Nonlinear Control*, Vol. 25(7), pp. 961-970.

[59] Yu, Y., Tang, H., Han, X., and Bi, Q., 2014, "Bursting mechanism in a time-delayed oscillator with slowly varying external forcing," *Communications in Nonlinear Science and Numerical Simulation*, Vol. 19(4), pp. 1175-1184.

[60] Xu, Y., Lu, R., Shi, P., Tao, J., and Xie, S., 2017, "Robust estimation for neural networks with randomly occurring distributed delays and Markovian jump coupling," *IEEE Transactions on Neural Networks and Learning Systems*, Vol. 29(4), pp. 845-855.

[61] Gao, X., and Chen, Q., 2014, "Nonlinear analysis, design and vibration isolation for a bilinear system with time-delayed cubic velocity feedback," *Journal of Sound and Vibration*, Vol. 333(6), pp. 1562-1576.

[62] Kim, J.H., and Park, H.B., 1999, " H_∞ state feedback control for generalized continuous/discrete time-delay system," *Automatica*, Vol. 35(8), pp. 1443-1451.

[63] Pyragas, K., 1998, "Synchronization of coupled time-delay systems: Analytical estimations," *Physical Review E*, Vol. 58(3), p. 3067.

[64] Cao, Y.Y., and Frank, P.M., 2000, "Analysis and synthesis of nonlinear time-delay systems via fuzzy control approach," *IEEE Transactions on Fuzzy Systems*, Vol. 8(2), pp. 200-211.

[65] Wang, H., Liu, X., Liu, K., and Karimi, H.R., 2014, "Approximation-based adaptive fuzzy tracking control for a class of nonstrict-feedback stochastic nonlinear time-delay systems," *IEEE Transactions on Fuzzy Systems*, Vol. 23(5), pp. 1746-1760.

[66] Du, B., and Ma, D., 2013, " H_∞ -Based Pinning Synchronization of General Complex Dynamical Networks with Coupling Delays," *Journal of Applied Mathematics*, Vol. 2013, Article ID 275205, http://dx.doi.org/10.1155/2013/275205.

[67] Qiu, J., Wei, Y., and Karimi, H.R., 2015, "New approach to delay-dependent H_∞ control for continuous-time Markovian jump systems with time-varying delay and deficient transition descriptions." *Journal of the Franklin Institute*, Vol. 352(1), pp. 189-215.

[68] Wu, L., Su, X., and Shi, P., 2012, "Sliding mode control with bounded gain performance of Markovian jump singular time-delay systems," *Automatica*, Vol. 48(8), pp. 1929-1933.

[69] Zhou, Q., Shi, P., Xu, S., and Li, H., 2012, "Adaptive output feedback control for nonlinear time-delay systems by fuzzy approximation approach," *IEEE Transactions on Fuzzy Systems*, Vol. 21(2), pp. 301-313.

[70] Goyal, V., Deolia, V.K., and Sharma, T.N., 2015, “Robust sliding mode control for nonlinear discrete-time delayed systems based on neural network,” *Intelligent Control and Automation*, Vol. 6(01), p. 75.

[71] Yang, Y., Yue, D., and Xue, Y., 2015, "Decentralized adaptive neural output feedback control of a class of large-scale time-delay systems with input saturation," *Journal of the Franklin Institute*, Vol. 352(5), pp. 2129-2151.

[72] Tong, S., Qian, D., Ren, J., Li, Y., and Li, H., 2014, “Networked Predictive Fuzzy Control systems with random time delay in the forward channel,” In *Proceeding of the 11th World Congress on Intelligent Control and Automation*, IEEE, pp. 2042-2046.

[73] An, F., Chen, W.D., and Shao, M.Q., 2015, “Study on discrete acceleration feedback control with time delay,” *Journal of Vibration and Control*, Vol. 21(7), pp. 1267-1285.

[74] Kuo, S.M., and Morgan, D., 1995. *Active noise control systems: algorithms and DSP implementations*. John Wiley & Sons, Inc.

[75] Yang, S.M., Sheu, G.J., and Liu, K.C., 2005, “Vibration control of composite smart structures by feedforward adaptive filter in digital signal processor,” *Journal of Intelligent Material Systems and Structures*, Vol. 16(9), pp. 773-779.

[76] Guan, Y.H., Lim, T.C., and Shepard, W.S., 2005, “Experimental study on active vibration control of a gearbox system,” *Journal of Sound and Vibration*, Vol. 282(3-5), pp. 713-733.

[77] Peng, F.J., Gu, M., and Niemann, H.J., 2003, “Sinusoidal reference strategy for adaptive feedforward vibration control: numerical simulation and experimental study,” *Journal of Sound and Vibration*, Vol. 265(5), pp. 1047-1061.

[78] Håkansson, L., Claesson, I., and Sturesson, P.O., 1998, “Adaptive feedback control of machine-tool vibration based on the filtered-x LMS-algorithm,” *Journal of Low Frequency Noise, Vibration and Active Control*, Vol. 17(4), pp. 199-213.

[79] Yazdanpanah, A., Khaki-Sedigh, A., and Yazdanpanah, A., 2005, "Adaptive control of chaos in nonlinear chaotic discrete-time systems," In *Proceedings. 2005 International Conference Physics and Control*, 2005, IEEE. pp. 913-915.

[80] Kim, H., and Adeli, H., 2004, "Hybrid feedback-least mean square algorithm for structural control," *Journal of Structural Engineering*, Vol. 130(1), pp. 120-127.

[81] Liu, M.K., and Suh, C.S., 2012, "Simultaneous time–frequency control of bifurcation and chaos," *Communications in Nonlinear Science and Numerical Simulation*, Vol. 17(6), pp. 2539-2550.

[82] Liu, M.K., Halfmann, E.B., and Suh, C.S., 2014, "Multi-dimensional time-frequency control of micro-milling instability," *Journal of Vibration and Control*, Vol. 20(5), pp. 643-660.

[83] Liu, M.K., and Suh, C.S., 2012, "On controlling milling instability and chatter at high speed," *Journal of Applied Nonlinear Dynamics,* Vol. 1(1), pp. 59–72.

[84] Haykin, S.S., 2002. *Adaptive Filter Theory, 4th ed*., Prentice-Hall," Upper Saddle River, New Jersey, 2002.

[85] Takenouchi, Y., Suzuki, H. and Omoto, A., 2006, "Behavior of the practically implemented filtered reference LMS algorithm in an active noise control system," *Acoustical Science and Technology*, Vol. 27(1), pp. 20-27.

[86] Long, G., Ling, F. and Proakis, J.G., 1989, "The LMS algorithm with delayed coefficient adaptation," I*EEE Transactions on Acoustics, Speech, and Signal Processing*, Vol. 37(9), pp. 1397-1405.

[87] Bjarnason, E., 1993, "Analysis of the filtered-X LMS algorithm," In *1993 IEEE International Conference on Acoustics, Speech, and Signal Processing*, Vol. 3, pp. 511-514.

[88] Vicente, L., 2006, "Novel FxLMS convergence condition with deterministic reference," *IEEE Transactions on Signal processing*, Vol. 54(10), pp. 3768-3774.

[89] Xiao, Y., Ikuta, A., Ma, L. and Khorasani, K., 2008, “Stochastic analysis of the FXLMS-based narrowband active noise control system,” *IEEE Transactions on Audio, Speech, and Language Processing*, Vol. 16(5), pp. 1000-1014.

[90] Gardner, W.A., 1984, “Learning characteristics of stochastic-gradient-descent algorithms: A general study, analysis, and critique,” *Signal Processing*, Vol. 6(2), pp. 113-133.

[91] Ardekani, I.T. and Abdulla, W.H., 2010, “Theoretical convergence analysis of FxLMS algorithm,” *Signal Processing*, Vol. 90(12), pp. 3046-3055.

[92] Bismor, D., 2012, “LMS algorithm step size adjustment for fast convergence,” *Archives of Acoustics*, Vol. 37(1), pp. 31-40.

[93] Kuo, C.W. and Suh, C.S., 2016, “Mitigating grazing bifurcation and vibro-impact instability in time-frequency domain,” *Journal Applied Nonlinear Dynamics*, Vol. 5, pp. 169-184.

[94] Kuo, C.W. and Suh, C.S., 2017, “A case of mitigating non-autonomous time-delayed system with cubic order feedback,” *Journal of the Franklin Institute*, Vol. 354(15), pp. 6651-6671.

[95] Kryzhevich, S.G., 2008, “Grazing Bifurcation and chaotic oscillations of single degree of freedom dynamical systems,” *Journal of Applied Mathematics and Mechanics*, Vol. 72(4), pp. 383-390.

[96] Yang, B. and Suh, C.S., 2003, "Interpretation of crack induced nonlinear response using instantaneous frequency," *Mechanical Systems and Signal Processing*, Vol. 18(3), pp. 491-513.

APPENDIX A

By substituting Eq. (2.55) into the performance function, $J(\mathbf{W})$, one has

$$\begin{aligned} J(\mathbf{W}) &= E\left[e(n)e^T(n)\right] \\ &= E\left\{\left[e_{opt}(n)-\sum_{q=0}^{Q-1} w_{1T,q}\mathbf{c}^T(n-q)\mathbf{z}(n-q)\right]\left[e_{opt}(n)-\sum_{p=0}^{Q-1} w_{1T,p}\mathbf{z}^T(n-p)\mathbf{c}(n-p)\right]\right\} \\ &= E\left\{e_{opt}^2(n)\right\}+\sum_{q=0}^{Q-1}\sum_{p=0}^{Q-1} w_{1T,q}w_{1T,p}\left[\mathbf{c}^T(n-q)\mathbf{z}(n-q)\mathbf{z}^T(n-p)\mathbf{c}(n-p)\right] \\ &\quad -2\sum_{q=0}^{Q-1} w_{1T,q}E\left[\mathbf{c}^T(n-q)\mathbf{z}(n-q)e_{opt}(n)\right] \end{aligned} \tag{A.1}$$

Since $e_{opt}(n)$ is assumed to be a zero mean signal and statistically independent of weights and the input signal, the 3rd term in Eq. (A.1) is therefore zero. The MSE can be expressed using the rotated variables as

$$J(n) = J_{\min} + J_{ex}(n) \tag{A.2}$$

where the minimum MSE $J_{\min}$ is

$$J_{\min} \triangleq E\left\{e_{opt}^2(n)\right\} \tag{A.3}$$

and the excess MSE (EMSE) $J_{ex}(n)$ is

$$J_{ex}(n) = \sum_{q=0}^{Q-1}\sum_{p=0}^{Q-1} w_{1T,q}w_{1T,p}\left[\mathbf{c}^T(n-q)\mathbf{z}(n-q)\mathbf{z}^T(n-p)\mathbf{c}(n-p)\right] \tag{A.4}$$

Based on independent assumption that correlation matrix between different vector of a stationary input signal can be approximated as

$$E\left\{\mathbf{X}_T(n-p)\mathbf{X}_T^T(n-q)\right\} = \delta_{p,q}\mathbf{R} \tag{A.5}$$

where δ is the Kronecker delta function. Then, Eq. (A.5) can be further derived as

$$E\left\{\mathbf{X}_T\left(n-p\right)\mathbf{X}_T^T\left(n-q\right)\right\}=\delta_{p,q}\mathbf{F}\mathbf{\Lambda}\mathbf{F}^T \tag{A.6}$$

By multiplying $\mathbf{F}$ and $\mathbf{F}^T$ to both sides of Eq. (A.6), one has

$$\begin{aligned}\delta_{p,q}\mathbf{\Lambda}&=\delta_{p,q}\mathbf{F}^T\mathbf{F}\mathbf{\Lambda}\mathbf{F}^T\mathbf{F}\\&=\mathbf{F}^T E\left\{\mathbf{X}_T\left(n-p\right)\mathbf{X}_T^T\left(n-q\right)\right\}\mathbf{F}\\&=E\left\{\mathbf{F}^T\mathbf{X}_T\left(n-p\right)\mathbf{X}_T^T\left(n-q\right)\mathbf{F}\right\}\\&=E\left\{\mathbf{z}\left(n-p\right)\mathbf{z}^T\left(n-q\right)\right\}\end{aligned} \tag{A.7}$$

Submitting Eq. (A.7) intro Eq. (A.4) to obtain $J_{ex}\left(n\right)$ as follows which is Eq. (2.58)

$$\begin{aligned}J_{ex}\left(n\right)&=\sum_{q=0}^{Q-1}\sum_{p=0}^{Q-1}w_{1T,q}w_{1T,p}E\left[\mathbf{c}^T\left(n-q\right)\delta_{p,q}\mathbf{\Lambda}\mathbf{c}\left(n-p\right)\right]\\&=\sum_{p=0}^{Q-1}w_{1T,q}^2E\left[\mathbf{c}^T\left(n-q\right)\mathbf{\Lambda}\mathbf{c}\left(n-p\right)\right]\end{aligned} \tag{A.8}$$